공학박사 학위논문

Synthesis and Characterization of Environmentally Benign Alloyed Core/Shell Heterostructured Nanocrystals

친환경 합금 코어쉘 이종접합구조 양자점의 합성과 특성분석

2023년 8월

서울대학교 대학원
화학생물공학부

이학준

Synthesis and Characterization of Environmentally Benign Alloyed Core/Shell Heterostructured Nanocrystals

지도교수 차국헌

이 논문을 공학박사 학위논문으로 제출함

2023년 8월

서울대학교 대학원
화학생물공학부
이학준

이학준의 박사학위 논문을 인준함
2023년 8월

Chair	이 원 보	(Seal)
Vice Chair	차 국 헌	(Seal)
Examiner	배 완 기	(Seal)
Examiner	임 재 훈	(Seal)
Examiner	강 문 성	(Seal)

Abstract

Synthesis and Characterization of Environmentally Benign Alloyed Core/Shell Heterostructured Nanocrystals

Hak June Lee
School of Chemical & Biological Engineering
Seoul National University

Colloidal semiconductor nanocrystals (NCs) have garnered interests for their remarkable optical properties such as broad absorption but narrow emission linewidth, tunable band gap and near-unity photoluminescence quantum yield (PL QY). These properties have facilitated the successful practical use of NCs in the luminescent solar concentrator (LSC), light-emitting-diodes (LEDs) and lasers. However, the extensive use of CdSe-based NCs, which have been instrumental in these advancements, is hampered by stringent environmental regulations.

To address these regulatory concerns, both academia and industrial fields have developed environmentally benign NCs, notably InP-based NCs. Nevertheless, InP-based NCs suffer from significant drawbacks that hinder their use in the industrial

fields. such as low absorption coefficient at blue spectral regime, broad emission linewidth, and the challenge of realizing blue-emitting InP-based NCs.

Herein, we reported synthesis and characterization of spherical quantum well ZnSe/$ZnSe_{1-X}Te_X$/ZnSe NCs and core/shell $AgIn_XGa_{1-X}S_2$/$AgGaS_2$ NCs, which represent new class of environmentally benign NCs bearing near-unity PL QYs across full visible range (450 nm to 630 nm). Through structural, optical, photophysical analyses with computational calculations, we unveil synthetic processes and emission mechanism of these NCs. Our findings expand the Cd-free material envelope to the $ZnSe_{1-X}Te_X$ and $AgIn_XGa_{1-X}S_2$ NCs, thereby offering promising prospects for a wide range of light emitting applications.

In Chapter 1, fundamental properties of NCs and history of environmentally benign NCs are introduced briefly. We also highlight the necessity of developing alternatives of InP-based NCs and the present challenges faced in developing environmentally benign NCs.

In Chapter 2, we demonstrate a new class of *quasi*-type II nano-emitters formulated in ZnSe/$ZnSe_{1-X}Te_X$/ZnSe seed/spherical quantum well/shell heterostructures (SQW) whose emission wavelength ranges from blue to orange. In a given geometry, $ZnSe_{1-X}Te_X$ emissive layers grown between the ZnSe seed and shell layer are strained to fit into the surrounding media, and thus the lattice mismatch between $ZnSe_{1-X}Te_X$ and ZnSe is effectively alleviated. In addition, composition of $ZnSe_{1-X}Te_X$ emissive layer and the dimension of ZnSe shell layer are engineered to tailor the distribution and energy of electron and hole wavefunctions. Benefited from the capabilities to tune the charge carriers on demand and to form defect-free heterojunctions, $ZnSe/ZnSe_{1-X}Te_X/ZnSe/ZnS$ NCs show near-unity photoluminescence quantum yield (PL QY > 90 %) in a broad range of emission wavelength (peak PL from 450 nm to 600 nm). Finally, we exemplify dichromatic white NC-LEDs employing the mixed layer of blue- and yellow-emitting $ZnSe/ZnSe_{1-X}Te_X/ZnSe/ZnS$ SQW NCs.

In Chapter 3, we explore the excitonic states in $ZnSe_{1-X}Te_X$ NCs and their photophysical characteristics in relation to the morphological inhomogeneity of highly mismatched alloys. Ensemble and single-dot spectroscopic analysis on a series of $ZnSe_{1-X}Te_X$ NC samples with varying Te ratios coupled with computational calculations show that, due to the distinct electronegativity between Se *versus* Te, nearest-neighbor Te pairs in $ZnSe_{1-X}Te_X$ alloys create localized hole states spectrally distributed approximately 130 meV above $1S_h$ level of homogenous $ZnSe_{1-X}Te_X$ NCs. This forms spatially separated excitons (delocalized electron + localized hole in trap), accounting for both inhomogeneous and homogeneous linewidth broadening with delayed recombination dynamics. Our results identify photophysical characteristics of excitonic states in NCs made of highly mismatched alloys and provide future research directions with potential implication of photonic applications.

In Chapter 4, Multicarrier dynamics of $ZnSe_{1-X}Te_X$ NCs are undetermined yet due to their strange behavior that positive trion is prevailing, not negative trion. Thus, we demonstrate an opto-electrical method that enables us to precisely assess AR rates of X^+ and X^- in core/shell heterostructured NCs. Specifically, we devise electron-only-devices and hole-only-devices to inject extra charge carriers into NCs without unwanted side reactions or degradation of NCs, and probe AR characteristics of these charged NCs *via* time-resolved photoluminescence measurements. We find that AR rates of charged excitons, both X^+ and X^-, gained from the present method agree well with those attained from conventional approaches and the superposition principle, corroborating the validity of the present approach. This present method permits to comprehend multicarrier dynamics in NCs, prompting the use of NCs in light-emitting diodes and laser devices based on NCs.

In Chapter 5, we present the heteroepitaxy for AIGS-$AgGaS_2$ (AIGS-AGS) core-shell NCs bearing near-unity PL QYs in almost full visible range (460 nm to 620 nm) and enhanced photochemical stability. Key to the successful growth of AIGS-AGS NCs is the use of the $Ag-S-Ga(OA)_2$ complex, which complements the reactivities among cations for both homogeneous AIGS cores in various compositions and uniform AGS shell growth. The heteroepitaxy between AIGS and AGS results in the Type I heterojunction that effectively confines charge carriers within the emissive core without optically active interfacial defects. AIGS-AGS NCs show remarkably

higher extinction coefficient and narrower spectral linewidth compared to state-of-the-art heavy metal-free NCs, prompting their immediate use in practicable applications including displays and luminescent solar concentrators.

Keyword : colloidal nanocrystals · environmentally-benign nanocrystals · spherical quantum well · Auger recombination · synthetic mechanism

Student Number : 2018-22155

Table of Contents

List of Figures

Chapter 1. Introduction

1.1. Colloidal semiconductor nanocrystals

1.1.1 Fundamental properties of nanocrystals

Colloidal semiconductor NCs are solution processable nano-emitters that feature size-dependent emission tunability and narrow spectral linewidth with near-unity quantum yield upon optical or electrical excitation, promising their use in a wide-range of light-emitting applications (**Fig. 1.1a, b**).[1-6] Representative examples are the down-conversion[7,8] or electroluminescence[9-12] NC displays, in which NCs convert high energy excitation photons or electrically injected charge carriers into narrow band emission of photon energies corresponding to NCs' band gap. After their success in displays, NCs have extended their application territory (**Fig. 1.1c**).[13-15]

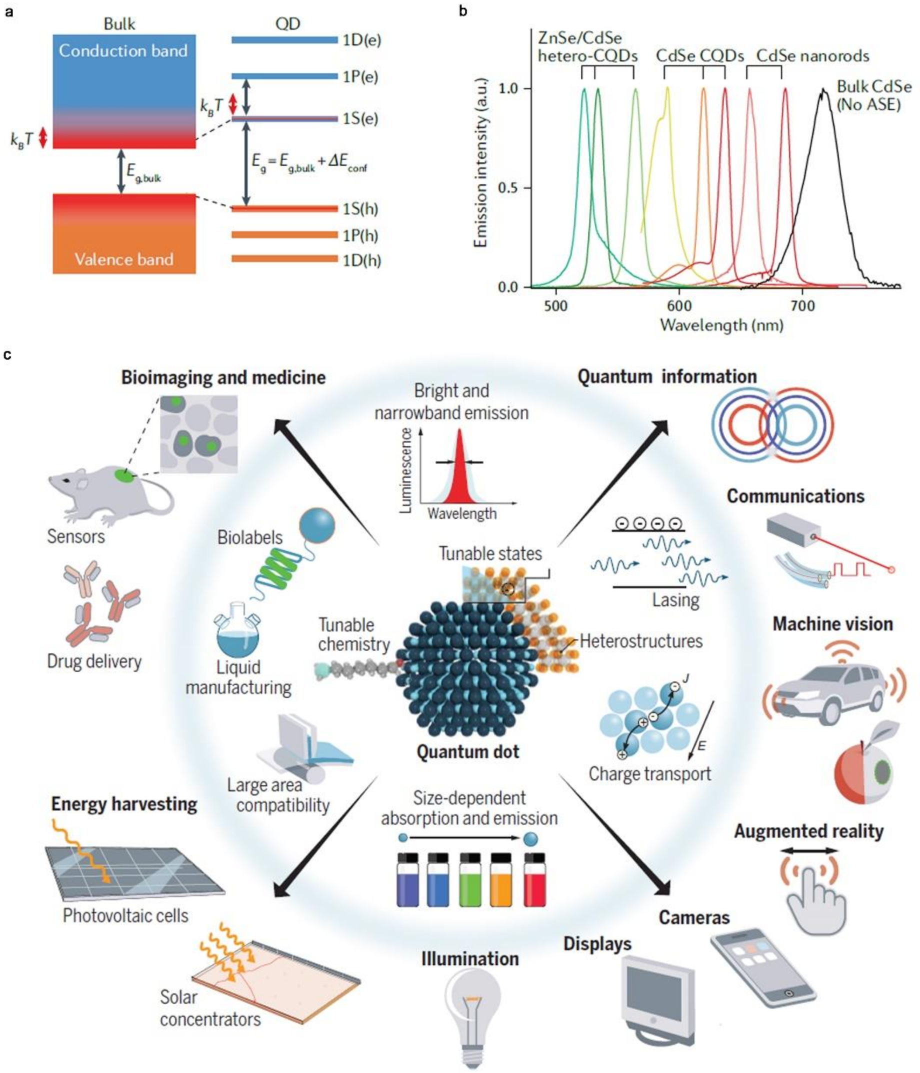

Figure 1. 1. Fundamental properties of NCs and their application. (a) Comparison of band structure between bulk and NCs.[16] (b) Energy gap tunability of NCs with varying size and composition.[16] (c) Semiconductor nanocrystals technological.[17]

1.1.2 Core/shell heterostructure

For the use of NCs in the practical light-emitting applications, it is crucial to achieve high photoluminescence quantum yield (PL QY) and stable emission. However, core only NCs exhibit low PL QY due to surface defects, which traps generated charge carriers and reacts as main non-radiative paths in the NCs. Thus, the construction of core/shell heterostructures has been employed as strategy for achieving high PL QY and stable emission of excited charge carriers in NCs.

The potential profile of NCs can be classified based on the offset between the core and shell materials (**Fig. 1.2**). The type 1 band profile, where both charge carriers are confined within the core, provides complete isolation of charge carriers from surface traps, resulting in high PL QY and stable emission. The *quasi*-type 2 band profile, where one charge carrier is confined in the core while the other is localized over the entire NC, allows for the control of the wavefunction of charge carriers by modulating the thicknesses of the shell. On the other hand, in the type 2 band profile, the electrons and holes exist in separate spaces, leading to slow radiative recombination rates and low PL QY, making it less suitable for practical applications. Therefore, type 1 and quasi-type 2 band alignments are suitable for light-emitting applications.

The successful construction of heterostructures relies on pairing appropriate semiconductor materials with the same crystal structure to achieve heteroepitaxy. However, As the lattice constants between the core and shell materials are different, interfacial defects are generated inevitably when the thickness of the shell material exceeds the critical thickness, which refers to the maximum thickness maintaining high optical properties. In addition, appropriate energy position of shell material relative to the core is essential to be satisfied for the confining charge carriers in the NCs.

To relax lattice strain in the heterostructures, previous research has proposed several solutions, such as implementing an alloyed buffer layer between the core and shell or employing spherical quantum well structures. These approaches enable to both relax interfacial strain and suppress Auger recombination, which is essential for realizing the use of NCs in the light-emitting application. In addition, the introduction of spherical quantum well (SQW) structure effectively alleviates lattice mismatch by growing the emissive layer on a seed that is the same material with the shell, resulting in an A (seed) /B (emissive layer)/A (shell) structure that allows to realize defect-free at the interface.

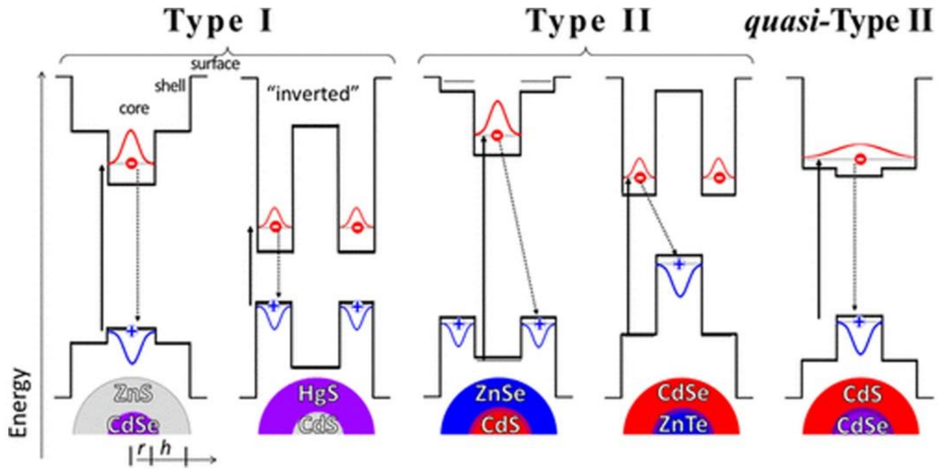

Figure 1. 2. Types of core/shell heterostructured NCs based on the band profile.[18]

1.1.3 Alloyed core

Previous studies have predominantly focused on quantum confinement effect for tuning band gap. In addition to this, alloying multi–components enables to expand tuning spectra further. The extensive synthetic efforts have expanded material envelope to various Cd–based composition such as $Cd_XZn_{1-X}Se$, $Cd_XZn_{1-X}S$, $CdSe_XS_{1-X}$ NCs. These pairs of semiconductors exhibit almost linear relationship between band gap and the compositional ratio, which allows for sophisticated band gap tunability covering all visible range (**Fig. 1.3.a–b**).

On the other hand, specific combination of semiconductor allows smaller or larger band gap relative to original band gap. For examples, $ZnSe_{1-X}Te_X$ alloy shows strong band gap bowing effect that specific alloy ratio shows smaller band gap (2.0 eV) than that of ZnSe (2.7 eV) and ZnTe (2.3 eV). This unusual effect enables realizing red emission (~2.0 eV) with the $ZnSe_{1-X}Te_X$ (**Fig. 1.3.c–d**)

The alloyed core allows for the broad control of not only band gap, but also lattice constant, which can alleviate lattice strain between core and shell. However, synthesizing homogeneous alloyed cores is challenging due to differences in the reactivity among constituent ions. Thus, relaxing the reactivity disparity through several methods such as feed ratio control, ligand and temperature control is essential for achieving uniform nucleation of core.

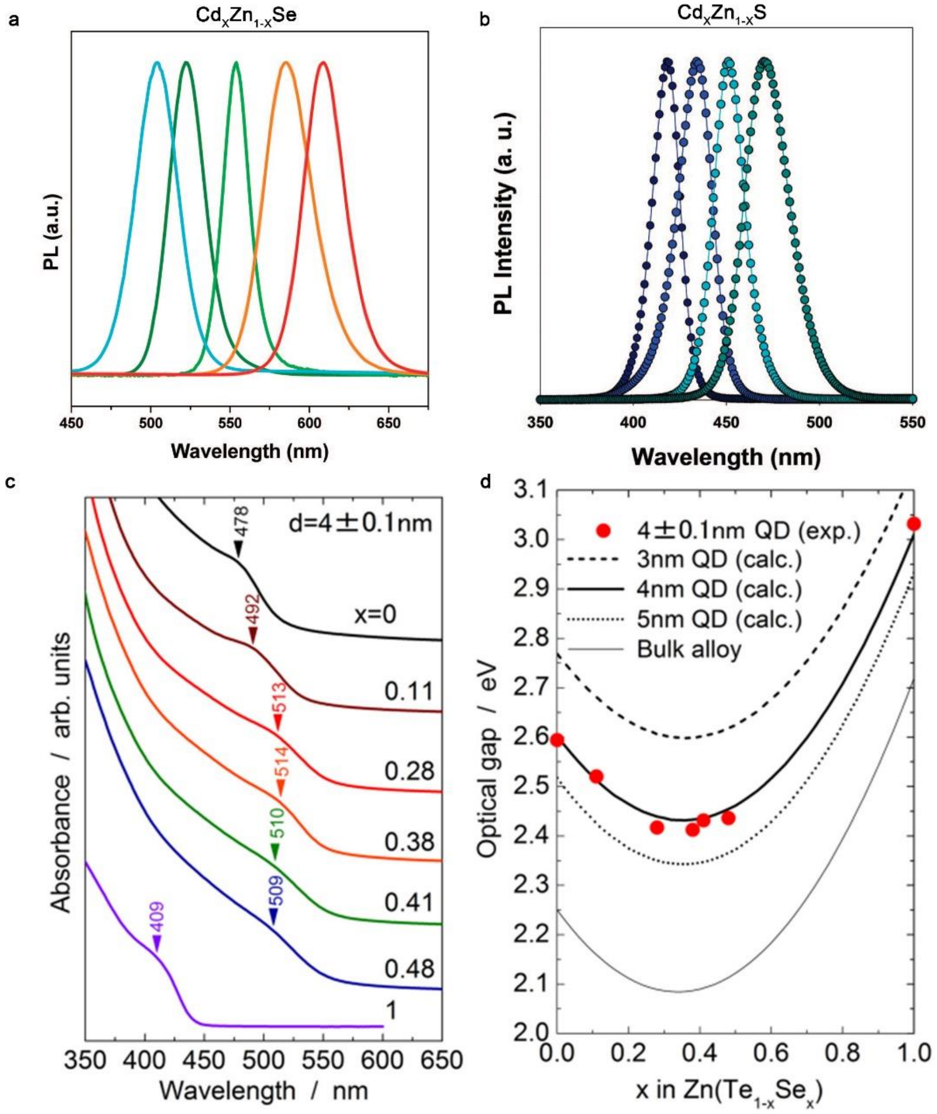

Figure 1. 3. Energy gap tunability of (a, b) CdSe−based[19,20] alloyed core. (c) Absorption spectra and (d) optical band gap of ZnSe$_X$Te$_{1-X}$ alloyed cores.[21]

1.1.4 Auger recombination

In addition to synthetic difficulties, spontaneously occurring multicarrier states, in which exciton recombination energy is transferred to the third carriers (Auger recombination, AR), complicate the realization of high-power light emitting devices (**Fig. 1.4a**). For instance, the imbalance between hole *versus* electron injection rates in NC-LEDs accumulates extra charge carriers, either electrons or holes, in NC emissive films, which leads to the low external quantum efficiency and significant efficiency roll-off at high current density regime due to AR process (**Fig. 1.4b**).[22-25] In addition, fast AR processes complicate both generating multicarrier states for optical gain and maintaining population inversion preventing from reaching the lasing regime (**Fig. 1.4c**).[13,26] Thus, precise assessment of AR characteristics of NCs is prerequisite for their light-emitting applications.

For achieving high performance in the light-emitting applications, many researchers have developed various methods to improve multicarrier QY by several methods (**Fig. 1.5**). One such method is volume scaling, which involves increasing the effective volume where charge carriers exist decreases AR. For instances, effective volume control by adjusting core size (type Ⅰ and quasi-type Ⅱ) or shell thickness (quasi-type Ⅱ) effectively suppresses AR due to relaxation of quantum confinement effect. The other method is inserting gradient layer between core and shell, which decreases the overlap of the initial and final states of the multicarrier systems effectively. Practically, compositional gradient structure is much more effective way than volume scaling.[28]

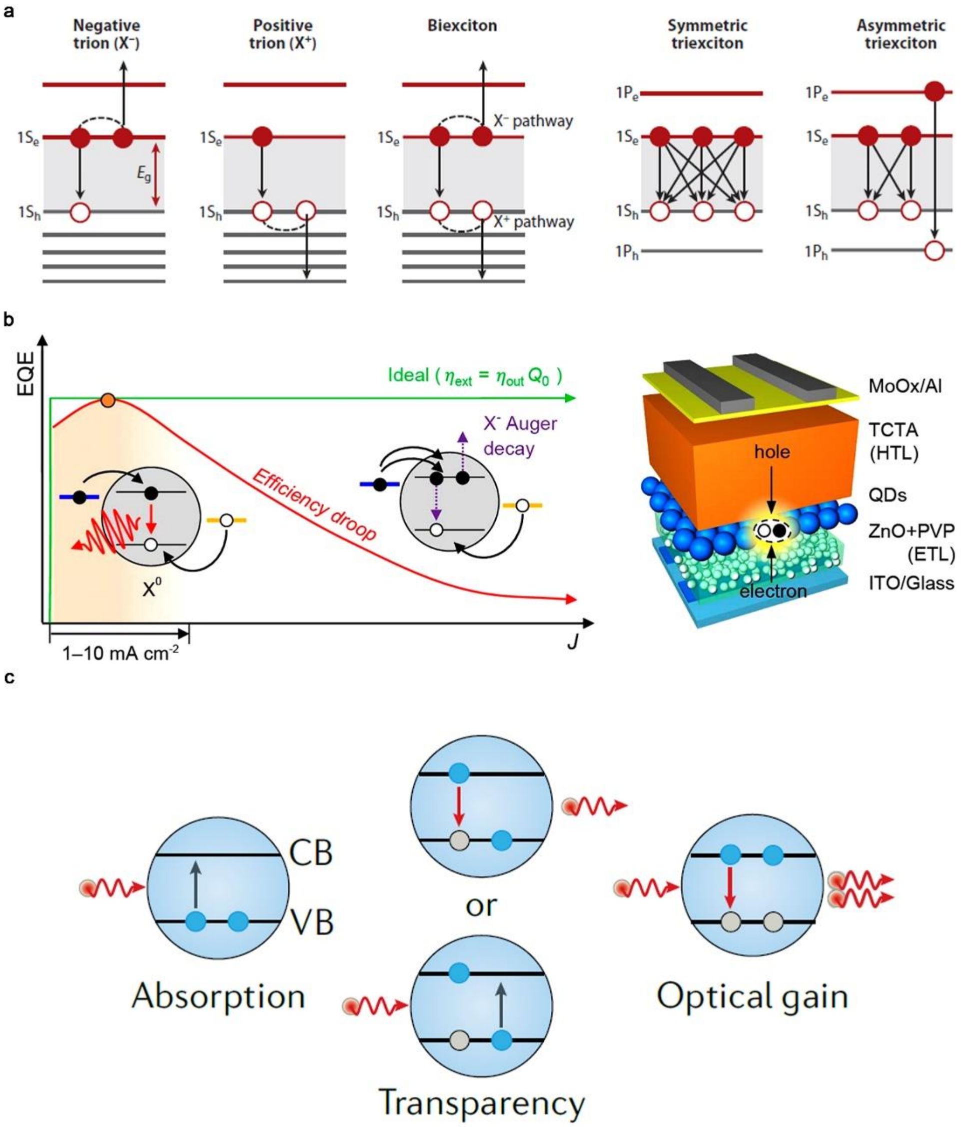

Figure 1. 4. Recombination routes in multicarrier states in the light−emitting application. (a) Carrier recombination path in the multicarrier states of the NCs[27]. Electronic states in the (b) NC−LEDs[14] and (c) NC−Lasers[16]. Imbalance of injection rates between electron and hole generates negative trions in the emissive layer. Maintaining multicarrier states for optical gain is essential for stimulated emission.

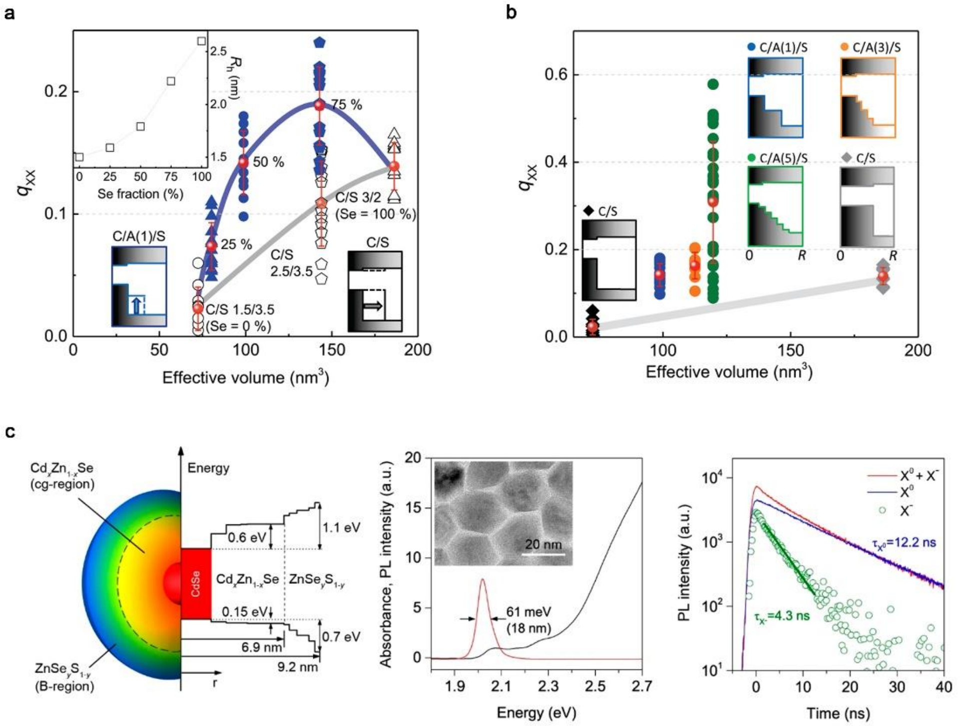

Figure 1. 5. Previous methods for suppressing Auger Recombination. (a, b) Biexciton PL QYs of the core/shell and multiple condition of core/alloy/shell NCs obtained from single−dot measurement ($g^{(2)}$).[28] (c) Band profile, TEM image, optical and photophysical properties of continuously gradient NCs.[14] Smooth potential profile plays key roles in the suppressing AR (Fig. 5(a−c)).

1.2. Environmentally benign colloidal nanocrystals

For decades, extensive efforts have achieved significant advancements in the use of Cd−based NCs for the light−emitting application such as displays, luminescent solar concentrator and lasers. The representative is CdSe/CdZnSe/ZnSeS NCs (continuously gradient NCs or cg−NCs), which exhibit near−unity PL QY and suppressed AR, enabling the realization of droop−free EL device and electrically driven amplified spontaneous emission.

However, due to the toxicity of Cd, the industrial use of Cd−based NCs is subject to strict global restrictions, which has necessitated the development of alternative materials (**Fig. 1.6**). Among these alternatives, the representatives are InP, $ZnSe_{1-X}Te_X$, $AgIn_XGa_{1-X}S_2$, $CuIn_XGa_{1-X}S_2$ NCs. In particular, InP NCs are a promising alternative due to their appropriate emission wavelength range. Specifically, it is noted that InP/ZnSe/ZnS NCs exhibit near−unity PL QYs and theoretical limited external quantum efficiency (EQE) in NC−LEDs. Besides, $ZnSe_{1-X}Te_X$/ZnSe/ZnS NCs also exhibit near−unity PL QYs across visible wavelength, and low Te ratio (X) of $ZnSe_{1-X}Te_X$ layer enables realizing blue emitting NCs. Practically, 20 % of EQE in the blue emitting NC−LEDs with $ZnSe_{1-X}Te_X$/ZnSe/ZnS NCs is reported, which is milestone of the first high performance blue emitting diodes from Cd−free NCs. but their low photostability under the ambient air currently hinders their practical use in the light emitting applications. $AgIn_XGa_{1-X}S_2$ NCs have emerged as promising down−conversion materials due to their high extinction coefficient. However, conventional shell material (*i.e.* ZnS or amorphous GaSx) are unable to suppress surface trap states emissions, which are characteristic optical properties in the $\mathrm{I}-\mathrm{III}-\mathrm{VI}_2$ semiconductors. This improper pairing of core and shell generates interfacial traps, resulting in broad trap emission and low PL QY, which hinders their use in the display applications. $CuIn_XGa_{1-X}S_2$ NCs exhibit similar properties with $AgIn_XGa_{1-X}S_2$ NCs such as broad emission linewidth, large stoke shift and high extinction coefficient. On the other hand, small band gap of $CuInS_2$ NCs enables absorbing all visible light, boosting their use in the solar cell or luminescent solar concentrator rather than display.

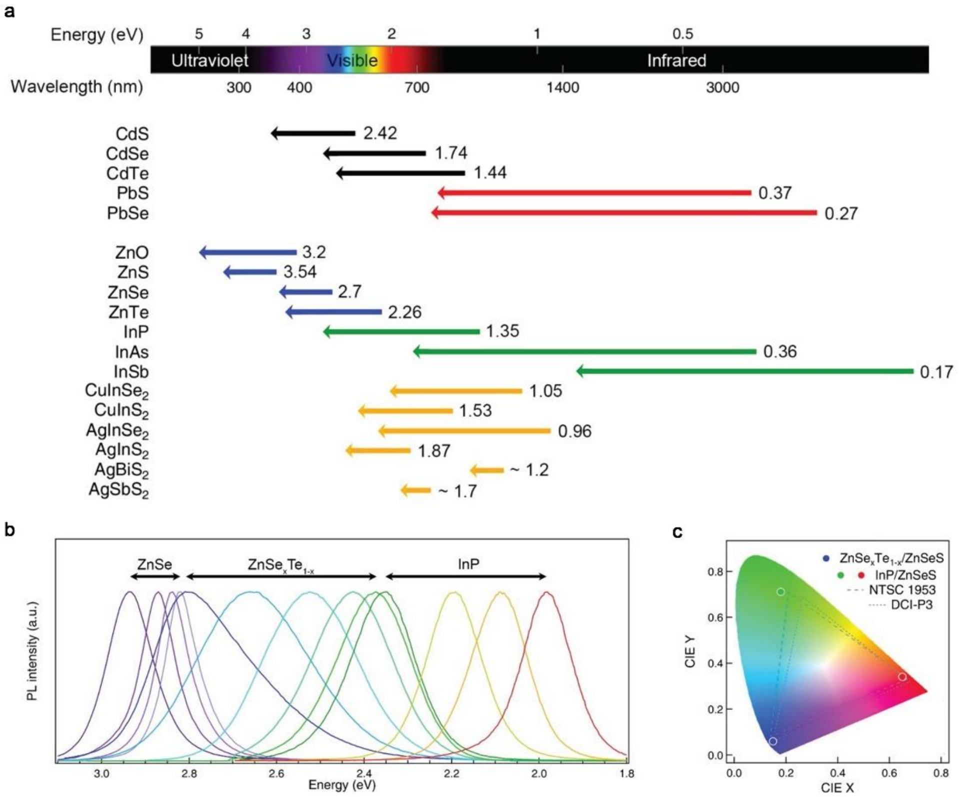

Figure 1. 6. Energy gap tunable ranges of various NCs. (a) Size−dependent energy gap tunability of various compositional NCs. (b) PL spectra and (c) CIE color chart of environmentally benign NCs across visible wavelength.[29]

Chapter 2.① Synthesis of *quasi*–type Ⅱ ZnSe/ZnSe$_{1-X}$Te$_X$/ZnSe spherical quantum well nanocrystals

2.1. Introduction

Colloidal semiconductor NCs, in which charge carriers are confined in all three dimensions, have received tremendous interest as next–generation light–emissive materials owing to their unique optical properties such as broad absorption but narrow emission bandwidth, and size dependent band gap tunability across visible to near IR.[1–3,30] In addition to the quantum confinement effect, the heterojunction in NCs enables further control over the spatial distribution of charge carriers and their dynamics, boosting practicable use of NCs in displays,[31–33] luminescent solar concentrators (LSCs)[34,35] and biomarkers.[36] The representative is the core/shell heterostructures, wherein the charge carriers in the core are decoupled from the surface trap states to award photochemical stability and near–unity luminescence efficiency at the room temperature.[4,37,38]

Among the core/shell heterostructures, NCs with the *quasi*–type II band alignment have been of particular interest due to its great potential for controlling the interactions among

---

① This chapter is based on paper from Chang, J. H.; Lee, H. J.; Rhee, S.; Hahm, D.; Jeong, B. G.; Nagamine, G.; Padilha, L. A.; Char, K.; Hwang, E.; Bae, W. K. Pushing the Band Gap Envelope of Quasi–Type II Heterostructured Nanocrystals to Blue: ZnSe/ZnSe1–X Te X/ZnSe Spherical Quantum Wells. *Energy Mater. Adv.* 2021, *2021*, No. 3245731.

charge carriers. In *quasi*–type II heterostructured NCs, one charge carrier is confined in the core, whereas the other charge carrier is delocalized over the entire volume, and thus controlling the geometry or the dimension of the core and the shell allows to manage electron and hole wavefunctions independently. The distinguished feature of *quasi*–type II heterostructured NCs is the suppression of non–radiative Auger recombination processes of multi–carriers (more than one electron and one hole),[26,39,40] which is the key to high efficiency light–emitting diodes and low threshold lasers.

To achieve *quasi*–type II NC emitters, two semiconductor materials having similar conduction band edge (CBE) energy levels or valence band edge (VBE) energy level need to form a contact without the interfacial defects. So far, reports on *quasi*–type II NCs have been limited to few cases (*i.e.*, CdSe/CdS,[39–42] PbSe/CdSe,[43] and $CuInS_2$/CdS[44,45]). The lack of materials choice for *quasi*–type II NCs restricts the accessible emission wavelength to red to NIR, which in return hinders their use in light–emitting applications that demand a wide range of visible colors.

Herein we demonstrate a new class of *quasi*–type II nano–emitters formulated in ZnSe/$ZnSe_{1-X}Te_X$/ZnSe seed/spherical quantum well/shell heterostructures (SQW). The composition of $ZnSe_{1-X}Te_X$ emissive layer and the dimension of ZnSe shell layer are engineered to tailor the distribution and energy of hole and electron wavefunctions and their interactions. In addition, a comprehensive study across spectroscopic analysis, structural analysis and calculation is conducted to assess the role of the composition and the geometry of given SQW NCs on their photophysical properties. Finally, we exemplify dichromatic white light-emitting diodes enabled by excellent luminescence efficiency of resulting SQW NCs in a range of emission colors from blue to orange.

2.2. Experimental Section

Materials. Zinc acetate ($Zn(ac)_2$, 99.99 %), selenium (Se, 99.9 %), sulfur (S_8, 99.9 %), oleic acid (OA, 99 %), n-trioctylphosphine (TOP, 99 %), and 1-octadecene (ODE, 99 %) were purchased from Uniam. Diphenylphosphine (DPP, 98 %), Zinc acetate dihydrate ($Zn(ac)_2 \cdot 2H_2O$, ≥ 98 %), 1-dodecanethiol (DDT, 98 %), potassium hydroxide (KOH, 90%), and butylamine (99.5 %) were purchased from Aldrich. Tellurium powder (Te, 99.999 %) was purchased from Alfa Aesar. Poly[(9,9-bis(3′-N,N-dimethylamino)propyl)-2,7-fluorene)-alt-2,7-(9,9-ioctylfluorene) (PFN) was purchased from 1-materials. 2,2’-bis(4-(carbazol-9-yl)phenyl)-biphenyl (BCBP, > 99.9 %) was purchased from Organic Semiconductor Materials (OSM, Korea). MoO_3 and Al were purchased from iTASCO (Korea). All chemicals are used as received.

Synthesis of ZnSe/$ZnSe_{1-X}Te_X$ seed/emissive layer structure. All synthesis was carried out under the inert atmosphere through the Schlenk line technique. 1.2 ml of 0.5 M $Zn(OA)_2$ prepared from $Zn(ac)_2$, OA and ODE, and 15 ml of ODE were stirred and degassed at 110 °C in a 3-neck round flask. After one hour of degassing to remove water and oxygen completely, it was filled with N_2. Then, 1 ml of 0.2 M DPPSe, prepared from 4 mmol Se powder, 2 ml DPP and 18 ml anhydrous toluene, was injected at 230 °C and After 1 minute ZnSe seed is synthesized (r = 0.6 nm), 0.5 M TOPTe (0.02 ml

(X = 0.03), 0.06 ml (X = 0.1), 0.12 ml (X = 0.2), 0.2 ml (X = 0.33), 0.3 ml (X = 0.5)), prepared from 50 mmol Te powder and 100 ml TOP, and 2 M TOPSe (0.145 ml (X = 0.03), 0.135 ml (X = 0.1), 0.12 ml (X = 0.2), 0.1 ml (X = 0.33), 0.075 ml (X = 0.5)) were injected to grow $ZnSe_{1-X}Te_X$ emissive layer at same temperature and maintained for 30 minutes. After that, heated to 300 °C for 15m to grow seed/emissive layer completely (r = 0.6 nm, l = 1.2 nm).

Synthesis of $ZnSe/ZnSe_{1-X}Te_X/ZnSe$ and $ZnSe/ZnSe_{1-X}Te_X/ZnSe/ZnS$ NCs. $ZnSe/ZnSe_{1-X}Te_X/ZnSe$ NCs were synthesized injecting additional precursor to grow ZnSe outer shell, at first ZnSe shell, 2 ml $Zn(OA)_2$ (0.5 M stock solution) and 0.25 ml TOPSe (2 M stock solution) were injected and maintained at 320 °C for 30 minutes (r = 0.6 nm, l = 1.2 nm, h = 0.6 nm). For consecutive thick ZnSe outer shell growth, $Zn(OA)_2$ 3.4, 5.2, 7.8 ml and TOPSe 0.425, 0.625, 0.975 ml were injected in sequence at 320 °C for 60 minutes per each step (r = 0.6 nm, l = 1.2 nm, h = 1.2, 1.8, 2.4 nm). To passivate surface trap, thin ZnS shell was grown on $ZnSe/ZnSe_{1-X}Te_X/ZnSe$ (r = 0.6 nm, l = 1.2 nm, h = 0.6, 1.2, 1.8, 2.4 nm) by same process but different amounts of precursors. $Zn(OA)_2$ 3.4, 5.2, 7.8, 10 ml and DDT 0.2, 0.3, 0.45, 0.58 ml were injected respectively to different outer ZnSe shell thickness NCs at 300 °C for 60 minutes. Synthesized NCs were purified repeatedly in glove box *via* precipitation (30 ml of acetone)/redispersion (10 ml of anhydrous toluene) method, diluted at a concentration of 20 g/ml (anhydrous toluene) and kept in glove box refrigerator for device fabrication and UPS measurement.

Device fabrication. Before ZnSe/ZnSe$_{1-X}$Te$_X$/ZnSe NC−LEDs fabrication, patterned indium tin oxide (ITO) glass substrates were ere cleaned with acetone, isopropyl alcohol, and deionized water with 15 min respectively. First, ZnO NPs solution (20 mg/ml in butanol) was spun−cast on an ITO substrate at a spin rate of 2000 rpm for 40 seconds followed by annealing at 100 ° C for 30 min. Afterward, PFN solution (0.5 mg/ml in methanol/acetic acid mixed solvent) was spun−cast on the ZnO−coated substrates at a spin rate of 4000 rpm for 30 seconds. The PFN−coated substrates were dried for 30 minutes under vacuum condition. ZnSe/ZnSe$_{1-X}$Te$_X$/ZnSe/ZnS NC solutions (10 mg/ml in toluene) were spun−cast at 4000rpm for 30 seconds to form 2 − 3 monolayers of NCs. Finally, BCBP (60 nm), MoO$_3$ (10 nm) and Al (130 nm) layers were thermally evaporated under a vapor pressure of 1×10^{-6} Torr. The deposition rates of each layer were 0.5 − 1 Å/s for BCBP, 0.1 − 0.2 Å/s for MoO$_3$, and 3 − 5 Å/s for Al.

Optical and Structural Characterization. Absorption and photoluminescence spectra were obtained with Shimadzu UV−1800 and Horiba FluoroMax−4, respectively. Absolute PL QY was measured with Otsuka QE−2000 at the same absorbance (0.1) in toluene with the 450 nm excitation wavelength. High−resolution TEM images were obtained from FEI Tecnai−F20. The current–voltage–luminance (I–V–L) characteristics of the NC−LEDs were measured using a Keithley−236 source−

measure unit and a Keithley−2000 multimeter with a calibrated Si photodiode (Hamamatsu, S5227−1010BQ). The electroluminescence spectra of the devices were obtained by a spectroradiometer (Konica Minolta, CS−2000). The crystalline structures of NCs were investigated by synchrotron X−ray diffraction measurements (JP/D/MAX−2500H, X−ray wavelength = 1.5406 Å) The XRD data were acquired in the 2θ range between 20° and 60° at a scan rate of 1° /min. The XRD patterns of ZnSe and $ZnSe_{1-X}Te_X$ in $ZnSe/ZnSe_{1-X}Te_X$ NCs were decoupled by subtracting a separately measured XRD pattern of ZnSe NCs from that of $ZnSe/ZnSe_{1-X}Te_X$ NCs, considering the volume of each component.

2.3. Results and Discussion

As a new class of *quasi*−type II NCs, we construct heterojunctions made of $ZnSe_{1-X}Te_X$ emissive layer passivated by ZnSe shell layer for the following reasons. First, the band gap of $ZnSe_{1-X}Te_X$ bulk semiconductors can cover a wide range of visible regions, from blue to orange, depending on the alloy compositions. In addition, the energy offset between conduction band edge energy levels (E_{CBE}) of ZnSe and $ZnSe_{1-X}Te_X$ is similar to the thermal energy of room temperature (k_BT = 25 meV), allowing the electron wavefunction to spread over the entire volume of NCs. Furthermore, the crystal structure of

ZnSe and ZnTe are both zincblende, and thus the epitaxial growth of ZnSe on $ZnSe_{1-X}Te_X$ is achievable.

Heterostructuring $ZnSe_{1-X}Te_X$ and ZnSe in a conventional core/shell geometry entails the nucleation of $ZnSe_{1-X}Te_X$ emissive core and the epitaxial growth of ZnSe shell, but both appear to be challenging to be experimentally realized *via* wet-chemistry. First, the significant reactivity difference between Se and Te precursors often results in the independent nucleation of ZnSe and ZnTe instead of the formation of homogeneous $ZnSe_{1-X}Te_X$ core, particularly at high Te contents ($X \geq 0.30$). In addition, the large lattice mismatch between $ZnSe_{1-X}Te_X$ emissive core and ZnSe shell promotes the creation of misfit defects at the interface, which gives rise to the reduction of PL QYs with increasing shell thicknesses.[46] The difficulties in the synthesis of homogenous $ZnSe_{1-X}Te_X$ emissive cores and defect-free growth of ZnSe shell on $ZnSe_{1-X}Te_X$ impedes the realization of high quality $ZnSe_{1-X}Te_X$/ZnSe core/shell heterostructured NCs with varying Te contents.[47-49]

As a mean to relieve the structural stress between $ZnSe_{1-X}Te_X$ emissive layer and ZnSe shell, we adopt the concept of coherently strained multilayered heterostructures.[50] Specifically, we design the ZnSe/$ZnSe_{1-X}Te_X$/ZnSe seed/spherical quantum well/shell heterostructures (**Fig. 2.1a**), in which the $ZnSe_{1-X}Te_X$ emissive layer is successively grown on top of the ZnSe seed and passivated by the ZnSe shell layer. In a SQW geometry, the sandwiched emissive layer is strained by the presence of underlying seed to relieve the structural stress against the shell layer, enabling to attain high luminescence efficiency even with thick−shells.50,51 Besides, the growth of $ZnSe_{1-X}Te_X$ emissive layer requires the injection of mixed Se and Te precursors at the concentration below the critical concentration for nucleation of ZnSe and ZnTe, which allows to avoid the problems originated from the inhomogeneity in size and composition among NCs.

As a first step, we optimize the reaction condition for the synthesis of ZnSe seeds with a radius (r) of 0.6 nm and further ZnSe growth up to 1.8 nm. At the given homoepitaxy growth condition, we replace in part of Se precursor with Te precursor to grow $ZnSe_{1-X}Te_X$ emissive layer. Resulting NCs show uniform size distribution (std ~ 10 %) and single gaussian PL emission regardless of Te contents. Small particles or side PL peaks, which are the signs of homogenous nucleation of ZnSe or ZnTe, do not appear during the growth. The composition analysis in chorus with the size and shape monitoring confirms that the Te content (X) of $ZnSe_{1-X}Te_X$ emissive layer remains unchanged along the radial direction. These results coherently attest the successive growth of homogeneous $ZnSe_{1-X}Te_X$ emissive layers on the surface of ZnSe seeds. The sequential growth of ZnSe on top of $ZnSe/ZnSe_{1-X}Te_X$ NCs at the given reaction condition results in $ZnSe/ZnSe_{1-X}Te_X/ZnSe$ SQW NCs.

Figure 2.1 shows the structure and optical properties of the resulting $ZnSe/ZnSe_{1-X}Te_X/ZnSe$ SQW NCs. In such a geometry, the hole is strongly confined within the $ZnSe_{1-X}Te_X$ emissive layer, whereas the electron is delocalized over the entire volume of the ZnSe/ZnSe$_{1-X}$Te$_X$/ZnSe SQW NCs (**Fig 2.1c**). The dimensions of ZnSe seed (radius, *r*) and ZnSe$_{1-X}$Te$_X$ emissive layer (thickness, *l*) are fixed to be r = 0.6 nm and l = 1.2 nm for all samples, and thus the variation in the ZnSe shell thickness (*h*) determines the distribution of electron wavefunction and its energy. By contrast, the hole wavefunction is solely affected by the composition of ZnSe$_{1-X}$Te$_X$ emissive layer (*X*). Engineering these parameters permits to tune the emission wavelength of heterostructured NCs from blue (peak PL @ 450 nm) to orange (peak PL @ 600 nm) (**Fig 2.1b** and **d**).

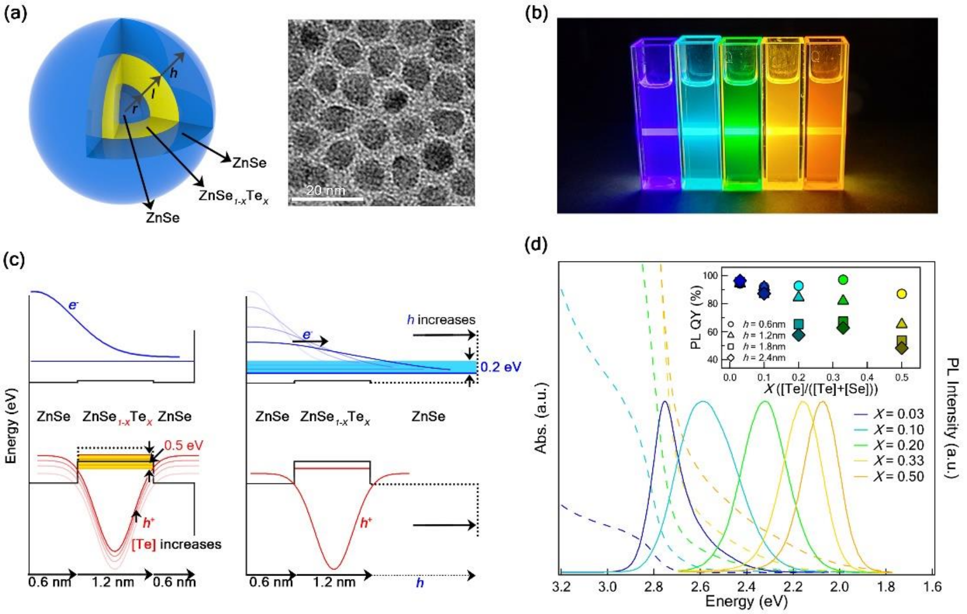

Figure 2. 1. Structural characteristics and optical properties of ZnSe/ZnSe$_{1-X}$Te$_X$/ZnSe SQW NCs. (a) Schematic illustration (left) and transmission electron microscopy (TEM) image (right) of ZnSe (r = 0.6 nm)/ZnSe$_{1-X}$Te$_X$ (l = 1.2 nm)/ZnSe (h = 2.4 nm) NCs. Scale bar is 20 nm. (b) A photographic image of ZnSe (r = 0.6 nm)/ZnSe$_{1-X}$Te$_X$ (l = 1.2 nm)/ZnSe (h = 2.4 nm) NC dispersions with varying Te ratios. X varies from 0.03 (left) to 0.50 (right). (c) Schematics illustrating the bulk band structure of ZnSe/ZnSe$_{1-X}$Te$_X$/ZnSe NC (black solid line) and electron (blue) and hole (red) wavefunction at their lowest quantized energy state. The change in Te content (X) alters the energy states for the hole (left), whereas the modulation of ZnSe shell thickness alters the energy states for electron (right). (d) Absorption (dashed line) and PL spectra (solid line) of ZnSe (r = 0.6 nm)/ZnSe$_{1-X}$Te$_X$ (l = 1.2 nm)/ZnSe NCs with varying Te ratios ($0.03 \leq X \leq 0.50$) and ZnSe shell thicknesses

($0 \leq h \leq 2.4$ nm). The inset displays PL QYs of ZnSe/ZnSe$_{1-X}$Te$_X$/ZnSe NCs with varying Te contents ($0.03 \leq X \leq 0.50$) and ZnSe shell thicknesses (h = 0.6, 1.2, 1.8, and 2.4 nm).

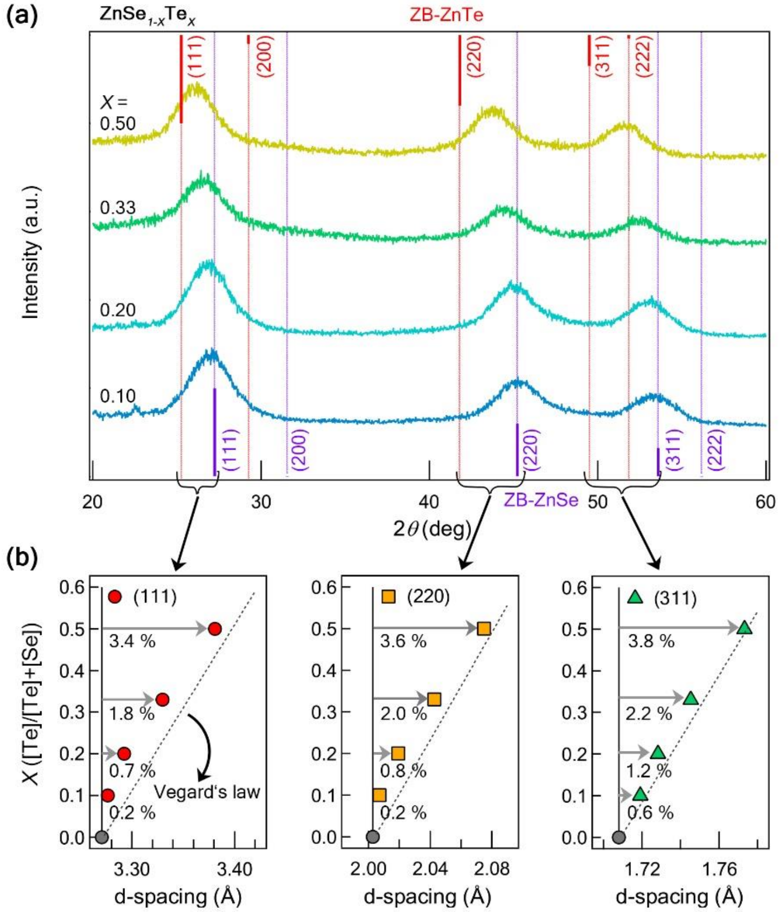

Figure 2. 2. Lattice strain relaxation in ZnSe/ZnSe$_{1-X}$Te$_X$/ZnSe SQW NCs. (a) XRD patterns of ZnSe$_{1-X}$Te$_X$ emissive layers with varying Te contents (X varies from 0.10 (bottom) to 0.50 (top)). The XRD patterns of ZnSe$_{1-X}$Te$_X$ and ZnSe in ZnSe/ZnSe$_{1-X}$Te$_X$ NCs were decoupled by subtracting separately measured XRD patterns of ZnSe seed from that of ZnSe/ZnSe$_{1-X}$Te$_X$ NCs, by considering the volume of each component. The XRD patterns are vertically shifted for visual clarity. The characteristic diffraction peaks of bulk zincblende ZnSe (violet, bottom, JCPDS No. 65−9602) and ZnTe (red, top, JCPDS No. 15−0746) are displayed for comparison. (b) *d*−

spacing for (111) (red circle (left)), (220) (orange square, (middle)), and (311) (green triangle (right)) peaks and the estimated d-spacing of bulk $ZnSe_{1-X}Te_X$ alloys from Vegard's law (black broken line) are displayed for comparison.

A notable feature of the resulting NCs is the excellence in PL QYs. Specifically, passivating additional thin ZnS shell layer (0.6 nm) on the exterior of ZnSe/$ZnSe_{1-X}Te_X$/ZnSe SQW NCs assists to diminish the influence of surface trap states on the charge carrier wavefunctions, resulting in over 90 % PL QY of NCs even the cases with high Te contents (**Fig. 2.1d inset**). The near-unity PL QYs for ZnSe/$ZnSe_{1-X}Te_X$/ZnSe/ZnS SQW NCs clearly contrast with previous reports on $ZnSe_{1-X}Te_X$/ZnSe/ZnS core/shell NCs with similar structural parameters (PL QY = 52 % for $X = 0.02$, ZnSe shell thickness = 1.5 nm, ZnS shell thickness = 0.4 nm),46 which in turn implies that the formation of misfit defects at the interface between $ZnSe_{1-X}Te_X$ emissive layer and ZnSe surround media is effectively suppressed in the SQW platform.

To validate the impact of the geometry on the lattice strain relaxation between $ZnSe_{1-X}Te_X$ and ZnSe, we characterize the lattice constant of $ZnSe_{1-X}Te_X$ emissive layers grown on ZnSe seeds (**Fig. 2.2**). We obtain the x-ray diffraction patterns of ZnSe/$ZnSe_{1-X}Te_X$ core/spherical quantum well samples and decouple the contribution of ZnSe seeds to extract the patterns of $ZnSe_{1-X}Te_X$ only (See experimental section). $ZnSe_{1-X}Te_X$ films are well-known to follow Vegard’ s law in a wide range of alloy ratios ($0 < X < 0.9$) when grown in bulk films.52 The diffraction patterns of $ZnSe_{1-X}Te_X$ emissive layers clearly deviate from the lattice constant estimated from Vegard’ s law (**Fig. 2.2b**), indicating that the $ZnSe_{1-X}Te_X$ spherical quantum well layers are strained to fit into the ZnSe sublayer.

Specifically, in the SQW platform, the lattice mismatch between ZnSe and $ZnSe_{0.8}Te_{0.2}$ emissive layer is suppressed by 55 %, 49 %, 23 % along (111), (220), and (311) directions compared to the bulk parameters, respectively. The reduction in the lattice mismatch between ZnSe and $ZnSe_{1-X}Te_{X}$ alleviates the lattice stresses at the interface between ZnSe and $ZnSe_{1-X}Te_{X}$ and aids to extend the critical thickness for the defect formation during the SQW NC growth, allowing ZnSe/$ZnSe_{1-X}Te_{X}$/ZnSe SQW NCs to reach near-unity PL QYs.

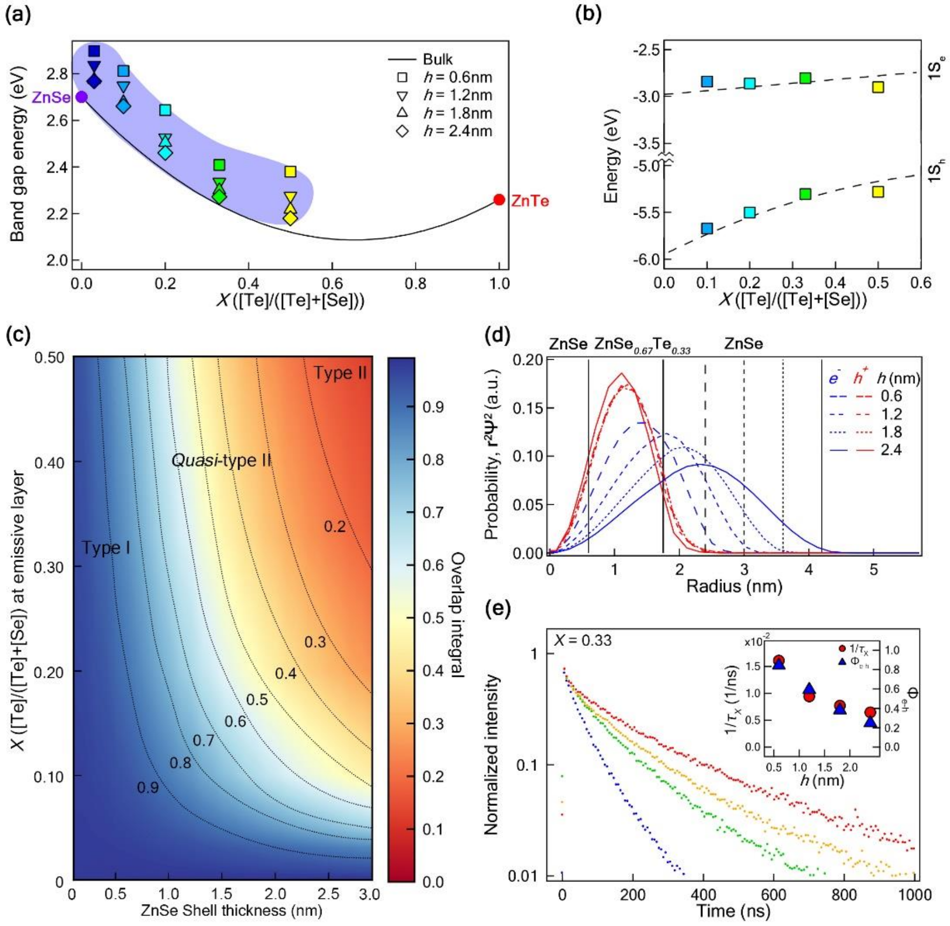

Figure 2. 3. Electronic features and photophysical properties of ZnSe/ZnSe$_{1-X}$Te$_X$/ZnSe NCs. (a) Band gap energy of ZnSe/ZnSe$_{1-X}$Te$_X$/ZnSe NCs with varying Te contents (X = 0.03, 0.10, 0.20, 0.33, 0.50) and ZnSe shell thicknesses (h = 0.6, 1.2, 1.8, 2.4 nm). The bulk band gap energy of ZnSe (violet circle at the left y axis) and ZnTe (red circle at the right y axis) are displayed for comparison. (b) The lowest quantized energy states for electron (1S$_e$) and hole (1S$_h$) of ZnSe (r = 0.6 nm)/ZnSe$_{1-X}$Te$_X$ (l = 1.2 nm)/ZnSe (h = 0.6 nm) NCs with varying Te contents. 1S$_h$ and 1S$_e$ of NCs are obtained from

ultraviolete photoelectron spectroscopy in chorus with UV−Vis absorption spectroscopy. (c) Calculated electron−hole overlap integrals of ZnSe (r = 0.6 nm)/$ZnSe_{1-X}Te_X$ (l = 1.2 nm)/ZnSe NCs with varying Te ratios and ZnSe shell thicknesses. (d) Radial probability of electron and hole wavefunctions and (e) PL decay dynamics of ZnSe (r = 0.6 nm)/$ZnSe_{0.66}Te_{0.33}$ (l = 1.2 nm)/ZnSe NCs with varying ZnSe shell thicknesses (0.6 nm $\leq h \leq$ 2.4 nm). The inset shows radiative decay rates of single exciton ($1/\tau_x$) and electron and hole overlap integrals (Φ_{e-h}) of each samples.

The achievable emission window of ZnSe/ZnSe$_{1-X}$Te$_X$/ZnSe SQW NCs by varying the composition of ZnSe$_{1-X}$Te$_X$ and the dimension ranges from blue (450 nm, 2.76 eV) to orange (600 nm, 2.07 eV), which exceeds that of bulk ZnTe ($E_{g,ZnTe}$ = 2.3 eV) (**Fig. 2.3a**). The wide-ranging band gap tunability is attributed to the unusual strong band gap bowing of ZnSe$_{1-X}$Te$_X$,[53] which is given by $E_{g,ZnSe_{1-X}Te_X} = X \cdot E_{g,ZnTe} + (1-X) \cdot E_{g,ZnSe} - b_{ZnSe_{1-X}Te_X} \cdot X \cdot (1-X)$ (eq. 1) where X denotes the Te content in ZnSe$_{1-X}$Te$_X$ and $b_{\mathrm{ZnSe}_{1-X}\mathrm{Te}_x}$ is the bowing parameter (1.45 eV).53 We note that the band gap bowing parameters of ZnSe$_{1-X}$Te$_X$ is substantially large compared to the cases with ZnSe$_{1-X}$S$_X$ or Cd$_{1-X}$Zn$_X$Se alloys ($b_{\mathrm{ZnSe}_{1-X}\mathrm{S}_x}$ = 0.41 eV, $b_{Cd_{1-X}\mathrm{Zn}_x Se}$ = 0.35 eV).[54]

The strong band gap bowing could stand for the strong bowing in either the conduction band edge energy level (E_{CBE}) or valence band edge energy level (E_{VBE}) of ZnSe$_{1-X}$S$_X$, or combination of both, whose impact to the distribution of electron and hole wavefunctions and their recombination processes varies significantly. So far, the key parameters (*e.g.*, the band position and the effective masses of charge carriers (m_e*, m_h*)) for ZnSe$_{1-X}$Te$_X$ alloys are largely missing. To gain band position of ZnSe$_{1-X}$Te$_X$ alloy NCs, we conduct spectroscopic analysis on ZnSe/ZnSe$_{1-X}$Te$_X$/ZnSe SQW NCs in parallel with simulation on bulk ZnSe$_{1-X}$Te$_X$ alloys (**Fig 2. 3a,b**). The ultraviolet photoemission spectroscopy (UPS) on ZnSe/ZnSe$_{1-X}$Te$_X$/ZnSe SQW NCs with varying Te ratios allows to measure the quantized energy state of hole ($1S_h$), and the UV−Vis spectroscopy enables to estimate the quantized energy state of electron ($1S_e$) (**Fig 2.3b**). The quantum mechanical calculation in ZnSe/$ZnSe_{1-X}Te_X$/ZnSe SQW NCs allows us to approximate energy positions (E_{CBE} and E_{VBE}) and effective masses of charge carriers for $ZnSe_{1-X}Te_X$ alloys with varying Te contents. The experimental results show that the unusual band gap bowing of $ZnSe_{1-X}Te_X$ alloys is a results of the strong bowing of E_{VBE} of $ZnSe_{1-X}Te_X$ alloys. In fact, E_{CBE} of $ZnSe_{1-X}Te_X$ alloys varies linearly along with Te contents.

Fig 2.3c displays the overlap integral of ZnSe (r = 0.6 nm)/$ZnSe_{1-X}Te_X$ (l = 1.2 nm)/ZnSe SQW NCs as a function of the Te ratio ($0 \le X \le 0.5$) and the ZnSe shell thickness ($0 \le h \le$ 3.0 nm). The asymmetic changes in E_{CBE} and E_{VBE} of $ZnSe_{1-X}Te_X$ alloys allow constructing *quasi*−type II band alignment across ZnSe seed, $ZnSe_{1-X}Te_X$ emissive layer, and ZnSe shell layer, in which the electron wavefunction is delocalized over the entire volume, whereas the hole wavefunction is strongly confined within the $ZnSe_{1-X}Te_X$ emissive layer (**Fig 2.3d**). In a given ZnSe (r = 0.6 nm)/$ZnSe_{1-X}Te_X$ (l = 1.2 nm)/ZnSe geometry, the quantum confinement effect is only valid to electron wavefunctions and the energy of hole wavefunction is primarily governed by the composition of $ZnSe_{1-X}Te_X$ emissive layer. The chosen variation in the composition (X) of $ZnSe_{1-X}Te_X$ emissive layer and the ZnSe shell thickness (h) modulates the energy levels of $1S_h$ and the $1S_e$ of NCs by 0.5 eV and 0.2 eV, respectively, and the combination of both enables to engineer the optical band gap of *quasi*–type II NCs from 2.07 eV to 2.76 eV.

The electronic structure of given NCs is similar to the case of *quasi*–type II heterostructures made of CdSe and CdS, but the variation in electron and hole overlap integral appears to be more dramatic than the case with CdSe and CdS.[39] For example, the growth of ZnSe shell from 0.6 nm to 3.0 nm reduces the electron and hole overlap integral of ZnSe (r = 0.6 nm)/$ZnSe_{0.67}Te_{0.33}$ (l = 1.2 nm)/ZnSe SQW NCs from 0.9 to 0.2, which accompanies the substantial change in the single exciton recombination rate from 0.0161 ns^{-1} to 0.0064 ns^{-1} (**Fig 2.3e**). The wider window to modulate the electron and hole wavefunctions is important not only because it provides optical band gap tunability of *quasi*–type II NCs to complement with that of previously reported *quasi*–type II NCs,[39–45] but also promises the capability to engineer the multicarrier dynamics of NCs that is the key for realizing non–blinking quantum–emitters or high power light sources. Indeed, trion lifetime measurements indicate that multicarrier dynamics in ZnSe (r = 0.6 nm)/$ZnSe_{0.67}Te_{0.33}$ (l = 1.2 nm)/ZnSe/ZnS SQWs are similar to those measured in CdS/CdSe/CdS SQWs,[51] and about one order of magnitude slower than the ones reported for regular Type I core/shell nanocrystals.[55]

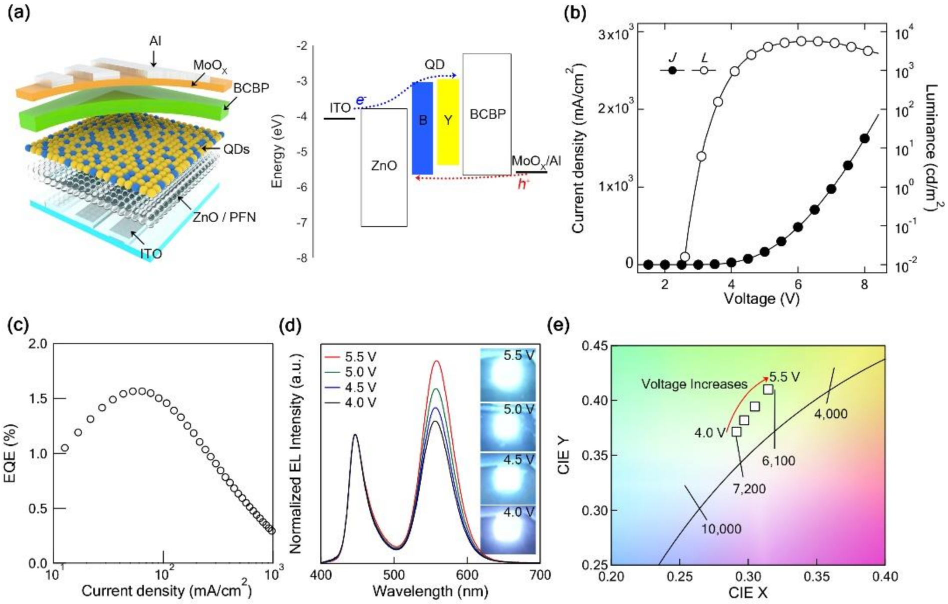

Figure 2. 4. Device characteristics of dichromatic white NC−LED employing blue− and yellow−emitting ZnSe/ZnSe$_{1-X}$Te$_X$/ZnSe SQW NCs. (a) Schematic illustrations of dichromatic white NC−LED employing blue− and yellow−emitting ZnSe/ZnSe$_{1-X}$Te$_X$/ZnSe SQW NCs (left) and its energy band diagram (right). (b) Current density−voltage−luminance characteristics and (c) external quantum efficiency (EQE) *versus* current density of dichromatic white NC−LED. (d) The normalized EL spectra of white NC−LED operated at different applied voltages. (e) The CIE 1931 color space chromaticity diagram demonstrating the color coordinates of EL spectra of white NC−LED operated at different applied voltages.

As a mean to exploit high PL QYs of SQW NCs in a wide range of emission wavelength, we exemplify dichromatic white NC−LEDs by employing the mixed layer of blue− and yellow−emitting ZnSe/$ZnSe_{1-X}Te_X$/ZnSe/ZnS SQW NCs (**Fig 2.4a**). Specifically, the dimensions and compositions of blue− and yellow−emitting NCs are formulated in ZnSe (r = 0.6 nm)/$ZnSe_{0.97}Te_{0.03}$ (l = 1.2 nm) /ZnSe (h = 0.6 nm)/ZnS (H = 0.6 nm) and ZnSe (r = 0.6 nm)/$ZnSe_{0.50}Te_{0.50}$ (l = 1.2 nm) /ZnSe (h = 0.6 nm)/ZnS (H = 0.6 nm), respectively. We adopt an inverted device structure, in which NC emissive layer (EML) is sandwiched between hybrid charge transport layers.[32,56] In this device structure, the electrons drift from ITO to NCs *via* ZnO electron transport layer (ETL), and holes drift from MoO_X /Al to NCs *via* 2,2’ −bis(4−(carbazol−9−yl)phenyl)−biphenyl (BCBP) hole transport layer (HTL) (figure 4a). A thin layer of poly[(9,9−bis(30−(N,Ndimethylamino)propyl)−2,7−fluorene)−alt−2,7−(9,9−ioctylfluorene)] (PFN) (~ 2 nm) is employed as an interfacial dipole layer to reduce the electron injection barrier between NCs EML and ZnO ETL (ΔE_{CBE} = 1.3) through the vacuum level shift (ΔE = 0.3 eV).57 BCBP with deep highest occupied molecular orbital (−5.7 eV) serves as the hole transport layer (HTL) for efficient hole injections into both blue− and yellow−emitting ZnSe/$ZnSe_{1-X}Te_X$/ZnSe/ZnS SQW NCs.

Fig 2.4 displays the representative characteristics of dichromatic white NC−LEDs employing a mixed layer of blue− and yellow−emitting ZnSe/$ZnSe_{1-X}Te_X$/ZnSe/ZnS SQW NCs.

The mixing ratio for blue− and green−emitting NCs is set to be 1:3 (wt%:wt%) by a process of trial and error. The resulting device displays the peak external quantum efficiency of 1.6 %, the peak luminance over 5,000 cd/m^2, and most importantly, stable white colors upon the variation of operation conditions (**Fig 2.4b−e**). For practicable use in lighting applications, the brightness in range of 1,000 – 5,000 cd/m^2 and the high color stability are required.[58,59] The performance of present NC−LEDs fully satisfies these criteria in view of the brightness (the peak luminance of 5,700 cd/m^2) and the color stability (CIE X = 0.292−0.315 and CIE Y = 0.371−0.41 at the luminance ranges of 700−5,000 cd/m^2).

2.4. Summary

We have demonstrated highly luminescent *quasi*−type II heterostructured nano−emitters formulated in ZnSe/ZnSe$_{1-X}$Te$_X$/ZnSe seed/spherical quantum well/shell heterostructures. In a given formation of NCs, the electron wavefunction is delocalized over the entire volume, whereas the hole wavefunction is strongly confined within the ZnSe$_{1-X}$Te$_X$ emissive layer, and thus the composition of ZnSe$_{1-X}$Te$_X$ emissive layer and the dimension of ZnSe shell layer permit to tailor the hole and electron wavefunction independently. The SQW structural platform alleviates large lattice mismatch between the ZnSe$_{1-X}$Te$_X$ emissive layer and the ZnSe passivation layer. Benefited from the capabilities to tune the charge carriers on demand and to form defect−free heterojunctions, resulting ZnSe/$ZnSe_{1-X}Te_X$/ZnSe/ZnS SQW NCs show near unity photoluminescence quantum yield (PL QY > 90 %) in a range of emission wavelength (peak PL from 450 nm to 600nm), which have not been reached previously. Finally, we exemplify the use of ZnSe/$ZnSe_{1-X}Te_X$/ZnSe/ZnS NCs as the emitters for white light sources.

The supplement of emission wavelengths achieved in the present study completes the emission window for the *quasi*-type II NCs to cover the entire visible region. The apparent next step is to investigate the multicarrier dynamics of ZnSe/$ZnSe_{1-X}Te_X$/ZnSe/ZnS SQW NCs in relationship with their structural formulation. In parallel, the delicate design of heterostructures by means of advances in wet-chemistry is required to engineer the multicarrier dynamics in give NCs. These all together will allow to engineer the interplay of charge carriers of *quasi*-type II NCs on demand and hence foster the use of *quasi*-type II NCs in a range of light-emitting applications including non-blinking quantum emitters, high power LEDs, or low threshold lasers.

Chapter 3.② Impact of morphological inhomogeneity on excitonic states in highly mismatched alloy $ZnSe_{1-X}Te_X$ nanocrystals

3.1. Introduction

Semiconductor alloying is an effective and versatile tool to customize the intrinsic physical properties of materials such as bulk bandgap, effective mass of charge carriers, and lattice parameter on demand. Reducing the dimension of semiconductor alloys to nanoscales permits additional control of the distribution of charge carriers and their dynamics, which enables us to achieve almost arbitrary control of optical and electrical characteristics of materials.[60−63] NCs made of semiconductor alloys, whose physical dimensions allow for the efficient charge carrier recombination and cost−effective solution processing, have gained considerable attention as next generation photon emitters in a wide range of applications, including tunable lasers,[64−66] light emitting diodes[9,10,14,32] and luminescent solar concentrator.[34,35,67]

Heavy metal−free $ZnSe_{1-X}Te_X$ alloy NCs are of particularly interest due to their wide emission tunability from violet to orange and near−unity photoluminescence quantum yields (PL

---

② This chapter is based on paper from Chang, J. H.; Jung, D.; Lee, H. J.; Shin, D.; Kim, Y.; Hahm, D.; Wang, X.; Lee, D. C.; Hwang, E.; Park, Y.−S. Impact of Morphological Inhomogeneity on Excitonic States in Highly Mismatched Alloy ZnSe1–X Te X Nanocrystals. *J. Phys. Chem. Lett.* 2022, *13* (49), 11464−11472.

QYs), with special emphasis on its potential for the blue emitter.[46,68–72] Blue emitters are the essence of everyday light-emitting applications, not only because blue is one of the primary colors but also because it is the energy source for the other color emitters *via* spectral down-conversion. In addition to high efficiency and emission stability that are prerequisites, from a practical standpoint, blue emitters should be given with fine emission wavelength tunability for eye comfort[73] as well as narrow spectral linewidth for wide color gamut.[74,75] Specifically, industrial standards for eye safety suggest limiting the use of high energy blue emission approximately greater than 2.8 eV (440 nm). At the same time, the color range standard by the International Telecommunications Union, referred to as BT.2020,[74,75] drives researchers to push the bandgap envelop of blue emitters to a higher energy region. These restrictions have set stringent conditions for the emission wavelength and linewidth of blue emitters.

However, $ZnSe_{1-X}Te_X$ NCs show broad non-gaussian emission spectra with multiple exponential decay dynamics even with near-unity PL QYs. Interestingly, but unfortunately, all of the previous reports show sudden linewidth broadening as the peak emission wavelength of $ZnSe_{1-X}Te_X$ NCs is tuned to the blue region (*i.e.*, full width at half maximum, FWHM = 35–45 nm (210–270 meV) for NCs with peak PL at 450–470 nm (2.64–2.76 eV)),[46,68–72] which is 2–2.7 times higher compared with that of standard red or green heavy metal free NCs implemented in LED applications (*i.e.*, peak PL/FWHM for red InP NCs = 630 nm/35 nm (1.97 eV/109 meV) and green InP NCs = 530 nm/35 nm (2.34 eV/155 meV)),[29,76,77] imposing a roadblock toward their practical use in display applications. Most importantly, understanding the origin of unusual characteristics of these $ZnSe_{1-X}Te_X$ alloy NCs is lacking and so are the future research directions.

Herein, we investigate the underlying mechanism of spectral linewidth broadening of highly mismatched $ZnSe_{1-X}Te_X$ alloy NCs in the blue region. We first devise heterostructured NCs made of $ZnSe_{1-X}Te_X$ ($0 \leq X \leq 0.33$) and ZnSe in a geometry wherein the impact of size (volume) inhomogeneity to the bandgap dispersion is minimized. We conduct ensemble and single dot spectroscopic analysis to monitor homogeneous and inhomogeneous broadening in a series of $ZnSe_{1-X}Te_X$ NCs. Finally, we perform ab initio DFT calculations and assess the impact of composition homogeneity on the linewidth broadening.

3.2 Experimental Section

Materials. Zinc acetate ($Zn(ac)_2$, 99.99 %), selenium (Se, 99.9 %), sulfur (S_8, 99.9 %), oleic acid (OA, 99 %), n-trioctylphosphine (TOP, 99 %), and 1-octadecene (ODE, 99 %) were purchased from Uniam. Diphenylphosphine (DPP, 98 %), and 1-dodecanethiol (DDT, 98 %) were purchased from Aldrich. Tellurium powder (Te, 99.999 %) was purchased from Alfa Aesar. All chemicals were used as received.

Precursor preparation. A mixture of 10 mmol of $Zn(ac)_2$ and 20 mmol of OA was loaded in a flask, degassed at 110 °C for 3 hour to form $Zn(OA)_2$ complex, and back−filled with N_2. An adequate amount of ODE was added to make 0.5 M $Zn(OA)_2$ precursor. 1 mmol of Se powder, 1 mmol of S powder or 0.25 mmol of Te powder were dissolved in 0.5 ml of TOP to prepare 2 M TOPSe, 2 M TOPS or 0.5 M TOPTe. 4 mmol of Se power, 2 ml of DPP and 18 ml of anhydrous toluene was mixed to prepare 0.2 M DPPSe. DDT was diluted with ODE to make 1 M DDT precursor.

Synthesis of $ZnSe/ZnSe_{1-X}Te_X/ZnSe/ZnS$ NCs. All synthesis were carried out under an inert atmosphere through the Schlenk line technique. 1.2 ml of 0.5 M $Zn(OA)_2$ and 15 ml of ODE were stirred in a 3−neck round flask, degassed under vacuum at 110 °C for an hour and backfilled with N_2. The flask was heated up to 230 °C to proceed the NC growth. 1 ml of 0.2 M DPPSe was swiftly injected into the flask to synthesize ZnSe seed (r = 0.6 nm). After 1 min of reaction, a mixture of 0.88 ml of 0.5 M TOPTe and 2.6 ml of 2 M TOPSe was injected dropwise (0.12 ml/min) to grow a $ZnSe_{1-X}Te_X$ alloy layer. The total amount of TOPTe and TOPSe was fixed, but the amount of each precursor was varied to control the composition of the $ZnSe_{1-X}Te_X$ alloy layer. Since the reactivity of Te precursor exceeds that of Se precursor, the injection of Te and Se precursors all at once could result in the compositionally−graded $ZnSe_{1-X}Te_X$ layer, wherein Te is rich at the inner layer while Se is rich at the outer layer. To obtain homogeneous $ZnSe_{1-X}Te_X$ alloying, we inject the mixed Te:Se precursors dropwise at a certain rate such that throughout the growth process the anion precursor concentration remains depleted, leading to uniform Te:Se ratio in the $ZnSe_{1-X}Te_X$ layer. After 30 min of reaction, the flask was further heated to 320 °C to grow ZnSe and ZnS shell layers. At the elevated temperature, 74 ml of 0.5 M $Zn(OA)_2$ and 18 ml 2M TOPSe were added to grow 1.6 nm thick ZnSe shell growth. After 1 hour of reaction, 180 ml of 0.5M $Zn(OA)_2$ and 48 ml of 1M DDT were injected to grow 1 nm thick ZnS exterior layer. The reaction temperature was maintained for 1 hour and cooled to room temperature to complete the reaction. Produced NCs were purified repeatedly in glove box *via* precipitation (acetone)/redispersion (anhydrous toluene) method, diluted in anhydrous toluene (20 mg/ml) and kept in glove box for characterization.

Characterization. Absorption and photoluminescence spectra were obtained with Shimadzu UV-1800 and Horiba FluoroMax-4, respectively. Absolute PL QY was measured with Otsuka QE-2000 at the same absorbance (0.1) in toluene at the 350 nm excitation wavelength. High-resolution TEM images were obtained from FEI Tecnai-F20. Time-resolved emission spectra measurement was conducted using the 405nm (3.06 eV) excitation beam at 500 kHz repetition rate (PicoQuant, LDH-D-C-405 laser diode) with photo multiplier tube (PicoQuant, PMA-C182-N-M) coupled to the monochromator (Teledyne Princeton Instruments, SpectraPro SP-2150). Single-dot measurements were conducted using Hanbury Brown-Twiss setup with the same excitation beam. We prepared samples for single-dot spectroscopic measurement in a glovebox. NCs diluted with hexane were drop−cast onto a coverslip cleaned with UV−Ozone cleaner. The coverslip was encapsulated to prevent exposures to oxygen and moisture. The laser beam was focused on the sample using the oil immersion objective (Olympus, UPLXAPO100XO, 1.45 NA). The photons were collected through the same objective lens and directed to EMCCD camera (Princeton Instruments, ProEM HS1024BX3) attached to the spectrometer (Princeton Instruments, IsoPlane SCT320) or to single−photon avalanche diodes (Micro Photon Devices, PDM Series) connected with time−correlated single photon counting module (PicoQuant, HydraHarp 400). Hanbury Brown−Twiss setup was used to measure the exciton dynamics, blinking statistics and the second order correlation function $g^{(2)}(t)$ of individual NCs.

Relationship between PL QY of NCs and PL decay lifetime. The PL QY is defined as $PL\,QY = k_{rad}/(k_{rad} + k_{non-rad})$ with the radiative (k_{rad}) and non−radiative ($k_{non-rad}$) recombination rates. We have devised ZnSe/ZnSe$_{1-X}$Te$_X$/ZnSe/ZnS spherical quantum well heterostructured NCs, in which ZnSe$_{1-X}$Te$_X$ is *coherently strained* to fit into the surrounding ZnSe seed and shell layer, so that the formation of internal defects is effectively suppressed. In this geometry, PL QYs of the series of NC samples reach near−unity, indicating that the non−radiative recombination rate is negligibly small ($k_{non-rad} \approx 0$). Thus, the change in PL decay rates does not necessarily alter the PL QY of NC samples.

Calcualtions. We simulated electronic properties of $ZnSe_{1-X}Te_X$ ($0 \leq X < 1$) using the generalized gradient approximation functional of Perdew–Burke–Ernzerhof (PBE) and Ultra soft pseudopotential (USPP) as implemented in the QUANTUM–ESPRESSO DFT code. We constructed a 2x2x2 (62–atom) cubic supercell of zincblende ZnSe and, for Te doping, we replaced Se atoms with Te atoms (*i.e.*, the 6 percent doping of Te corresponds to 32 Zn atoms, 30 Se atoms, and 2 Te atoms in the unit cel). To check the cluster effect of two tellulium atoms we performed the calculation by changing the distance of two Te atoms inside the supercell. After setting the supercell we fully relaxed the cell to optimize the structure. After convergence tests, we adopted 50 Ry of wave function energy cutoff and 300 Ry of charge density cutoff. For a dense K–point grid for fine DOS result, we used 4x4x4 K–point grid for self consistent field calculation (SCF) and increased the K–point into 6x6x6 using non–self consistent calculation (NSCF). For the band structure, we simulated around Gamma point where the bandgap appears. We used fixed occupation to make a small difference in DOS visible.

3.3. Results and Discussion

We adopt ZnSe (radius, $r = 0.6$ nm)/$ZnSe_{1-X}Te_X$ (thickness, $l = 1.2$ nm)/ZnSe (thickness, $h = 1.7$ nm)/ZnS (thickness, $d = 1.0$ nm) seed/spherical quantum well/shell/shell heterostructured NCs[68] as a model system (**Fig. 3.1a**). In this geometry, the sandwiched $ZnSe_{1-X}Te_X$ emissive layer is coherently strained to fit into the surrounding ZnSe layers, alleviating the structural stress (lattice constant of ZnSe, ZnTe is 0.5668, 0.6101 nm) and thus allowing NC heterostructure free from internal defects.[50,68] To protect the NC surface from oxidization during photophysical measurements, NCs are passivated with an exterior ZnS layer. The resulting NCs show near−unity photoluminescence quantum yields (PL QYs) for a range of Te content up to 33%, which validates defect−free, epitaxial growth of each layer throughout the synthesis.

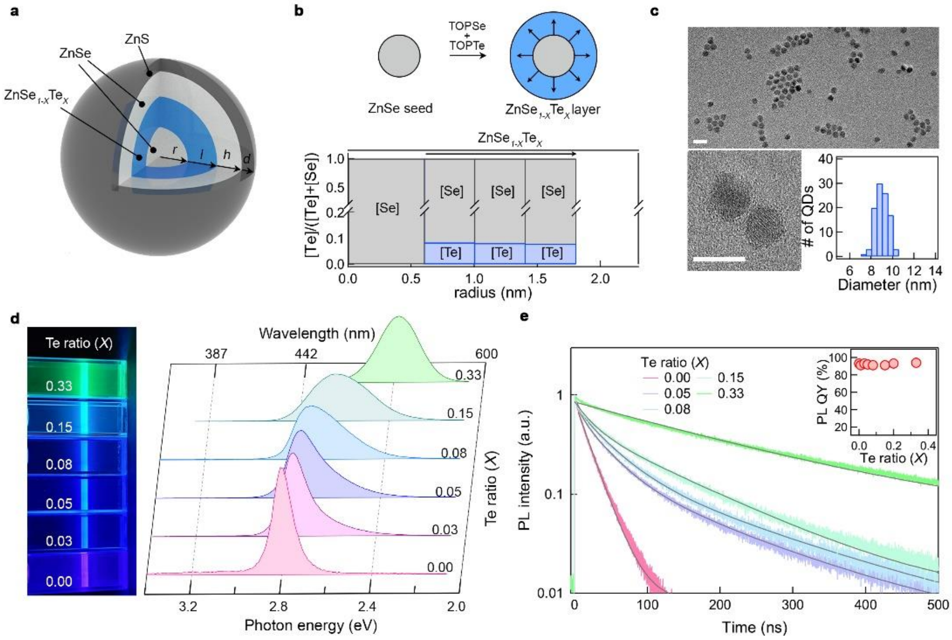

Figure 3. 1. Structural and optical characteristics of $ZnSe/ZnSe_{1-X}Te_X/ZnSe/ZnS$ NCs. (a) A schematic illustration of $ZnSe/ZnSe_{1-X}Te_X/ZnSe/ZnS$ seed/spherical quantum well/shell/shell heterostructured NCs. *r, l, h,* and *d* indicate the radius of ZnSe seed, and thicknesses of $ZnSe_{1-X}Te_X$, ZnSe, and ZnS layers, respectively. (b) A chemical sheme for the growth of the $ZnSe_{1-X}Te_X$ alloy layer (top) and a composition profile of an NC having $ZnSe_{0.92}Te_{0.08}$ emissive layer along the radial direction (bottom). (c) Transmission electron microscopy (TEM) images of $ZnSe/ZnSe_{1-X}Te_X/ZnSe/ZnS$ NCs and their size distribution (bottom right). The scale bars indicate 20 nm and 10 nm for top and bottom TEM images, respectively. (d) A photograph (left) and PL spectra (right), and (e) transient PL decay curves (inset: PL QYs) of $ZnSe/ZnSe_{1-X}Te_X/ZnSe/ZnS$ NCs with varying Te ratios ($0 \leq X \leq 0.33$). Grey lines indicate exponential fits to decay curves (single-exponential fits for

$X = 0 \text{ and } 0.33$ and double−exponential fits for $X = 0.05, 0.08\ and\ 0.15$）.

The reference sample without Te ($X = 0$), *i.e.,* ZnSe (r = 3.5 nm)/ZnS (d = 1.0 nm) NCs, radiates gaussian shape PL spectra positioned at 440 nm (2.80 eV) along with a narrow linewidth of 16 nm (100 meV), which corresponds to the violet emission of bulk ZnSe. To down−shift the PL spectrum to blue, a mixture of Te and Se precursors is injected to grow a $ZnSe_{1-X}Te_X$ layer. The compositional homogeneity of $ZnSe_{1-X}Te_X$ layer along the radial direction is validated by the inductively coupled plasma atomic emission spectroscopy (ICP−AES) coupled with the geometry assessment (**Fig. 3.1b**). It is noted that the well−controlled change of Te contents in $ZnSe_{1-X}Te_X$ layers ($0 \leq X \leq 0.33$) does not affect either the size or shape of NCs, or their homogeneity.

ZnSe/$ZnSe_{1-X}Te_X$/ZnSe/ZnS NCs retain *quasi*−type II band alignment,[68] wherein the hole is confined within the $ZnSe_{1-X}Te_X$ layer, while the electron is deocalized over ZnSe seed, $ZnSe_{1-X}Te_X$ and ZnSe shell layers. In the present geometry, the optical bandgap is affected not only by the dimensions of each layer in NC heterostructure, but also by the chemical composition of the $ZnSe_{1-X}Te_X$ layer, which obscures understanding the origin of emission linewidth broadening. To minimize the impact of size inhomogeneity on the linewidth broadening, we optimize the reaction conditions for each layer growth and obtain narrow NC size dispersion. TEM analysis shows that the size inhomogeneity (σ_{RMS}) from ZnSe seeds to the final heterostructured NCs remains less than 10 % (**Fig. 3.1c**). Moreover, we devise a larger volume ZnSe shell layer (*i.e.*, thickness, h = 1.7 nm), so that the lowest quantized state for electron ($1S_e$) barely alters upon a given size variation of NCs. At the fixed geometry and growth condition, we have varied the Te contents in the $ZnSe_{1-X}Te_X$ emissive layer in a controlled way and conducted spectroscopic analysis on a series of NC samples.

The emission color of $ZnSe/ZnSe_{1-X}Te_X/ZnSe/ZnS$ NCs shifts from violet to blue with increasing Te content ($0 \leq X \leq 0.15$) (**Fig. 3.1d**). Interestingly, we find that the spectral shift results from an emergence of additional peaks at lower energy positions, approximately larger than $110\,meV$ apart from the apex, rather than the gradual shift of the main peak, which is evident in asymmetric PL spectral profiles for NCs with non-zero Te content. In fact, the additional peaks in the lower energy side of PL spectra have been commonly observed in $ZnSe_{1-X}Te_X$ based NCs whose PL peak emission lies in the blue region (450–470 nm (2.64–2.76 eV)).[46,68–72] This phenomenon is responsible for the sudden broadening of spectra linewidth (FWHM) from $110\,meV$ (16 nm) for $X = 0$ to $260\,meV$ (44 nm) for $X = 0.08$.

The emergence of additional emission band in these blue emitting NCs is also monitored in their PL decay curves measured from NC solution with no spectral filters (**Fig. 3.1e**). For NCs with Te ($X = 0$), the decay curve is fitted well with a single exponential decay with a fast rate of $0.05\,ns^{-1}$. However, in sharp contrast, once the Te content is present in NCs, an additional slow decay component ($0.015\,ns^{-1}$ for $X = 0.05$)

appears and this slow decay gets prominent for the further increase of Te contents ($0.010\, ns^{-1}$ for $X = 0.15$). For NCs with $X = 0.33$, there exists a slow decay component ($0.009\, ns^{-1}$) only. Considering near−unity PL QYs for these NCs (inset of **Fig. 3.1e**), multi−exponential decay curves indicate the presence of multiple distinctive radiative recombination channels in NCs. Both fast and slow decay rates show strong dependence on the Te contents, which reflects essential changes in the electron−hole recombination mechanism of these blue−emitting NC, as discussed in detail later.

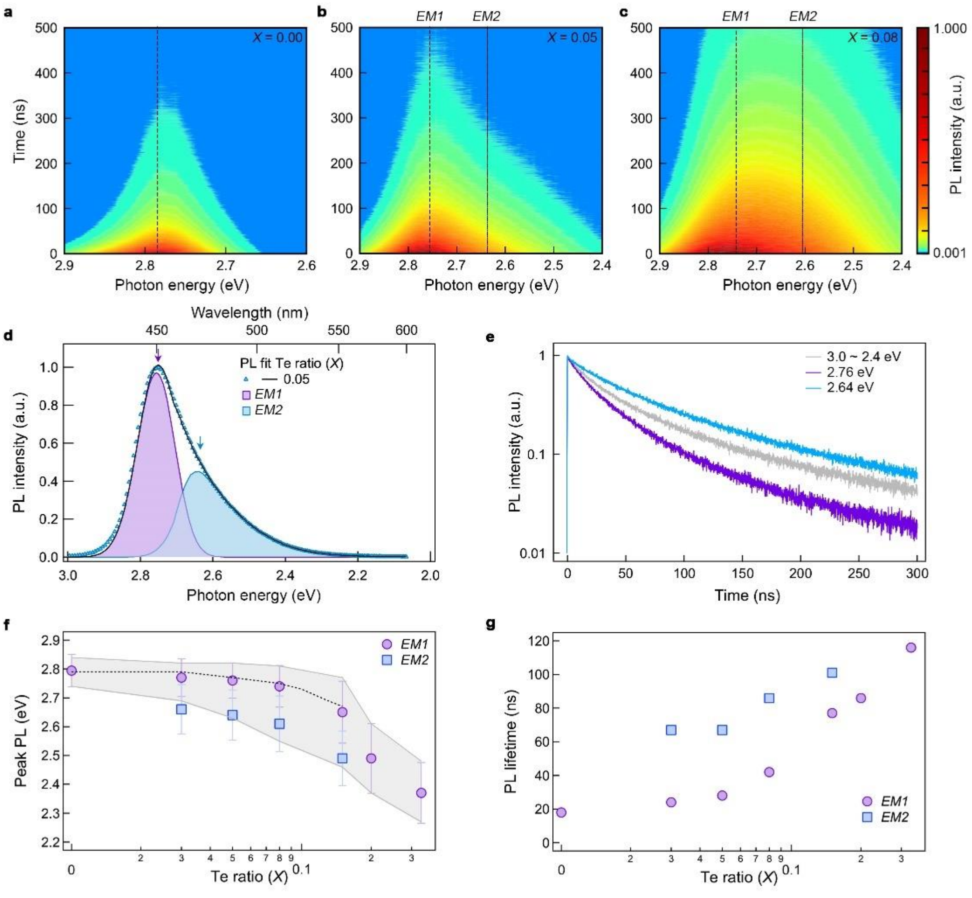

Figure 3. 2. Photophysical characterisctiscs of ZnSe/ZnSe$_{1-X}$Te$_X$/ZnSe/ZnS ensemble NCs. (a−c) Time−resolved PL

spectra of ZnSe/ZnSe$_{1-X}$Te$_X$/ZnSe/ZnS NCs with varying Te ratios (X = 0, 0.05 and 0.08). The dashed guidelines and dotted guidelines indicate the peak PL energies of *EM1* and *EM2* for each NCs. (d) Time-averaged ensemble PL spectrum of ZnSe/ZnSe$_{0.95}$Te$_{0.05}$/ZnSe/ZnS NCs (triangle), its constituent PL spectra (noted as $EM1$ (violet) and $EM2$ (blue)) and their sum (solid black line). (e) PL decay curves measured at the peak energy of the constituent PL spectra (2.76 eV (violet), and 2.64 eV (blue)). The decay curve of the entire PL spectrum is displayed for comparison (grey). (f) The peak energies (error bars: linewidths) and (g) 1/e lifetimes of the constituent PL spectra ($EM1$ (violet circle) and $EM2$ (blue square)) of ZnSe/ZnSe$_{1-X}$Te$_X$/ZnSe/ZnS NCs with varying Te ratios ($\mathbf{0} \leq X \leq \mathbf{0.33}$). The dotted line in Fig. 2f is calculated 1S$_e$-1S$_h$ energy gap for NCs comprising homogeneous ZnSe$_{1-X}$Te$_X$ alloys (without nearest-neighbor Te pairs). The grey background in **Fig. 3.2f** indicates the linewidths of entire PL spectra of each NCs.

For the systematic analysis of the emission properties of blue emitting ZnSe/ZnSe$_{1-X}$Te$_X$/ZnSe/ZnS NCs ($0.03 \leq X \leq 0.15$), we performed spectrally- and temporally-resolved spectroscopic measurements. As displayed in **Fig. 3.2a-c**, for the NCs with $X = 0.05$ and 0.08, we observe substantial spectral shift to a lower energy side as the PL decays away, which distinctly differs from the characteristics of the reference NCs without Te ($X = 0$), where the PL peak energy remains constant over the entire observation time. This observation is consistent with the emergence of additional peak and slow decay component discussed before, again suggesting the presence of distinct emission states in blue emitting NCs when the Te content is present.

Here we decouple the PL spectra of blue-emitting NCs into two constituent PL spectra, namely $EM1$ and $EM2$ (**Fig. 3.2d**); $EM1$ corresponds to the optical transition ($1S_e \rightarrow 1S_h$) between the lowest quantized states of the electron and the hole, and $EM2$ is the emergent PL side peak, respectively. The peak positions of $EM1$ are attained from quantum mechanical calculation that takes account of the quantum confinement effect for homogeneous ZnSe$_{1-X}$Te$_X$ alloying, and the spectrum of $EM1$ is assumed to have a Gaussian shape with an emission linewidth that is inferred from the high energy side profile of PL spectrum. Then, $EM2$ are obtained by subtracting $EM1$ from the entire PL spectra (**Fig. 3.2d**). Specifically, for ZnSe/ZnSe$_{1-X}$Te$_X$/ZnSe/ZnS NCs with 3, 5 and 8 % Te contents, we resolve $EM1$ with Gaussian spectral shape centered at 2.77, 2.76 and

$2.74\ eV$ and $EM2$ having asymmetric profile with extended tails at the low energy regime with the peak positions at 2.66, 2.64 and $2.61\ eV$, respectively. These two emissions clearly differ not only from their energies and shapes, but also from their radiative recombination dynamics. As shown in **Fig. 3.2e**, for NCs with $X = 0.05$, the characteristic time (defined as 1/e lifetime) of $EM2$ is 67 ns, which is approximately 3 times slower than that of $EM1$ (24 ns). The discrepancy in PL energy and decay dynamics between $EM1$ and $EM2$ becomes smaller with increasing the Te content (**Fig. 3.2f** and **g**), and eventually they merge to form single gaussian PL spectra with nearly single exponential PL decay dynamics.

To comprehend the phenomenon at individual NC level, we have conducted single-dot spectroscopic analysis on ZnSe/$ZnSe_{1-X}Te_X$/ZnSe/ZnS NCs with varying Te contents ($0 \leq X \leq 0.33$) over 350 individual NCs (**Fig. 3.3**). The reference samples without Te ($X = 0$, ZnSe/ZnS NCs) or with high Te content ($X = 0.33$), show narrow PL energy dispersion (**Fig. 3.3a** and **b**), allowing us to exclude the possibility of substantial compositional inhomogeneity among individual NCs. However, large PL energy spread materializes among individual NCs for $0.03 \leq X \leq 0.15$ (**Fig. 3.3a** and **b**), which agrees well with corresponding ensemble spectra with linewidth broadening. For example, for individual NCs with $X = 0.08$ (the 2nd panel of **Fig. 3.3a**), we can see that the dot number distribution is contributed mainly from $EM1$ emission band, accompanied by a small number of NCs from $EM2$ emission band.

In **Fig. 3.3b**, we display the relationship between the PL energy and emission linewidth, which clearly demonstrates a strong correlation in single−dot level. For a series of NCs with varying Te ratios, we observe that, as the Te content is increased, the average value (denoted by diamonds) of PL energy is decreased and that of the emission linewidth is increased, which is consistent with ensemble measurement (**Fig. 3.1**). Interestingly, the strong correlation between PL energy and linewidth are present also within individual NCs for a given Te ratio, despite their large spreading of individual NCs in PL energy and FWHM. Inhomogeneous linewidth broadening presented in individual blue−emitting NCs agrees well with the emergent lower−energy PL sub−peaks along with broader linewidths observed from ensemble spectroscopic analysis (**Fig. 3.2f** and **g**). Moreover, we also find that the PL decay lifetime is also strongly correlated with PL energy (thus, PL linewidth), as displayed for three dots (color−coded) with X = 0.08 in **Fig. 3.3c** and **d**. When the linewidth is broader, the corresponding PL decay is slower (inset of **Fig. 3.3d**).

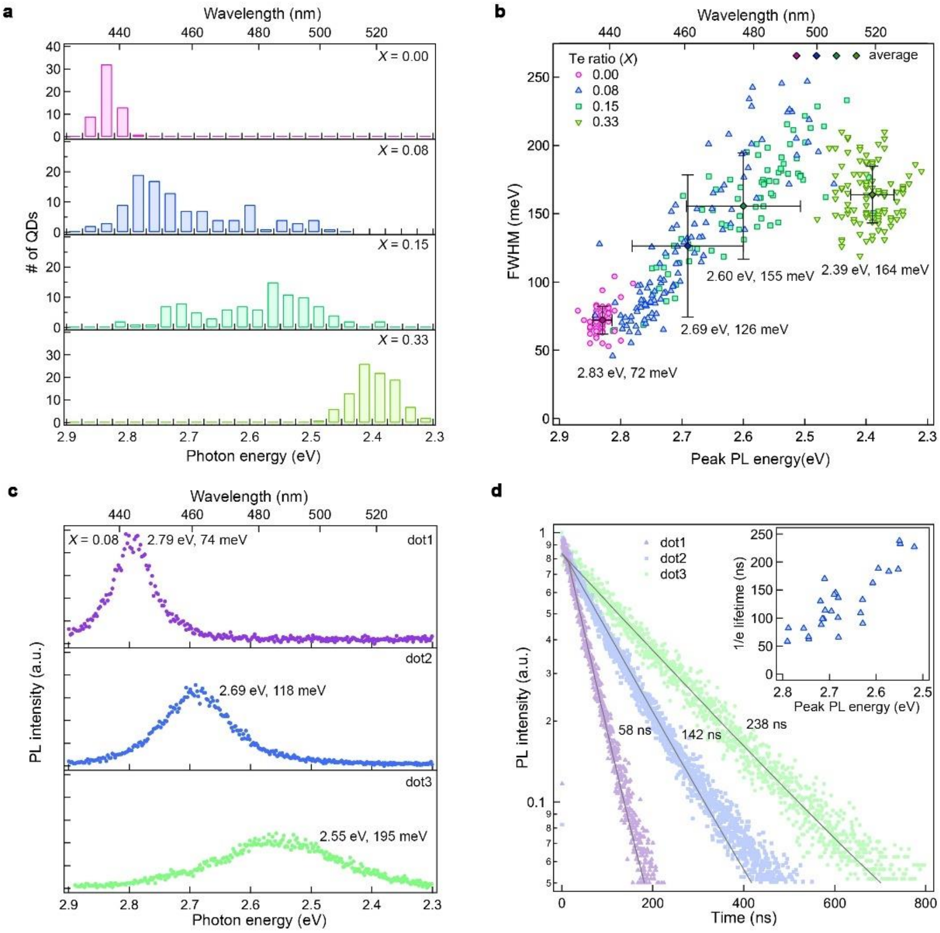

Figure 3. 3. Photophysical characteristics of ZnSe/ZnSe$_{1-X}$Te$_X$/ZnSe/ZnS individual NCs. (a) Histograms of peak PL energies and (b) scatterplots relating FWHM *versus* peak PL energy of individual NCs of ZnSe/ZnSe$_{1-X}$Te$_X$/ZnSe/ZnS NCs with varying Te ratios (0, 0.08, 0.15 and 0.33). The average peak PL energies and their distributions of each composition are noted. (c) PL spectra and (d) PL decay dynamics of individual ZnSe/ZnSe$_{0.92}$Te$_{0.08}$/ZnSe/ZnS NCs having different PL energies. The peak energy and linewidth of PL spectra and 1/e lifetime of PL decay curves of each NC are noted. Grey lines indicate single−exponential fit of corresponding decay. An

inset of **Fig. 3.3d** is the scatterplots relating 1/e lifetime of PL decay curve *versus* the peak PL energy of individual ZnSe/$ZnSe_{0.92}Te_{0.08}$/ZnSe/ZnS NCs.

The delayed radiative recombination and broadened linewidth for lower−energy PL components are typical characteristics of NCs bearing spatially separated electron and hole wavefunctions, for example, heterostructured NCs with *quasi*−type II[43,50,68,78,79] or type II band alignment[80−82], or NCs with emissive trap states.[35,67,83−89] $ZnSe_{1-X}Te_X$/ZnSe heterojunction constructs the *quasi*−type II band alignment, in which a hole is localized in $ZnSe_{1-X}Te_X$ while an electron is delocalized over both $ZnSe_{1-X}Te_X$ and ZnSe phases. In such condition, the increase in the Te content in the $ZnSe_{1-X}Te_X$ alloy layer reduces the energy gap between $1S_e$ and $1S_h$. In addition, the charge disparity due to spatial separation of the electron and the hole induces a strong coupling with the vibration modes in the nanostructure, fostering the PL linewidth broadening of NCs. This explains the PL emission trend observed for $EM1$; slight down−shift of PL peak energy and the elongation of the fast decay component with increasing the Te content. On the other hand, we speculate that $EM2$ should be attributed to the variations in the structure or chemical composition/morphology in our ZnSe/$ZnSe_{1-X}Te_X$/ZnSe/ZnS NCs.

The size inhomogeneity remains constant ($\sigma_{RMS} \simeq 10\,\%$) throughout the NC growth (**Fig. 3.1c**). The quantum mechanical calculation shows that the size inhomogeneity at a fixed chemical composition allows for only $40\,meV$ variation of the energy gap between the lowest quantized state for electron ($1S_e$) and the highest quantized state for hole ($1S_h$), which does not represent the emergence of PL side peaks ($EM2$) at $110-130\,meV$ apart from the apex ($EM1$). This consideration implies that the inhomogeneity in the chemical composition of $ZnSe_{1-X}Te_X$ alloy layer should rationalize the origin for the abrupt linewidth broadening observed in blue-emitting $ZnSe/ZnSe_{1-X}Te_X/ZnSe/ZnS$ NCs.

The PL energy dispersion among $ZnSe_{1-X}Te_X$ based NCs would come from either compositional or morphological inhomogeneity among NCs. The former implies the number variation of Te atoms among NCs, and the latter relates to the spatial distribution of Te atoms in NCs. Considering the reaction of Te and Se precursors occurs in a random manner, one expects Poisson distribution for the Te content in NCs. In case that the $ZnSe_{1-X}Te_X$ alloy layer retains the morphological homogeneity, in other words, Te atoms are well blended with Se atoms such that the presence of nearest-neighbor pairs of Te is excluded, the Poisson distribution for the Te content among NCs allows for at most $40\,meV$ of PL energy dispersion for a series of blue-emitting $ZnSe_{1-X}Te_X$ NCs ($0.03 \leq X \leq 0.08$). However, this does not account for the sudden emergence of PL side peaks ($EM2$) at $110-130\,meV$ lower position from the main PL peak.

Above considerations lead us to deduce that the morphological inhomogeneity of Te atoms in $ZnSe_{1-X}Te_X$ alloy layer is responsible for the distinguished energy dispersion seen in blue-emitting NCs. $ZnSe_{1-X}Te_X$ is a class of highly mismatched alloys, in which metallic anions (electronegativity of Se = 2.4) are replaced by isoelectronic atoms of distinctly different electronegativity (electronegativity of Te = 2.1).[90,91] It is known that the nearest−neighbor pairs of Te create localized hole states (Te_2) residing approximately $30 - 40\,meV$ above E_{VBE} of Se rich $ZnSe_{1-X}Te_X$ alloys (**Fig. 3.4c**).[92,93]

To comprehend the localized hole state induced by the nearest−neighbor pair of two tellurium atoms (Te_2), we investigate the role of Te doping in ZnSe (*i.e.*, $ZnSe_{1-X}Te_X$ with $X < 0.1$). Calculations are performed by using density functional theory and the generalized gradient approximation functional of Perdew, Burke, and Ernzerhof (PBE)[94] as implemented in the QUANTUM−ESPRESSO package.[95] The calculations are performed within a large 64−atom cubic supercell (*i.e.*, 3 percent Te doping indicates the one tellurium substitution out of 32 selenium). Since Te has the same number of valence electrons as the host Se atoms, in most cases, this isovalent doping does not produce a defect level inside the bandgap. The potential difference between the isovalent dopant and the host atom is too small to confine a localized defect level. Thus, when one tellurium atom does not strongly interact with other tellurium atoms nearby, it is expected that no resonant or trapped states are formed inside the bandgap.

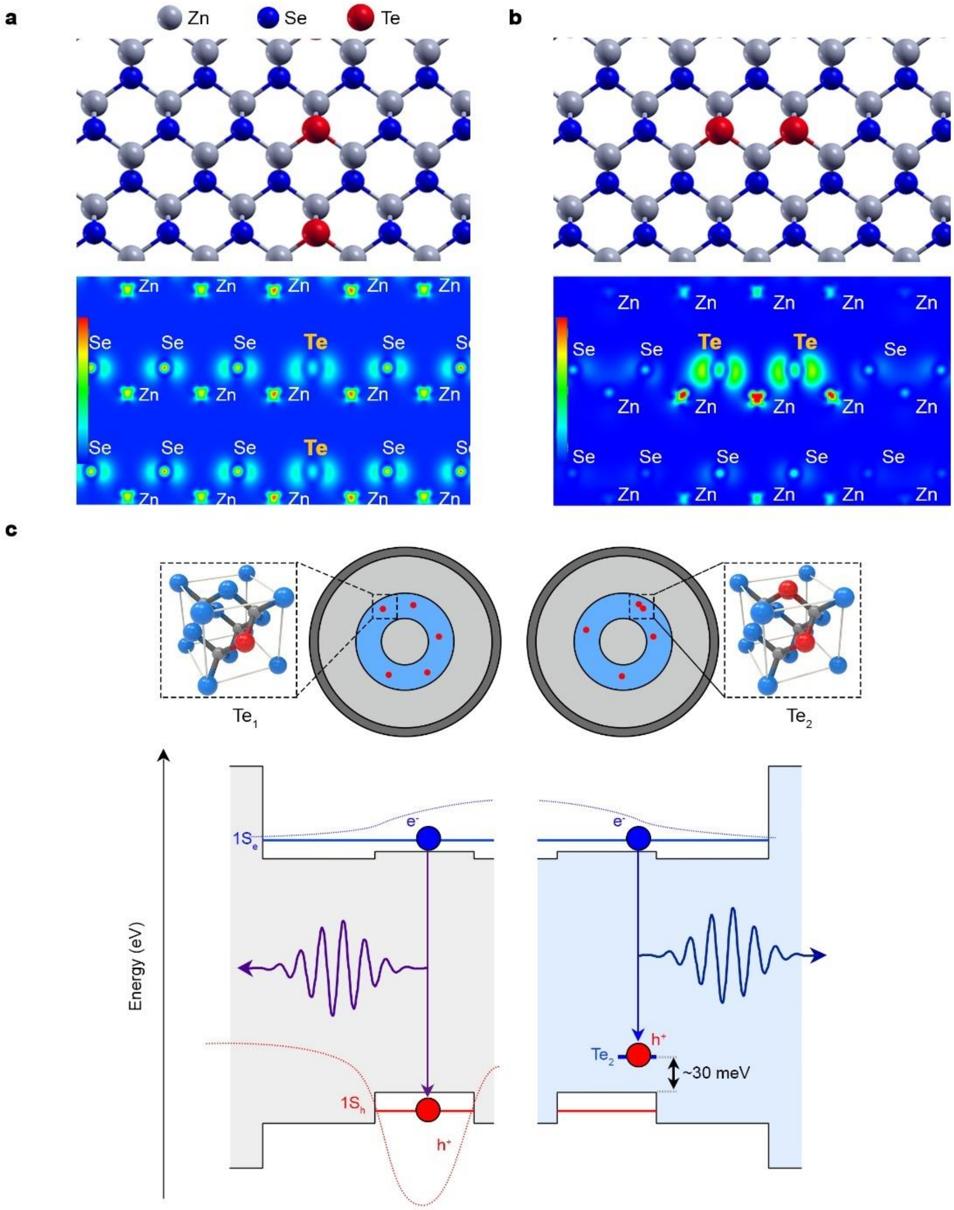

Figure 3. 4. Impact of nearest−neighbor pairs of Te atoms on the optical properties of ZnSe/ZnSe$_{1-X}$Te$_X$/ZnSe/ZnS NCs. (110) planes of bulk zincblende ZnSe$_{1-X}$Te$_X$ structure ($X = 0.06$) (top) and calculated charge density isosurfaces (bottom) of the valence band edge and the Te−induced state above the valence−band edge of ZnSe$_{1-X}$Te$_X$ alloy for (a) without and (b)

with the nearest-neighbor pair of two tellurium atoms (Te_2). Te_2 creates a hole trap state approximately $30 - 40\ meV$ above the valence band edge energy level of bulk zincblende $ZnSe_{1-X}Te_X$ alloys. (c) Band structure and electronic energy levels of $ZnSe/ZnSe_{1-X}Te_X/ZnSe/ZnS$ NCs without (left) *versus* with the nearest-neighbor pair of Te atoms (right).

In **Fig. 3.4a**, we show the charge density isosurface of the VBE when two Te atoms are located far enough and don' t form the nearest-neighbor Te pair. In this case, the charge density of the VBE is almost identical to that of ZnSe. The calculated band structure shows that instead of forming the impurity states the overall bandgap is reduced in this case, *i.e.*, homogenous alloying. In **Fig. 3.4b**, we show the calculations when two tellurium atoms are located in nearest-neighbor sites after Se substitution. In this case, the Te pair can introduce an impurity state above the VBE. The charge density isosurface corresponding to this state shows strongly localized around the Te pair. The isosurface corresponding to the VBE suggests that there is an interaction between this trap state and the extended states of the valence band. The calculated band structure shows that the nearest-neighbor Te pair (Te_2) creates a hole trap state approximately 30 meV above the VBE of bulk $ZnSe_{1-X}Te_X$ alloys (the right panel of **Fig. 3.4c**).

In $ZnSe_{1-X}Te_X$ based NCs, $1S_h$ resides approximately 70-100 meV below of bulk $ZnSe_{1-X}Te_X$ alloy due to the quantum confinement effect, while the localized hole trap state (Te_2) remains unchanged with respect to the bulk band edge (**Fig. 3.4c**). The asymmetric response of Te_2 *versus* $1S_h$ under the quantum confinement effect magnifies the energy difference between the optical transitions of $1S_e$-Te_2 *versus* $1S_e$-$1S_h$. The energy difference is calculated to be $\mathbf{130}\ \boldsymbol{meV}$ in a given geometry of blue-emitting $ZnSe_{1-X}Te_X$ NCs ($\mathbf{0.03 \leq \boldsymbol{X} \leq 0.08}$), which agrees well with the energy difference between the main

PL peak ($EM1$) and the PL side peak ($EM2$). Following the same analogy, we attribute the emergence of higher order PL sub-peaks to the presence of higher number nearest-neighbor Te pairs (*e.g.*, Te_3) in $ZnSe_{1-X}Te_X$ NCs. The coulomb interaction between the hole sitting in the localized trap states and electron prevailing over both ZnSe and $ZnSe_{1-X}Te_X$ phases form the spatially separated exciton, which accounts for the slowdown of radiative recombination rates. NCs bearing nearest-neighbor Te pairs show broader spectra linewidth, which may arise from impurity scattering,[96] surface effect[97] and/or photon scattering.[98] We note that the origin is not clear at this point, and more elaborated experiments, *e.g.*, single dot spectroscopic measurement at low temperature, are needed to elucidate the origin experimentally.

Based on combined spectroscopic analysis and calculations, we explain that, despite the similar Te content, the morphological inhomogeneity of $ZnSe_{1-X}Te_X$ alloys, i.e., with versus without the presence of nearest-neighbor Te pairs, causes substantial difference in photophysical characteristics of NCs in respects to their PL energies, emission linewidth, and decay dynamics. NCs made of homogenous $ZnSe_{1-X}Te_X$ alloys show fast radiative recombination rates with narrow emission linewidths, which are suited for display[14] or lasing applications.[64,65] On the other hand, NCs bearing nearest-neighbor Te pairs (or multiple pairs) accompany large stoke shifts, which is beneficial to reduce efficiency loss, especially in NC films *via* reabsorption, promising their use in luminescent solar concentrators.[34,35,67] From the perspective of end applications, NCs of either type are of profound interest, but the coexistence of both types discourages their practicable use. Although our current synthetic method is carefully designed to yield random deposition of Te and Se atoms to grow $ZnSe_{1-X}Te_X$ alloys, it seems that it is inevitable to create the nearest-neighbor Te pairs even for the low Te contents ($0.03 \leq X \leq 0.08$). Therefore the next challenge facing materials scientists is the development of elaborated chemical schemes enabling the selective growth of $ZnSe_{1-X}Te_X$ NCs in either type only on demand.

3.4. Summary

In summary, we identify the excitonic states in $ZnSe_{1-X}Te_X$ NCs and their photophysical characteristics in relation to the structural feature of highly mismatched alloys. Ensemble and single-dot spectroscopic analysis on a series of NC samples with varying Te contents ($0 < X \leq 0.15$) coupled with computational calculations disclose that the morphological inhomogeneity in the $ZnSe_{1-X}Te_X$ alloy layer, specifically, the presence of nearest-neighbor pairs of Te rather than the size or composition inhomogeneity, is responsible for the dispersion observed in emission spectra and decay dynamics. Due to distinct electronegativity between Se *versus* Te, nearest-neighbor Te pairs in $ZnSe_{1-X}Te_X$ alloys create localized hole states spectrally distributed approximately 130 meV above $1S_h$ level of homogenous $ZnSe_{1-X}Te_X$ NCs. This causes the formation of spatially separated excitons (delocalized electron + localized hole in trap), accounting for both inhomogeneous and homogeneous linewidth broadening with delayed recombination dynamics.

Our results for the first time identify the photophysical characteristics of excitonic states in NCs made of highly mismatched alloys. The phenomena observed in the present $ZnSe_{1-X}Te_X$ NCs will also appear in other highly mismatched alloy systems including $Ga_{1-X}In_XN_{1-Y}As_Y$, $GaN_{1-X}P_X$, or $ZnS_{1-X}Te_X$ alloys. Therefore, results and discussion of the present study will be generally applicable to understand NCs made of this class of materials, and thus provide future research directions with potential implication of their photonic applications.

Chapter 4.③ Direct Assessment of Auger Recombination Rates of Charged Excitons *via* Opto−Electrical Measurements.

4.1. Introduction

Colloidal semiconductor NCs are solution processable nano−emitters that feature narrow spectral linewidth with near−unity quantum yield upon optical or electrical excitation, promising their use in a wide−range of light−emitting applications.[1−6] Representative examples are the down−conversion[7,8] or electroluminescence[9−12] NC displays, in which NCs convert high energy excitation photons or electrically injected charge carriers into narrow band emission of photon energies corresponding to NCs' band gap. After their industrial success in displays, NCs have continued to expand their application territory toward lightings or lasers that demand bright and stable emission from NCs under higher excitation of photon fluxes or charge carrier injection rates.[13−15]

The performance of such applications that demand high emissivity of multicarrier states is dictated by the processes of fast non−radiative Auger recombination (AR), in which the recombination energy of an electron−hole pair is transferred to

---

③ This chapter is based on paper from Lee, H. J.; Rhee, S.; Jung, D.; Park, J. W.; Shin, D.; Lim, J.; Im, S.; Chae, J. A.; Char, K.; Park, K.; Lee, D. C.; Park, Y.−S.; Bae, W. K. Direct Assessment of Auger Recombination Rates of Charged Excitons via Opto−Electrical Measurements. *ACS Photonics* **2023**, *10* (5), 1638−1648.

a third carrier, followed by thermal dissipation.[16] For instance, the imbalance between hole *versus* electron injection rates in NC−LEDs accumulates extra charge carriers, either electrons or holes, in NC emissive films, which leads to the low external quantum efficiency and significant efficiency roll−off at high current density regime due to AR process.[17−20] In addition, fast AR processes complicate both generating multicarrier states for optical gain and maintaining population inversion preventing from reaching the lasing regime.[13,21] Thus, precise assessment of AR characteristics of NCs is prerequisite for their light−emitting applications.

So far, the experimental evaluation of AR rates of charged NCs has relied on photo−charging effects *via* photochemistry, electrochemistry, or stir−*versus*−static measurement, but these approaches are typically limited to probe one kind of polarity, *i.e.*, either negatively or positively charged NCs, and AR rate of other type is inferred from the superposition principle that expresses Auger decay rate of biexciton (XX, two electrons and two holes) as a sum of independent Auger decay pathways of positive trion (X^+, one electron and two holes) and negative trion (X^-, two electrons and one hole), given by ($1/\tau_{A,XX} = 2/\tau_{A,X^+} + 2/\tau_{A,X^-}$), where $\tau_{A,XX}$, τ_{A,X^+}, and τ_{A,X^-} are the Auger lifetimes of XX, X^-, and X^+, respectively.[22,23] For example, $\tau_{A,XX}$ and τ_{A,X^-} of CdSe NCs can be directly evaluated from the decay dynamics under pump fluence dependence and photo−charging effect *via* stir−*versus*−static comparison, respectively, and one can deduce τ_{A,X^+} accordingly to the superposition principle.[24−26] Alternatively, the Auger lifetime of charged excitons, predominantly X^- in nanocrystals, can be obtained using electrochemistry, which involve a redox reaction between an electrode and NCs in solution under an external potential.[27−34] In photochemistry, chemical reducing agent quenches photoexcited holes in the NCs, leaving the unpaired electron that will result in X^- under photoirradiation.[35−42] In contrast to X^-, the generation of X^+ in NCs has been challenging due to the lack of suitable oxidizing agent, thus only a few studies have been reported.[42−44]

Despite the apparent successes, above methods still face following limitations. The stir−*versus*−static measurement permits to probe only one type of charged excitons of NCs due to incontrollable surface trap states.[24−26] The electrochemistry is allowed only for the case that the lowest quantized energy states for hole ($1S_h$) and electron ($1S_e$) of NCs position near the potential of the working electrode[30], otherwise unwanted side reactions could occur when high voltage is applied to inject charge carriers into NCs.[31,45] The photochemistry is applicable to limited NC samples, whose surfaces are robust against side reactions (*e.g.*, oxidation or detachment of ligands) when exposed to oxidizing/reducing agents.[35,39]

Herein, we demonstrate a non−destructive opto−electrical method that permits direct evaluation of AR characteristics of positively and negatively charged excitons of NCs. Specifically, the capability of parity−selective electrical charging of NCs in chorus with optical excitation enables us to directly probe AR decays of X^+ and X^- in a wide range of NC types (type I and *quasi*-type II). We check the validity of measured AR characteristics with previous NC charging methods and finally discuss the validity of superposition principle among multicarrier states in NCs.

4.2. Experimental Section.

Materials for NC synthesis. Cadmium oxide (CdO, 99.95%), selenium powder (Se, 100 mesh, 99.99%) and tellurium powder (Te, 99.999 %) were purchased from Alfa Aesar. 1-dodecanethiol (DDT, 98%) was purchased from Sigma Aldrich. Zinc acetate ($Zn(ac)_2$, 99.9 %), sulfur powder (S_8, 99.9 %), oleic acid (OA, 99 %), 1-octadecene (ODE, 99 %), tri-n-octylamine (TOA, 99%), diphenylphosphine (DPP, 99 %) and tri-n-octylphosphine (TOP, 99 %) were purchased from Uniam.

Materials for device fabrication. Molybdenum oxide (MoO_x, 100 mesh powder, 99.995 %), Lithium fluoride (LiF, 99.9 %) and aluminum (5 mmDia × 5 mmTh pellets, Al, 99.999 %) metal source were purchased from Taewon Scientific Co. (TASCO). PEDOT:PSS (AI 4083), TFB, CBP (99.9%) and TPBi (>98.0 %) were purchased from Heraeus, American Dye Source, OSM and Tokyo chemical industry, respectively.

Precursor Preparation. All chemistry was conducted with Schlenk line technique. 0.5 M cadmium oleate ($Cd(OA)_2$) and zinc oleate ($Zn(OA)_2$) stock solution in ODE were prepared for cation precursors, and 2 M TOPSe, 0.2 M DPPSe, 0.5 M TOPTe, 2 M TOPS, 0.5 M DDT were prepared for anion precursors. For 0.5 M $Cd(OA)_2$ preparation, 50 mmol of CdO and 100 mmol of OA were mixed in the three neck-flask and degassed at 110 ° C for 1 hour, back-filled with N_2 and heated to 280 ° C for 2 hours. The mixture was cooled down to 110 ° C, degassed for 3 hours, and diluted to 0.5 M with ODE. For 0.5 M $Zn(OA)_2$, 50 mmol of $Zn(ac)_2$ and 100 mmol of OA were mixed, degassed at 160 ° C for 4 hours, back-filled with N_2 and diluted to 0.5 M with ODE. For 2 M TOPSe, 100 mmol of TOP and 200 mmol of Se powder were mixed and stirred at 160 ° C for 6 hours. 2 M TOPS and 0.5 M TOPTe were prepared in the same way with TOPSe but different temperatures (60 ° C and 150 ° C, respectively) and concentrations. 0.2 M DPPSe was prepared by mixing 10 mmol of Se powder and 5 ml of DPP at 150 ° C. Subsequently, 45 ml of anhydrous toluene was added for facile use of DPPSe at room temperature. 0.5 M DDT was prepared by diluting DDT with corresponding volume of TOA.

CdSe (r = 1.7, 2.0 nm) core synthesis. CdSe cores were synthesized following the previously reported method[59] with minor modifications. 1 ml of 0.5 M $Cd(OA)_2$, 0.25 mmol of Se powder and 5 ml of ODE were degassed at room temperature (RT) for 5 min in a 3-neck round flask and backfilled with N_2. The solution was heated to 240 ° C and maintained for 10 min (30 min), resulting in CdSe NCs with radius of 1.7 nm (2 nm). CdSe cores were purified twice by precipitation (ethanol)/redispersion (toluene) method and finally redispersed in 5 ml of toluene for further reaction.

***quasi*–Type Ⅱ CdSe (r = 1.7 nm)/CdS (l = 3.7 or 5.7 nm) NC synthesis.** *quasi*–Type Ⅱ CdSe/CdS NCs were synthesized following the previously reported method[26] with minor modifications. Reaction flask containing 10 ml of TOA and 300 mg of CdSe cores (r = 1.7 nm) was degassed at 130 ° C for 30 min, backfilled with N_2 and heated up to 300 ° C for further CdS shell growth. 10 (17) ml of 0.5 M $Cd(OA)_2$ and 0.5 M DDT are injected with a rate of 2 ml/h to the reaction flask for 3.7 (5.7) nm of CdS shell respectively. The reaction was maintained at 300 ° C during CdS shell growth. Resulting NCs were purified fifth in the same way as CdSe core synthesis for further characterizations.

Type Ⅰ CdSe/CdZnS (CdSe (r = 2.0 nm)/$Cd_{0.5}Zn_{0.5}S$ (l = 3.2 nm)) NC synthesis. Type Ⅰ CdSe/CdZnS NCs were synthesized following the previously reported method[46] with minor modifications. Reaction flask containing 10 ml of TOA and 300 mg of CdSe cores (r = 2 nm) was degassed at 130 ° C for 30 min, backfilled with N_2 and heated up to 300 ° C. 7.5 ml of 0.5 M $Cd(OA)_2$, 15 ml of 0.5 M $Zn(OA)_2$ and 5 ml of 2 M TOPS were injected for 30 min to the reaction flask for 3.2 nm of $Cd_{0.5}Zn_{0.5}S$ shell growth. Resulting CdSe/CdZnS NCs were purified fifth for further characterizations.

***quasi*–type Ⅱ ZnSeTe/ZnSe/ZnS NC synthesis. ($ZnSe_{0.67}Te_{0.33}$ (r = 2.5 nm)/ZnSe (l = 1.2 nm)/ZnS (h = 0.6 nm)).** ZnSeTe/ZnSe/ZnS NCs were synthesized following the previously reported method[47] with minor modifications.

Reaction flask containing 1.2 ml of 0.5 M $Zn(OA)_2$ and 15 ml of ODE was degassed at 110 °C for 1 hour, backfilled with N_2 and heated up to 230 ° C. Then, 1 ml of 0.2 M DPPSe and 0.2 ml of 0.5 M TOPTe were injected at 230 °C and maintained for 30 min to synthesize $ZnSe_{0.67}Te_{0.33}$ cores (r = 1.8 nm). After that, 1.4 ml of 0.5 M $Zn(OA)_2$, 1.1 ml of 0.2 M DPPSe and 0.22 ml 0.5 M TOPTe were injected and heated to 300 ° C for 60 min to grow $ZnSe_{0.67}Te_{0.33}$ cores largely (r = 2.5 nm). For further shell growth on the core, 3.4 ml of 0.5 M $Zn(OA)_2$ and 0.425 ml of 2 M TOPSe and 5.0 ml of 0.5 M $Zn(OA)_2$ and 0.625 ml of 2 M TOPSe were injected in order and maintained at 320 °C for 60 min. Additional injection of 7.2 ml of 0.5 M $Zn(OA)_2$ and 0.47 ml of DDT resulted in 0.6 nm thick ZnS shell growth.

Stir-*versus*-static measurement. Prepared NCs (see **EXPERIMENTAL METHODS**) were diluted to 3 mg/ml by anhydrous toluene in the N_2-filled glovebox. It is well-known that vigorous stirring of NC samples prevents NC charging under continued photoirradiation.[24,25] Thus, pump fluence dependent PL decay measurements under vigorous stirring or static conditions enables generating XX or charged excitons (X^+ or X^-) in the NCs.

Photochemistry. NC samples were prepared equally with the stir *versus* static measurement. 200 ul of 0.001 M lithium triethylborohydride (diluted by anhydrous toluene) was added to 3 ml of NC samples. Before optical and photophysical characterization, samples were irradiated under 365 nm UV lamp to achieve photo-charging.

Device fabrications. For EOD fabrication (ITO/ZnO/NCs/TPBi/LiF/Al), 20 mg/ml of ZnO nanoparticles were spun−cast on the ITO substrate at 2000 rpm for 30 sec and annealed at 75 ° C on the hotplate for 30 min in the glovebox. 15 mg/ml of NCs were spun−cast at 4000 rpm for 30 sec on ZnO/ITO and annealed at 80 ° C for 30 min in the glovebox. TPBi (30 nm), LiF (10 nm) and Al (110 nm) were thermally deposited on the NCs/ZnO/ITO films under the pressure of ~ 10^{-6} torr at deposition rate of 1.0−1.5, 0.1−0.2 and 1.0−2.0 Å/s, respectively. For HOD fabrication (ITO/PEDOT:PSS/TFB/NCs/CBP/MoOx/Al), PEDOT:PSS was spun−cast on the UV−exposed ITO substrate at 5000 rpm for 60 sec and baked at 150 ° C for 30 min in an ambient condition. The ITO/PEDOT:PSS films were transferred into a glovebox for further fabrication. 7 mg/ml of TFB was spun−cast on PEDOT:PSS/ITO films at 3000 rpm for 30 sec and annealed at 200 ° C for 30 min. Subsequently, 15 mg/ml of NCs were spun−cast on TFB/PEDOT:PSS/ITO films at 4000 rpm for 30 sec and annealed at 80 ° C for 30 min. CBP (60 nm), MoO_x (10 nm), and Al (110 nm) were thermally evaporated on the NCs/TFB/PEDOT:PSS/ITO films under the pressure of 10^{-6} torr at the deposition rate of 1.0−1.5, 0.1−0.2 and 1.0−2.0 Å/s respectively.

Characterization. UV−Vis, PL spectrum and PL QY were measured with UV−1800 (Shimadzu), FluoroMax−4 (Horiba), and quantauros−QY plus (hamamatsu photonics), respectively. HR−TEM images were obtained with Talos F200i working at

200 kV.Time-correlated single-photon counting (TCSPC) measurement was conducted using the 405 nm (3.06 eV) excitation beam at 500 kHz repetition rate (PicoQuant, LDH-D-C-405 laser diode) with single-photon avalanche diodes (Micro Photon Devices, PDM Series) connected with time-correlated single photon counting module (PicoQuant, HydraHarp 400), and PL spectrum measurement was also conducted using same laser with EMCCD camera (Princeton Instruments, ProEM HS1024BX3) attached to the spectrometer (Princeton Instruments, IsoPlane SCT320).

4.3. RESULTS AND DISCUSSION.

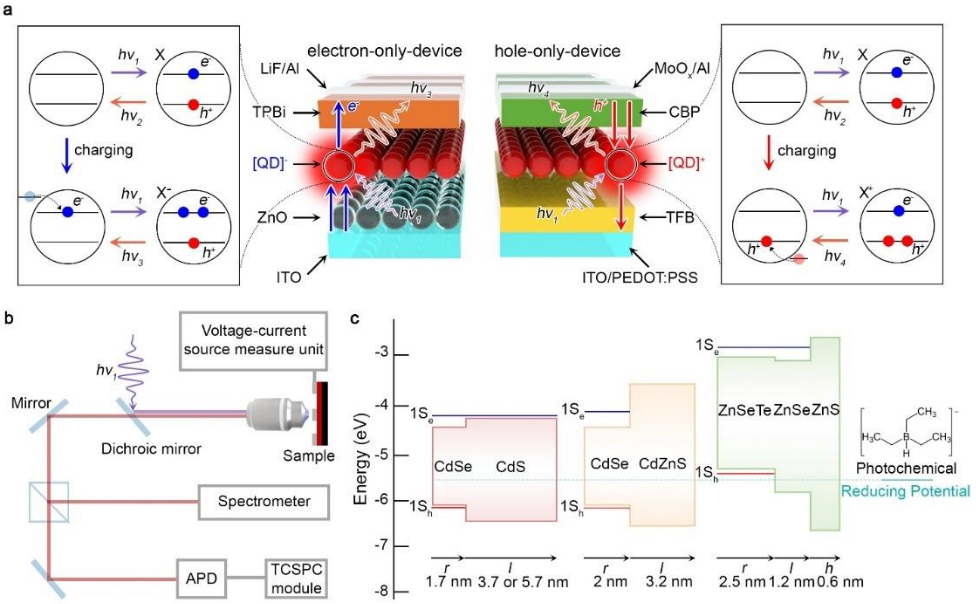

Figure 4. 1. Schemes for direct measurement of Auger recombination characteristics of charged NCs. (a) Schematic illustrations of electron–only–device (EOD, left) and hole–only–device (HOD, right) coupled with a spectroscopic measurement set–up, and the charge states of NCs in each device under photoexcitation. The current flow across the device yields the accumulation of extra charges in NCs. (b) Schematic illustration of spectroscopic set–up with the electrical source measure unit. APD : avalanche photodiode, TCSPC : time–correlated single photon counting. (c) Right–half potential profiles of NCs used in the present study: CdSe (*r* = 1.7 nm)/CdS (*l* = 3.7 or 5.7 nm), CdSe (*r* = 2.0 nm)/CdZnS (*l* = 3.2 nm), and ZnSeTe (*r* = 2.5 nm)/ZnSe (*l* = 1.2 nm)/ZnS (*h* = 0.6 nm). The blue and red solid lines of each NCs show the lowest quantized energy levels of electron ($1S_e$) and hole ($1S_h$), respectively. The cyan solid line indicates reducing

potential of the hole scavenger (triethylborohydride ions).

We devise an opto−electrical setup, in which 1−2 monolayers of NC films are embedded in electrical device and are probed with laser pulses using time−correlated single photon counting (TCSPC) measurement and a spectrometer (**Fig. 4.1**). Electrical devices, *i.e.,* electron−only−devices (EODs) and hole−only−devices (HODs) are made of multilayered films of transparent electrode/charge transport layer/NC films/charge transport layer/electrode (**Fig. 4.1a**). Sputtered ITO on a glass substrate is deployed as the transparent electrode that passes the laser beam and photoluminescence (PL) of NCs, and Al is deposited as the counter electrode. ZnO and 2,2’,2’’−(1,3,5−Benzinetriyl)−tris(1−phenyl−1−H−benzimidazole) (TPBi) are used for the electron transport layers in EODs (left panel of **Fig. 4.1a**), and poly[(9,9−dioctylfluorenyl−2,7−diyl)−*co*−(4,4’−(*N*−(4−sec−butylphenyl)diphenylamine))] (TFB) and 4,4’−Bis(N−carbazolyl)−1,1’−biphenyl (CBP) are adopted for the hole transport layers in HODs (right panel of **Fig. 4.1a**). Additionally, poly(3,4−ethylenedioxythiophene):poly(styrenesulfonate) (PEDOT:PSS) and MoO_x are inserted between electrodes and charge transport layer to facilitate the hole injection, and LiF is adopted to aid the electron injection. Electrical devices are encapsulated by glass cans under an inert atmosphere to prevent the exposure of devices to air and/or moisture.

Spectroscopic setup combined with an electrical source measure unit permits to monitor photophysical and optical properties of NC films in the devices while/after applying electric field across devices (**Fig. 4.1b**). Upon external bias, charge carriers are injected from an electrode and transport across charge transport layers and NCs toward a counter electrode. Due to the quantum well like energy potential of NC–ligands, charge carriers injected into NCs remain for an extended period, long enough to accumulate charges within the NC films under operation. We compare PL decay dynamics of NC films before *versus* after electrical charging to extract fast decay components that are X^- for NCs in EODs and X^+ for NCs in HODs. It is noted that device operation is halted (V_{app} = 0 V) during all spectroscopic measurements to avoid the influence of external electric field on photophysical (*e.g.,* AR rates and exciton recombination rates) or optical properties (*e.g.,* PL intensity and spectra). In both EODs and HODs, we use a weak laser excitation (the average per–pulse exciton number << 0.01) to minimize photo–charging induced by the laser pulses.

We study three types of core/shell heterostructured NCs bearing different potential profiles, *i.e.*, type I CdSe/CdZnS NCs, *quasi*–type II CdSe/CdS NCs, and ZnSeTe/ZnSe/ZnS NCs (**Fig. 4.1c**).[26,46,47] It is known that the hole trapping to the NC surface readily occurs under photoirradiation for type I CdSe/CdZnS NCs and *quasi*–type II CdSe/CdS NCs, enabling one to probe AR rates of X^- from the stir–*versus*–static measurement. Alternatively, photoexcited hole can be eradicated with an addition of hole scavengers (*e.g.*, triethylborohydride ions), allowing to evaluate AR rates of X^- of these CdSe based NCs. By contrast, *quasi*–type II

ZnSeTe/ZnSe/ZnS NCs behave oppositely. These NCs tend to lose electrons to the surface trap sites, allowing to experimentally gain AR rate of X^+ from the stir−*versus*−static measurement. In addition, the same photochemical (*i.e.*, triethylborohydride ions) is not applicable to ZnSeTe/ZnSe/ZnS NCs, whose $1S_h$ state lies above the electrochemical potential of the hole scavengers (**Fig. 4.1c**). Regardless of the potential profiles or energy positions, all NCs are passivated by 1 nm−thick organic ligands that aid NCs to retain injected charge carriers.

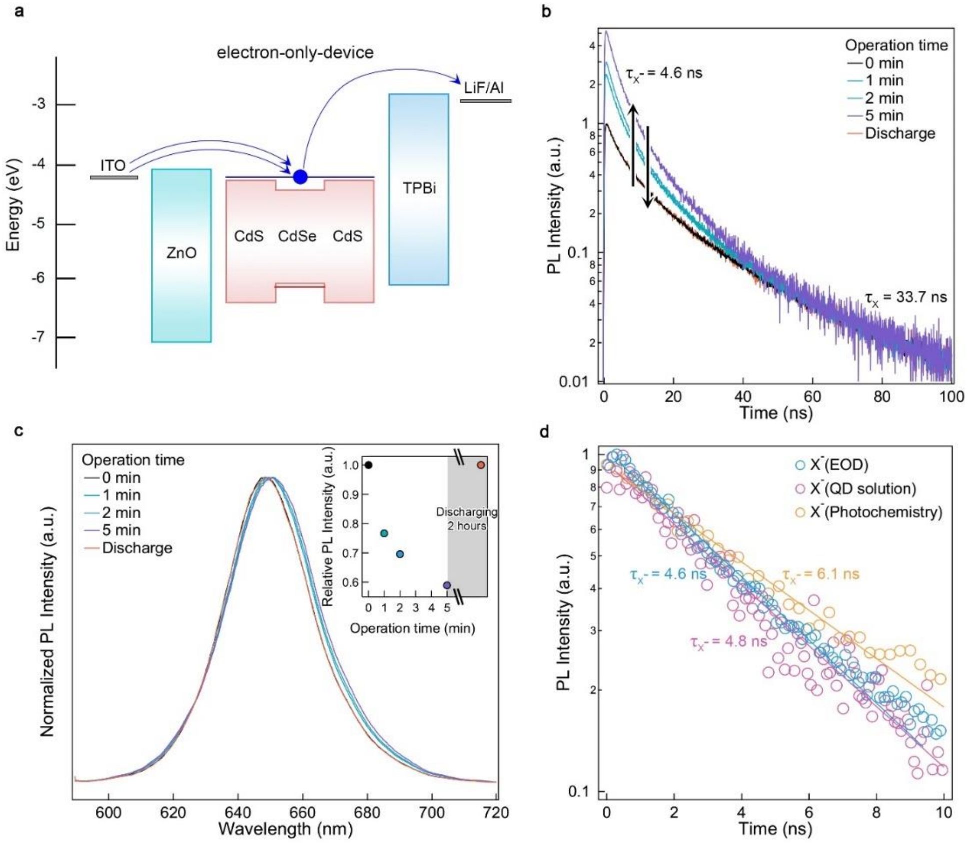

Figure 4. 2. Measurement of negative trion (X^-) decay dynamics of NCs in EOD. (a) Energy band diagram of EOD. Operation time dependent (b) tail-normalized PL decay dynamics and (c) normalized PL spectra of CdSe (r = 1.7 nm)/CdS (l = 5.7 nm) NC films in EOD under a constant voltage ($V_{app} = 1$ V, $0 \le t \le 5$ min). Zero-min means before operation. The inset of (c) shows relative PL intensities of NC films at each step. PL characteristics of NC films return to the initial values under unbiased condition ($V_{app} = 0$ V) after 2 hr. (d) X^- decay dynamics of CdSe (r = 1.7 nm)/CdS (l = 5.7 nm) NCs obtained from various charging methods attained from EOD, stir-*vs*-static (NC solution), and photochemistry. The decay

dynamics are extracted by subtraction of tail–normalized PL decay dynamics of NC samples before *versus* after charging.

Among NC samples, CdSe (radius, *r* = 1.7 nm)/CdS (thickness, *l* = 5.7 nm) NCs, whose multicarrier decay dynamics have been extensively investigated[26,48−52], are selected as the reference for the validity check of our present method in comparison with previous approaches (**Fig. 4.2** and **4.3**). As seen in the flat band structure of EODs (**Fig. 4.2a**), the electrons transport spontaneously from ITO/ZnO into CdSe/CdS NC films and drift toward TPBi/Al in aid of external field due to relatively large energy offset between $1S_e$ of NCs and TPBi (> 1.4 eV for the case of CdSe/CdS NCs). The asymmetry in the energy offset results in the electron accumulation in the NC films. It is noted that the single exciton lifetimes of these thick−shell NCs do not vary upon film deposition. Energy transfer among NCs prevails in NC films, but its characteristic lifetime (*ca.* 20 ns) does not complicate the assessment of AR rates of charged excitons of NCs with characteristic lifetimes of 2−5 ns.

The negative charging of NCs gives rise to temporal changes in both electric characteristics of devices and optical characteristic of NC films. First, the current density of EOD is decreased to 45 % of its initial value under the constant voltage operation (V_{app} = 1 V), indicating that the accumulated electrons impede additional injection of electrons into NCs. Simultaneously, the presence of extra electrons in NC films brings about fast decay components over 5−min operation under a constant voltage of 1 V (**Fig. 4.2b**), accompanied by the decrease in PL intensity down to 58.9 % in 5 mins from its initial value along with the spectral shift to lower energy (**Fig. 4.2c**).[53,54] The extend of changes made in relative PL QYs agrees well with the degree of negative NC charging extracted from PL decay curves[42,54]. These observations altogether indicate that the electrons are accumulated within NCs to promote non-radiative AR process of negatively charged excitons (X^-) upon photoexcitation.

We extract the fast decay component by the subtraction of tail-normalized PL decay dynamics of NC films before *versus* after EOD operation: τ_{X^-} = 4.6 ns, blue solid line in **Fig. 4.2d**. This agrees well with X^- decay dynamics obtained independently from stir-*versus*-static measurement (τ_{X^-} = 4.8 ns, pink solid line in **Fig. 4.2d**) and photochemistry (τ_{X^-} = 6.1 ns, yellow solid line in **Fig. 4.2d**), supporting the validity of the present method. The discrepancy with the lifetime of X^- obtained from photochemistry is speculated to arise from the attachment of reducing agents to the NC surface, which creates an electric field that prolongs the exciton recombination lifetime.[38,39] We observe that PL emission characteristics of NC films fully recover to the initial states after sufficient cooling (after 2 hrs under unbiased condition, V_{app} = 0 V) (right inset of **Fig. 4.2c**), implying that the NC charging method in EOD does not entail unwanted deterioration of NCs.

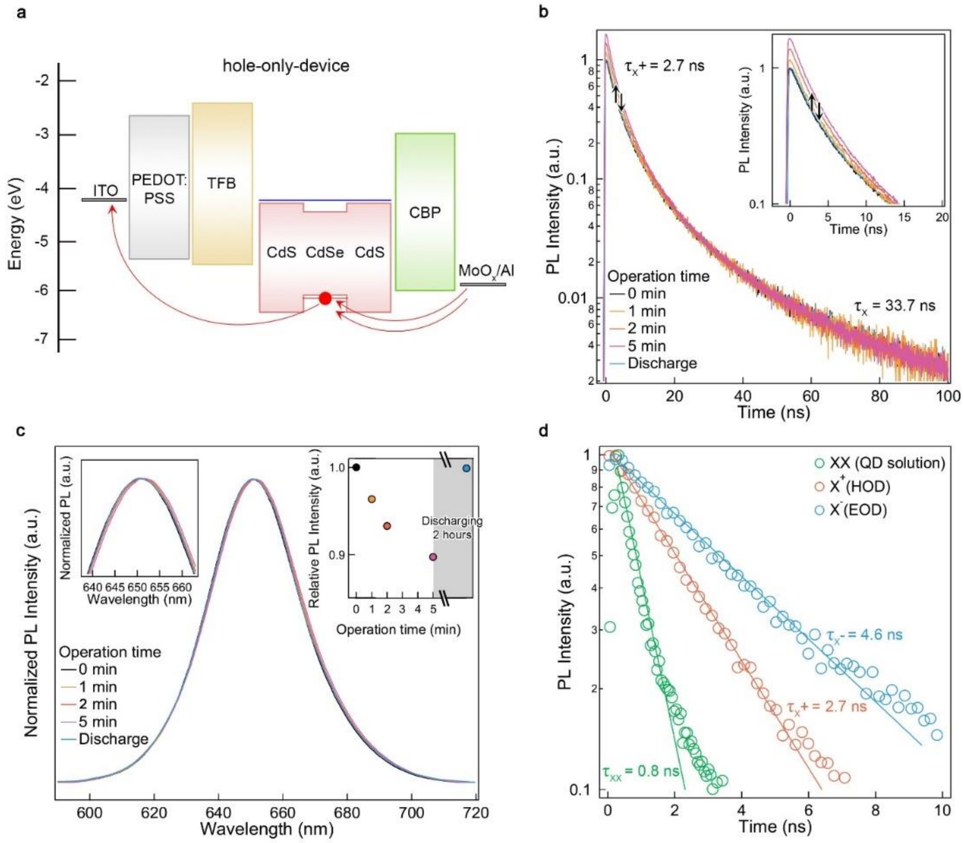

Figure 4. 3. Measurement of positive trion (X^+) decay dynamics of NCs in HOD. (a) Energy band diagram of HOD. Operation time dependent (b) tail-normalized PL decay dynamics and (c) normalized PL spectra of CdSe (r = 1.7 nm)/CdS (l = 5.7 nm) NC films in HOD under a constant voltage (*Vapp* = 2 V, 0 < t < 5 min). Zero-min means before operation. The inset of (b) is the magnified view of PL decay dynamics at the early time. The insets of (c) are the magnified view of PL spectra near PL peak (left) and relative PL intensities of NC films at each step (right). PL characteristics of NC films return to the initial values under unbiased condition (*Vapp* = 0 V) after 2 hr. (d) Multicarrier decay dynamics (XX, X^+ and X^-) of CdSe

(r = 1.7 nm)/CdS (l = 5.7 nm) NCs. Biexciton decay dynamics are obtained from pump fluence dependent measurement of NC solution samples under vigorous stirring. τ values show decay lifetimes of each curve.

Next, we demonstrate direct evaluation on AR rates of X^+ of CdSe/CdS NCs (**Fig. 4.3**). In a HOD, the energy level of $1S_h$ of CdSe/CdS NCs resides deeper than highest occupied molecular orbitals (HOMOs) of neighboring hole transport layers (TFB or CBP) (**Fig. 4.3a**) and consequently hole accumulation in NCs is less effective compared to the electron charging in EOD, showing 10 % reduction of current density even under a higher applied bias (V_{app} = 2 V). Nevertheless, CdSe/CdS NCs retain the injected holes even for a longer period than the case with the electrons owing to the strong confinement by the CdS shell (E_{offset} = 400 meV). Experimentally, 12 % of neutral NCs are positively charged over 5-min operation, accompanied by the rise of fast decay component, whose lifetime is much faster than that of EOD, and spectral shift to lower energy than that of X (**Fig. 4.3b** and **Fig. 4.3c**). We extract the decay dynamics of X^+ (τ_{X^+} = 2.7 ns) by the subtraction of tail-normalized PL decay dynamics of NC films before *versus* after HOD operation (**Fig. 4.3d**). We recite that the PL characteristics of NC films recover to the initial states after sufficient cooling (2 hrs under unbiased condition, V_{app} = 0 V), suggesting that the present method is non-destructive to NCs and the apparent photophysical changes are attributed to the NC charging.

Now, we examine the validity of the superposition principle of biexciton Auger lifetimes based on the lifetimes of charged excitons directly obtained using EOD and HOD. Auger lifetimes of X^+ and X^- are τ_{A,X^+} = 3.2 ns and τ_{A,X^-} = 6.3 ns, respectively, inferred from using a relationship of $1/\tau_{X^{+(-)}} = 1/\tau_{A,X^{+(-)}} + 1/\tau_{r,X^{+(-)}}$ assuming that the radiative decay lifetimes ($\tau_{r,X^{+(-)}}$) of charged excitons are two times shorter than that of single exciton ($\tau_{r,X}$) and AR is the dominant non−radiative process. As a result, the superposition principle yields biexciton Auger lifetime of $\tau_{A,XX} = 1.0$ ns, which agrees well with that ($\tau_{A,XX} = 0.9$ ns, cyan circles in **Fig. 4.3d**) extracted from the pump fluence dependent measurements under vigorous stirring. This result strongly suggests that the superposition principle can play an important role as an auxiliary tool to access AR rates of multicarrier states in NCs when a direct measure is not available.

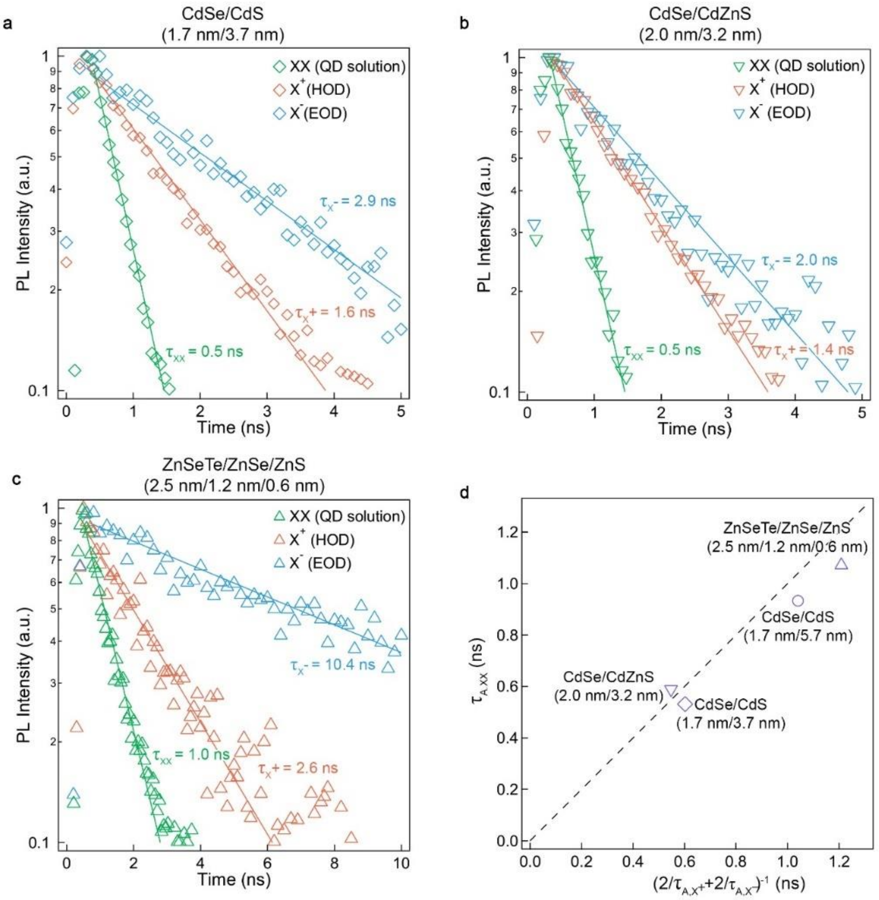

Figure 4. 4. Directly measured multicarrier decay dynamics in various NCs. Multicarrier decay dynamics (XX, X^+ and X^-) of (a) CdSe (r = 1.7 nm)/CdS (l = 3.7 nm), (b) CdSe (r = 2.0 nm)/CdZnS (l = 3.2 nm), and (c) ZnSeTe (r = 2.5 nm)/ZnSe (l = 1.2 nm)/ZnS (h = 0.6 nm) NCs. The τ values indicate decay lifetimes of each curve. (d) Comparison of biexciton Auger lifetimes ($\boldsymbol{\tau_{A,XX}}$) gained from pump fluence dependent PL decay measurement for NC solutions (vertical axis) *versus* estimations from trion lifetimes ($\boldsymbol{\tau_{A,X^+}}$ and $\boldsymbol{\tau_{A,X^-}}$) measured with opto-electrical set-up (horizontal axis). Diamond, circle, inverted triangle, and triangle correspond to CdSe (r = 1.7

nm)/CdS (*l* = 3.7 nm), CdSe (*r* = 1.7 nm)/CdS (*l* = 5.7 nm), CdSe (*r* = 2.0 nm)/CdZnS (*l* = 3.2 nm), and ZnSeTe (*r* = 2.5 nm)/ZnSe (*l* = 1.2 nm)/ZnS (*h* = 0.6 nm) NCs, respectively. Dashed black line indicates the ideal relationship among Auger lifetimes of XX, X^+ and X^- from the superposition principle.[22,23]

Table 4. 1. Characteristic lifetimes of exciton ($\boldsymbol{\tau_X}$), trions ($\boldsymbol{\tau_{X^+}}$ or $\boldsymbol{\tau_{X^-}}$) and biexciton ($\boldsymbol{\tau_{XX}}$) of core/shell heterostructured NCs examined in the present study.

	PL QY* (%)	τ_X (ns)	τ_{X^+} (ns)		τ_{X^-} (ns)			τ_{XX} (ns)
			HOD	stir−*vs*−static	EOD	stir−*vs*−static	photochemistry	pump fluence dependence
CdSe (r = 2.0 nm) /CdZnS (l = 3.2 nm)	85	13.3	1.4	–	2.0	2.1	2.0	0.5
CdSe (r = 1.7 nm) /CdS (l = 3.7 nm)	52	28.7	1.6	–	2.9	3.0	4.1	0.5
CdSe (r = 1.7 nm) /CdS (l = 5.7 nm)	43	33.7	2.7	–	4.6	4.8	6.1	0.8
ZnSeTe (r = 2.5 nm) /ZnSe (l = 1.2 nm) /ZnS (h = 0.6 nm)	95	59.7	2.6	2.6	10.4	–	–	1.0

**Solution PL QYs are measured under excitation at 450 nm* ($\langle N \rangle \ll 0.01$).

We continue applying current experimental methods on AR characteristics of charged excitons on core/shell NCs with varying compositions and/or dimensions (shown in **Fig. 4.1c**) and evaluate them in comparison with experimental results gained from previous methods (**Fig. 4.4**, see also **Table 4.1**). We recall that the stir-*versus*-static method or photochemistry permit to assess AR rates of only one type of trions: X^- for CdSe based NCs and X^+ for ZnSeTe based NCs, respectively. By contrast, the present approach allows to experimentally gain both types of trions (**Fig. 4.4a-c**). The lifetimes of X^- of CdSe-based NCs and X^+ of ZnSeTe-based NCs are consistent with those obtained from conventional methods (**Fig. 4.4a-c**). It is noted that, contrarily to CdSe-based devices, EOD and HOD employing ZnSeTe/ZnSe/ZnS NCs exhibit slow electron accumulation and fast hole accumulation rates, respectively, which is attributed to the relative energy position of the ZnSeTe/ZnSe/ZnS NCs compared to the neighboring charge transport materials.

In chosen NC' s structural variations, AR rates of X^+ are measured to be faster than these of X^-, which complies with previous studies.[26,32,49,55] This is attributed to the greater effective mass of holes than electrons and/or the smaller volume for holes than electrons. Multibands in the valence band and large effective mass of holes entail higher density of hole states than electron states.[56] The high density of holes states is favorable to meet the energy conservation for Auger process involving intraband transition of an extra hole. In addition, holes are strongly confined within the cores, whereas electrons are delocalized over the entire volume, particularly for *quasi*–type II NCs, in which the conduction band offset between core and shell is relatively small. In this geometry, the probability to scatter is much higher for X^+ than the case with X^-.[57]

As discussed above (**Fig. 4.3d**), we confirm that AR decay lifetimes of XX, X^+ and X^- fall in line with the ideal relation line expected from the superposition principle with only marginal deviations (**Fig. 4.4d**), implying that the present method is indeed effective to evaluate AR characteristics of NCs regardless of their compositions and potential profiles. Plus, the coherent relationship among multicarrier states attests that superposition principle is indeed effective to core/shell heterostructured NCs.

We note that the present charging method is only valid to gain singly charged excitons, and is not effective to attain doubly (X^{2-} or X^{2+}) or higher charged states. Our calculation[58] shows that the presence of one extra charge imposes extra potential to another charge carrier with the same polarity. Given the energy penalty, doubly or higher charged NCs are unlikely to exist in the chosen experimental condition ($V_{app} =$ 1 V in EOD, 2V in HOD, respectively), wherein more than 50 % of uncharged NCs are still present. Experimentally, higher operational voltage (4 V) results in rapid charge accumulation to a greater extend of NC charging (52 % and 22 % in 30 min for EOD and HOD, respectively), but the extracted fast decay dynamics from EOD and HOD are still same to X^- and X^+

attained at the low operation voltage. Operation of the devices above 4 V for an extended period has yielded device breakdown, limiting us to gain doubly higher charged states of NCs.

4.4. Summary

In summary, we have demonstrated an opto–electrical method that enables precise evaluation of AR rates of positively and negatively charged excitons in core/shell heterostructured NCs. The moderate operating voltage within inert atmosphere guarantees non–destructive charge carrier injection into NCs, allowing to evaluate the AR characteristics of NCs regardless of their compositions or structures. AR rates of charged excitons attained from present approach agree well with those attained from the conventional photo–charging approaches (photochemistry and stir–*versus*–static method) and the superposition principle, corroborating the effectiveness of the present approach and also the superposition principle. The present method provides the capability of direct, precise assessment of both X^+ and X^- to comprehend multicarrier dynamics in NCs, boosting their use in light–emitting diodes and laser devices based on NCs.

Chapter 5.④ Type-Ⅰ $AgIn_XGa_{1-X}S_2/AgGaS_2$ Ⅰ-Ⅲ-Ⅵ/Ⅰ-Ⅲ-Ⅵ core/shell heterostructures

5.1. Introduction

Colloidal semiconductor NCs are solution processable nano-emitters that emanate size-dependent tunable energies of photons with a narrow linewidth.[1,2,61] High-precision size control of NCs permits to fine-tune the emission wavelength in a nanometer scale.[3,99,100] In addition, defect-free heteroepitaxy in a core-shell geometry allows stable and efficient radiation of NCs under various circumstances.[101-104] These advances in chemistry accelerate the use of NCs in a range of photonic applications including displays[9,105-107], lasers[64,108], imagings[36,109], and energy conversion systems[34,35,110,111].

Demand for practical use in everyday light-emitting applications drives to expand the materials envelope for core-shell NCs toward semiconductors free from heavy metal elements.[112-120] Among potential candidates, I-III-VI_2 alloyed compounds made of Ag, (In,Ga) and S (hereinafter referred to as AIGS) have been of particular interest, as they promise efficient light absorption, wide ranging bandgap tunability from visible to near-IR and a narrow emission linewidth.[121-127] Nevertheless, only marginal success has been reported in

---

④ This chapter is based on paper from Lee, H. J.; Im, S.; Jung, D.; Kim, K.; Chae, J. A.; Lim, J.; Park, J. W.; Shin, D.; Char, K.; Jeong, B. G.; Park, J.-S.; Hwang, E.; Lee, D. C.; Park, Y.-S.; Song, H.-J.; Chang, J. H.; Bae, W. K. Coherent heteroepitaxial growth of I-III-VI2 Ag(In,Ga)S2 colloidal nanocrystals with near-unity quantum yield for use in luminescent solar concentrators. *Nat. Commun.* 2023, *14* (1), 3779.

synthesis and structural engineering of AIGS cores. Mostly, an effective way of passivating the surface without rendering unwanted defects, which is the key to the efficiency and stability, has yet to be developed.

Herein, we devise a chemical route for high-quality Ag(In,Ga)S_2-AgGaS_2 (AIGS-AGS) core-shell NCs. Specifically, a molecular precursor containing Ag, Ga and S (Ag-S-Ga$(COOR)_2$) is deployed for homogeneous AIGS nucleation of various compositions and uniform AGS shell growth, enabling us to realize AIGS-AGS NCs displaying color pure emissions in a wide visible region with near unity photoluminescence quantum yields (PL QYs). We conduct spectroscopic analysis to identify the impact of AGS heteroepitaxy on photophysical and chemical properties of AIGS cores and finally discuss the competitive advantages of AIGS-AGS NCs in photonic applications.

5.2. Experimental Section

Ag-S-Ga$(COOR)_2$ preparation. All synthesis was carried out under N_2 atmosphere through the Schlenk line technique. For preparing Ag_2S nanoparticles (NPs), 1 mmol of silver acetate and 5 mL of oleylamine (OAm) were loaded in a three-neck flask and degassed at 50 ° C for 1 hr. After the flask was backfilled with N_2, 2.5 ml of dodecanethiol (DDT) and 1 ml of 0.5 M S dissolved in OAm (S-OAm) were injected into the reaction flask to form Ag_2S NPs. To transform Ag_2S NPs to Ag-S-Ga$(COOR)_2$, 4.5 ml of 0.5 M Ga$(OA)_3$ and 8 ml of 0.5 M

S-OAm were added into the reaction flask and temperature was elevated to 210 ° C. The reaction was verified by the color changes of solutions.

AIGS core (X = 0.5) synthesis. Reaction flask containing 2 ml of Ag-S-Ga(COOR)$_2$ stock solution and 5 ml of OAm was degassed for 1 hr, filled with N_2, and heated up to 210 ° C. 0.15 ml of 0.5 M In(OA)$_3$ precursor were swiftly injected into the flask and the reaction temperature was maintained at the elevated temperature for 30 min. The flask was cooled to room temperature to cease the reaction. Varying the injected volume of In(OA)$_3$ precursor leads to changes in In content (X) in AIGS cores. Resulting AIGS cores were purified twice in glovebox by precipitation (ethanol)/redispersion (toluene) method and finally redispersed in 5 ml of toluene.

AGS shell growth. Reaction flask containing 5 ml of OAm and 300 mg of AIGS cores (X = 0.5) were degassed at 110 ° C for 1 hr, backfilled with N_2 and heated up to 240 ° C. At the elevated temperature, 0.3 ml of Ag-S-Ga(COOR)$_2$ precursor solution and 0.3 ml of 0.5 M S-OAm were added and the reaction temperature was maintained for 1 hr to grow 0.3 nm thick AGS shell. The injecting volume of Ag-S-Ga(COOR)$_2$ precursor and 0.5 M S-OAm were varied for AGS shell thickness control. Resulting AIGS-AGS NCs were purified twice in glovebox by precipitation (ethanol)/redispersion (toluene) method and finally redispersed in 5 ml of toluene for further characterization and applications.

Characterization. UV−Vis, PL and PL QY measurements were conducted with UV−1800 (Shimadzu), FluoroMax−4 (Horiba) and quantaurus−QY plus (hamamatsu photonics), respectively. HR−TEM images were obtained with Talos F200i working at 200 kV. The crystalline structures of NCs were investigated with XRD at the 5A beamline (λ = 0.154 nm) of the Pohang Accelerator Laboratory (PAL). Time−resolved emission spectra (TRES) measurement was conducted using the 405 nm (3.06 eV) excitation beam at 500 kHz repetition rate (PicoQuant, LDH−D−C−405 laser diode) with photo multiplier tube (PicoQuant, PMA−C182−N−M) coupled to the monochromator (Teledyne Princeton Instruments, SpectraPro SP−2150). Single−dot measurements were conducted using Hanbury Brown−Twiss setup with the 450 nm (2.76 eV) excitation beam (Pico Quant, LDH−D−C−450 laser diode). The laser beam was focused on the sample using the oil immersion objective (Olympus, UPLXAPO100XO, 1.45 NA) and signals were collected through the same objective lens and directed to single−photon avalanche diodes (Micro Photon Devices, PDM Series) connected with time−correlated single photon counting module (PicoQuant, HydraHarp 400) or to EMCCD camera (Princeton Instruments, ProEM HS1024BX3) attached to the spectrometer (Princeton Instruments, IsoPlane SCT320). The chemical composition of AIGS was analyzed by inductively coupled plasma atomic emission spectroscopy (ICP−AES) (Perkin−Elmer, OPTIMA−4300DV). The existence of Ag−S−

$Ga(COOR)_2$ complex is verified by MALDI–TOF (Applied Biosystems, Voyager DE–STR).

LSC fabrication and characterization. InP–ZnSeS NCs and AIGS–AGS NCs with similar PL QY (~ 95 %) were used for LSCs. LSCs with NC dispersion in toluene were loaded in a clear quartz cuvette (100 × 500 × 10 mm^3) to avoid inevitable PL QY drop during the polymerization process. The efficiency of LSC was monitored by a crystalline silicon solar cell (10 × 50 mm^2) mounted at one edge of LSC without index–matching oil, while the metal–based reflective films were installed on the other three sides. The top and bottom sides of LSC were enclosed by clear quartz, whose light trapping efficiency is 0.75 due to the refractive index difference between air and the quartz glass. The efficiency and absorptance of LSC with different concentrated NCs were repeatedly evaluated under 420 nm LED sources (1.4 mW/cm^2, 3.0×10^{15} $photons/cm^2$).

5.3 Results and Discussion

Coherent heteroepitaxial growth of AIGS–AGS NCs

The up–to–date chemistry still faces hurdles in attaining homogeneity in AIGS alloyed core synthesis and passivating the surface trap states, as seen from their mediocre optical characteristics (*i.e.*, record high PL QY of 70 % and an emission linewidth of 40–100 nm).[123–126] The broad emission linewidth relates to the size and/or composition inhomogeneities among AIGS alloyed cores, which are attributed to substantial difference in reactivity among cation precursors, specifically the low reactivity of Ga precursors compared to their cation counterparts (Ag or In precursors). The reactivity of In precursors ($In(COOR)_3$) far exceeds that of Ga precursors ($Ga(COOR)_3$), as predicted from the substantial bond-dissociation energy difference between Ga^{3+} *versus* In^{3+} to carboxylate ligands (−COOR). In addition, Ag precursor is prone to be reduced to precipitate in a form of silver metal (Ag) at an elevated temperature, at which Ga precursor is activated to participate in the chemical reaction. Therefore, the conventional hot injection method, *i.e.*, the injection of S precursor into the mixed solution of Ag, In and Ga precursors, is not applicable for homogenous AIGS core synthesis unless the reactivities of cation precursors are complemented.

At the same time, the chemistry for optically active defect-free heteroepitaxy is necessary to boost the optical performance of AIGS cores. Previously, zincblende ZnS[123,124] or amorphous GaS_X[125,126] have been suggested, but the structural difference between AIGS core and these shell materials has yielded interfacial defects that deteriorate the spectral purity and luminescence efficiency of resulting NCs. In this respect, $AgGaS_2$ (AGS) is ideal for the shell materials not only because its crystal structure is same to AIGS with a manageable lattice mismatch (*i.e.*, the mismatch between $Ag(In,Ga)S_2$ ($X = 0.5$) *versus* $AgGaS_2$ = 1.2 % in a axis and 3.9 % in c axis) but also because it constructs straddling energy gap (Type I heterojunction) that facilitates efficient recombination of charge carriers in the AIGS phase. Obviously, for the AGS shell growth, the reactivities of cation precursors should be managed to avoid unwanted side reactions (homogeneous nucleation of Ag_2S nanoparticles or precipitation of Ag).

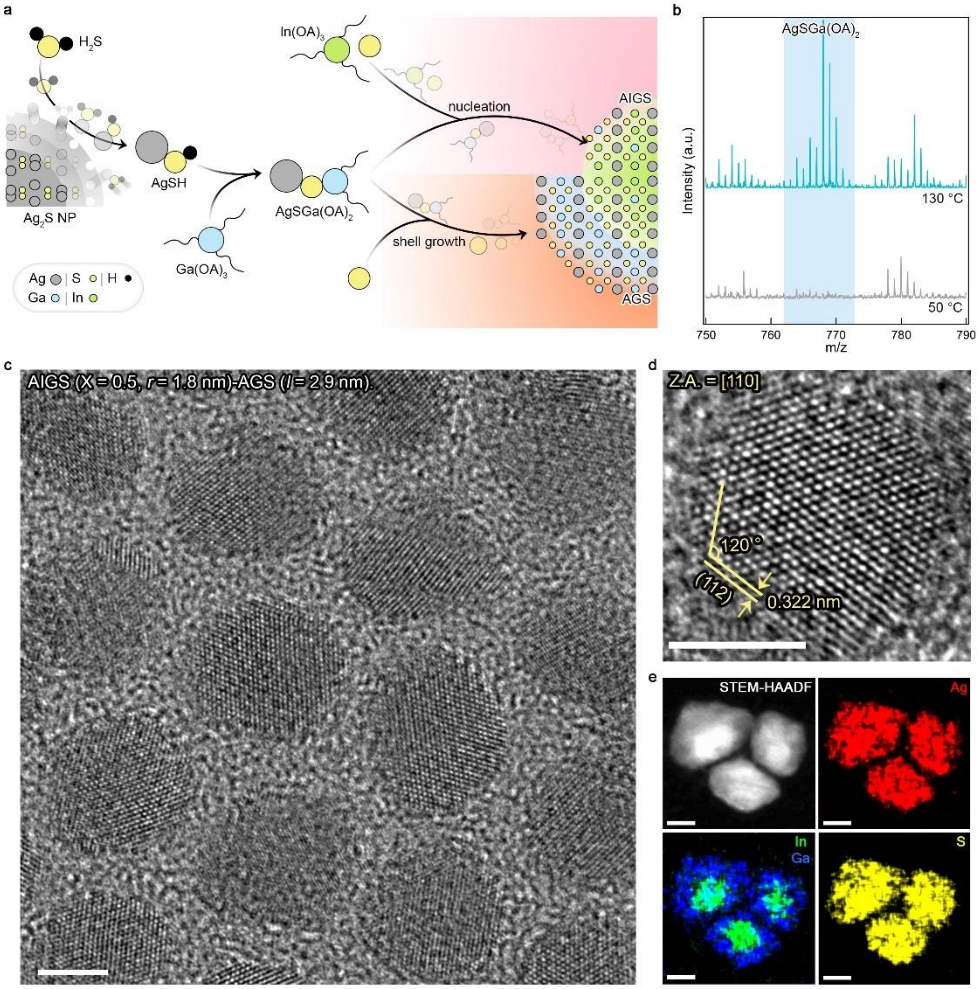

Figure 5. 1. $Ag(In,Ga)S_2$–$AgGaS_2$ (AIGS–AGS) core–shell NCs. (a) Schematic illustration of AIGS–AGS NC synthesis. Key reactants and chemical intermediates are depicted. (b) MALDI–TOF mass spectra of the reactants containing Ag, S, Ga and ligands (oleic acid (OA) and oleyl amine (OAm)) taken at different reaction temperatures (130 °C (top, cyan) and 50 °C (bottom, gray)). The colored background highlights the presence of Ag–S–$Ga(OA)_2$ complex at the elevated temperature. The spectra are vertically shifted for visual

clarity. (c,d) HR−TEM images of AIGS ($\mathrm{X} = 0.5$, radius $(r) = 1.8\,nm$)−AGS (shell thickness $(l) = 2.9\,nm$) NCs. A NC is measured along the [110] axis. (e) STEM−HAADF image and EDS elemental mapping of Ag (red), In (green), Ga (blue) and S (yellow) for AIGS ($\mathrm{X} = 0.9$, $r = 2.95\,nm$)−AGS ($l = 2.7\,nm$) NCs. Scale bars are 5 nm.

Above consideration imposes a chemical means to balance the reactivities among cation precursors for achieving AIGS–AGS core–shell NCs. In the present study, we devise a molecular precursor containing Ag, Ga and S (Ag–S–Ga(COOR)$_2$) for both AIGS core synthesis and AGS shell growth (**Fig. 5.1a**). Ag–S–Ga(COOR)$_2$ stock solution is prepared in following reaction steps. (i) Ag_2S nanoparticles (NPs) are formed to avoid Ag reduction at an elevated temperature. (ii) Ag_2S NPs react with in–situ generated H_2S from the mixture of S and alkylamine at an elevated temperature ($T \geq 130$ ℃) and dissolve into a form of AgSH. (iii) AgSH reacts with Ga(COOR)$_3$ to form Ag–S–Ga(COOR)$_2$. The dissolution of Ag_2S NPs is monitored with changes in their colors (dark brown to transparent orange) and TEM analysis. The role of in–situ generated H_2S is validated by the comparative experiments with *versus* without degassing for H_2S removal. The formation of Ag–S–Ga(COOR)$_2$ is confirmed with MALDI–TOF mass spectrometry (**Fig. 5.1b**). Ag–S–Ga(COOR)$_2$ stock solution is kept at the room temperature for AIGS core synthesis and AGS shell growth. The injection of In precursor (In(COOR)$_3$) into Ag–S–Ga(COOR)$_2$ stock solution at an elevated temperature ($T = 210$ ℃) bursts AIGS nucleation and subsequent growth. The addition of Ag–S–Ga(COOR)$_2$ stock solution in the AIGS core containing solution allows to grow AGS shell on top of AIGS core. HR–TEM, STEM–HAADF and EDS analysis verify that resulting NCs are indeed heterostructured in AIGS−AGS core−shell geometry (**Fig. 5.1c−e**).

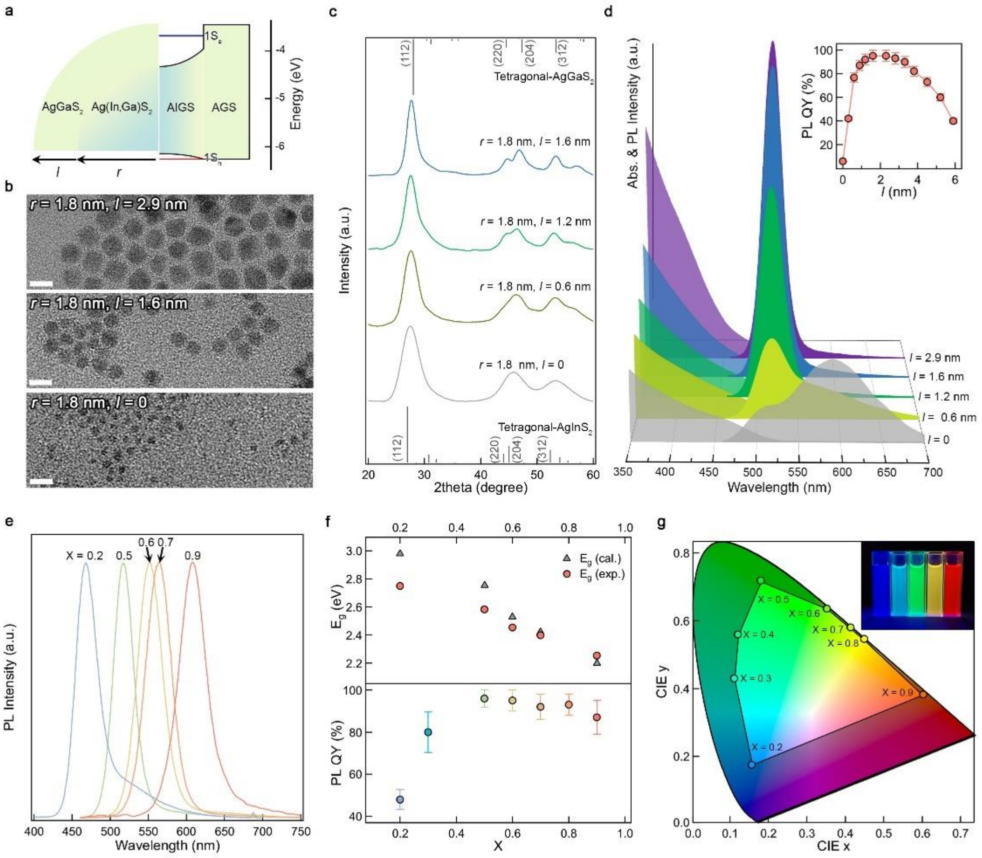

Figure 5. 2. AIGS−AGS NCs with variable core compositions and shell dimensions. (a) Schematic illustrations of the geometry (left) and potential profile (right) of AIGS−AGS NCs. Blue and red lines indicate the lowest quantized energy state for electron ($1S_e$) and hole ($1S_h$), respectively. (b) TEM images (scale bars = 10 nm), (c) X−ray diffraction patterns, and (d) UV−Vis absorption and PL spectra of AIGS ($\mathbf{X = 0.5}$, $r = 1.8\,nm$)−AGS NCs with varying shell thicknesses ($0 \leq l \leq 2.9\,nm$). The inset displays PL QYs as a function of shell thickness. (e) PL spectra, (f) energy gaps ($1S_e - 1S_h$) obtained from UV−Vis spectra (top) and PL QYs (bottom), and (g) their color coordinates of AIGS−AGS ($l = 1.6\,nm$) NCs with varying

In contents ($0.2 \leq X \leq 0.9$) (inset: a photographic image of AIGS−AGS NCs with varying In ratios). Gray triangles in (f) represent our calculation results for which homogenously alloyed AIGS cores are taken into account.

AIGS core and AGS shell build Type I heterojunction, in which both electron and hole wavefunctions are confined within AIGS core (**Fig. 5.2a**). In such potential profile, large versatility in controlling the chemical composition of AIGS core and the dimension of AGS shell provide AIGS–AGS NCs with brightness and stability as well as with expansive emission tunability. The reaction scheme enables uniform AGS shell growth with varying thicknesses (**Fig. 5.2b**), while keeping the crystal structure (chalcopyrite) remains unchanged throughout the shell growth (**Fig. 5.2c**). AGS shell growth effectively confines the charge carriers in AIGS core and promotes radiative recombination, as shown in the enhancement of the optical transition between the lowest quantized states for electron and hole ($1S_e-1S_h$) (**Fig. 5.2d**) and ensemble PL decay dynamics. Particularly, the dominant broadband emission due to the surface defects when no shell is present is greatly suppressed upon AGS shelling. We observe that PL QY reaches to near unity with AGS shell thickness of 1.6–2.9 nm (**Fig. 5.2d inset**), indicating the heteroepitaxy of AGS shell on AIGS core free from the formation of optically active defects. The shell thickness greater than 3.0 nm accompanies gradual decrease in PL QYs, which is attributed to the creation of internal defects by the accumulated structural stress between AIGS core and thick AGS shell.

The composition of AIGS cores can be tuned by varying the molar ratio of injected In *versus* Ga contents (**Fig. 5.2e–g**). To obtain In content (**X**) in AIGS cores, we carry out elemental analysis (ICP−AES) or estimate it from XRD. The value of X appears greater than the feed ratio, implying that In precursor indeed leads the nucleation. The energy gaps ($E_g = 1S_e - 1S_h$) inferred from absorption spectra deviate from our quantum mechanical calculation where homogeneously alloyed AIGS cores and NCs' dimensions are taken into account, and the discrepancy becomes greater for NCs having lower In contents (upper panel of **Fig. 5.2f**). These coherently suggest that synthesized AIGS cores have composition gradients with In−rich interior and Ga−rich exterior. Nevertheless, resulting AIGS cores possess tetragonal crystal structure regardless of their compositions (chalcopyrite), which promises the heteroepitaxy of tetragonal AGS shell onto them. The controllability of AIGS core compositions allow to expand the emission envelope of AIGS−AGS NCs to cover the entire visible region (**Fig. 5.2e−g**). The capability for heteroepitaxy with AGS shell ensures high PL QYs. It is noted that AIGS−AGS NCs having higher Ga contents ($X = 0.2$) show relatively low luminescence efficiencies (PL QY = 50 %) due to the ineffective passivation of charge carriers by AGS shell (lower panel of **Fig. 5.2f**).

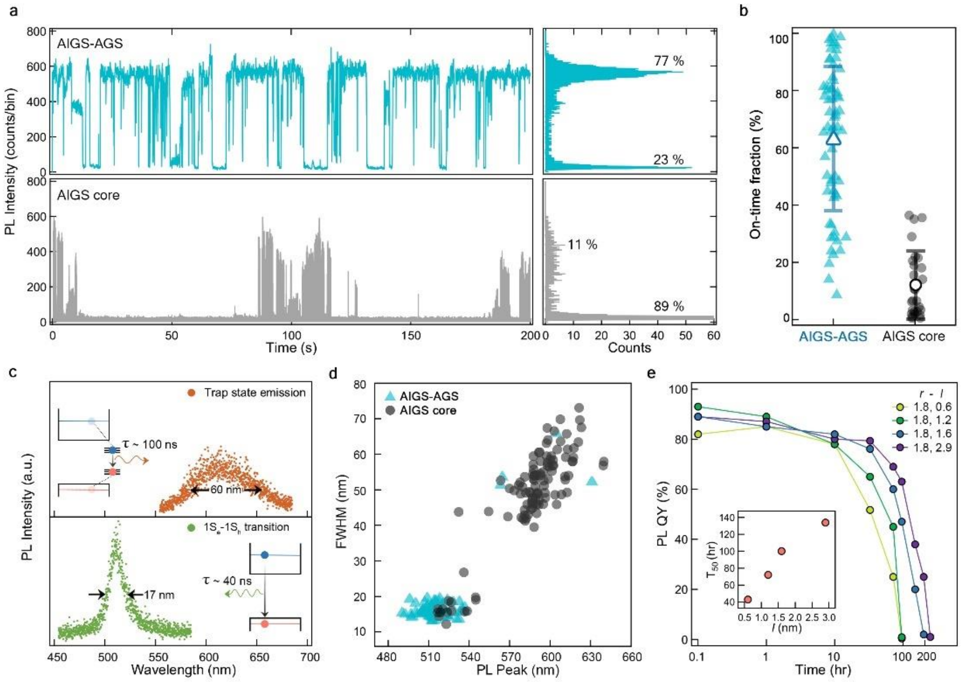

Figure 5. 3. Impact of AGS heteroepitaxy on photophysical and photochemical properties of individual AIGS−AGS NCs. (a) Representative PL intensity trajectories (left) and PL intensity histograms (right) of AIGS−AGS NC (top, cyan) *versus* AIGS core (bottom, gray) (bin time = 50 ms). (b) On−time fraction statistics of individual AIGS−AGS NCs (left, cyan) and AIGS cores (right, gray). Average on−times are 63.9 % and 12.3 % for AIGS−AGS NCs and AIGS cores, respectively. (c) Emission spectra from $1S_e-1S_h$ transition (bottom, AIGS−AGS NC) and surface trap states (top, AIGS core). The composition and dimensions are $\mathrm{X}=0.5$, $r=1.8\,nm$, and $l=0 \text{ or } 1.6\,nm$ for AIGS cores or AIGS−AGS NCs, respectively. The insets depict luminescence mechanism and its characteristic time. (d) PL peak *versus* FWHM distribution in individual AIGS−AGS NCs or AIGS cores. (e) Time dependent PL QYs of AIGS ($\mathrm{X}=0.5$,

$r = 1.8\ nm$)−AGS NCs with varying shell thicknesses ($l = 0.6, 1.2, 1.6\ or\ 2.9\ nm$) upon oxidative test. The inset displays T_{50}, the time when PL QY reaches to the half of initial values.

Two distinct PL emissions are present in AIGS cores, the narrowband emission (FWHM = 30 nm) originating from $1S_e$−$1S_h$ optical transition with a characteristic decay time (τ_{rad}) of $40\,ns$ and the broadband emission (FWHM of 40−70 nm) at lower energy positions with a slower recombination rate ($\tau_{rad} = 100\,ns$). The broadband emission is greatly suppressed by the AGS shell growth, implying that the broadband emission is related to the surface state of AIGS cores, rather than the compositional inhomogeneity among AIGS cores or the presence of chemical impurities in AIGS cores, which otherwise leave electronic footprints even after the passivation with AGS shell. The increase in PL QYs together with the suppression of the broadband emission in AIGS−AGS NCs signifies the effective passivation of the surface−related recombination channels.

The enhanced light emission of AIGS−AGS NCs can be also manifested in individual NCs, so we investigate the effect of AGS shell in single−dot spectroscopy. **Fig. 5.3a** displays representative single−dot PL intensity traces for an AIGS core (lower panel) *versus* an AIGS−AGS ($l = 1.6\,nm$) NC (upper panel). While the AIGS core suffers from severe PL blinking with on−time fraction of 11 %, AIGS−AGS NC is highly emissive with on−time fraction of 77 %. This implies that, in AIGS−AGS NCs, photoexcited charge carriers are effectively confined within AIGS core in Type I band structure and yield radiative recombination, instead of trapping in surface defects. Based on 50 individual NCs, the on−time fraction of individual

NCs increases on average from 12 % (no AGS shell) to 64 % after 1.6 nm−thick AGS shell growth (**Fig. 5.3b**). A large NC−to−NC variation of the on−time statistics observed from AIGS−AGS NCs likely happens due to the change in the environment medium from solvent to air, which was unavoidable in the process of single−dot measurement.

In addition, for AIGS−AGS NCs, the surface−state related broadband emission is near−completely suppressed and the narrowband emission from $1S_e - 1S_h$ transition is prevailing, as demonstrated in individual NC spectra in **Fig. 5.3c**, AIGS core (FWHM = 60 nm, upper panel) *versus* AIGS−AGS NC (FWHM = 17 nm, lower panel). The PL emission peaks of individual AIGS cores are distributed near the surface emission (~ 600 nm) as observed in ensemble spectrum (gray trace in **Fig. 5.2d**) with a broad linewidth (~ 48 nm on average). In a sharp contrast, the PL emission peaks of individual AIGS−AGS NCs are narrowly positioned near 520 nm, which is corresponding to the band edge emission, along with a very narrow linewidth (~ 17 nm on average). All these findings are consistent with ensemble data and again corroborate the fact that the surface trap states of AIGS core are effectively passivated by AGS shell.

The effective passivation by AGS shell is also validated by the oxidative test (**Fig. 5.3e**). For the oxidate test, we monitor the change in PL QYs of NC solution upon exposure to air over time. The increase in the AGS shell thickness expands the half−lifetime of AIGS−AGS NCs, supporting that the width of potential wall (AGS shell thickness) is indeed responsible for the enhanced stability rather than the atomistic surface passivation. These results coherently attest that our approach, the heteroepitaxy of AGS shell on AIGS core, is an effective means to boost the photophysical and photochemical performance of NCs.

We note that the present approach, *i.e.*, heteroepitaxy with I–III–VI_2 AGS shell, stands in sharp contrast to previous attempts to passivate the surface of AIGS cores using zincblende II–VI ZnS shells[123,124], amorphous GaSx[125,126], or z–type ligands[127] regarding the emission linewidth and efficiency. Specifically, ZnS shell or z–type ligand aids to enhance PL QYs up to 70 % by deactivating non–radiative recombination channels at the surface of AIGS cores, but resulting NCs still entail strong broadband emission (~ 100 nm). Amorphous GaSx shell eliminates the broadband emission of AIGS cores, but only marginal PL QY enhancement (~70 %) is allowed due to its inherent structural imperfection. By contrast, heteroepitaxy with AGS shell guarantees both bright and narrowband PL emission of AIGS–AGS NCs.

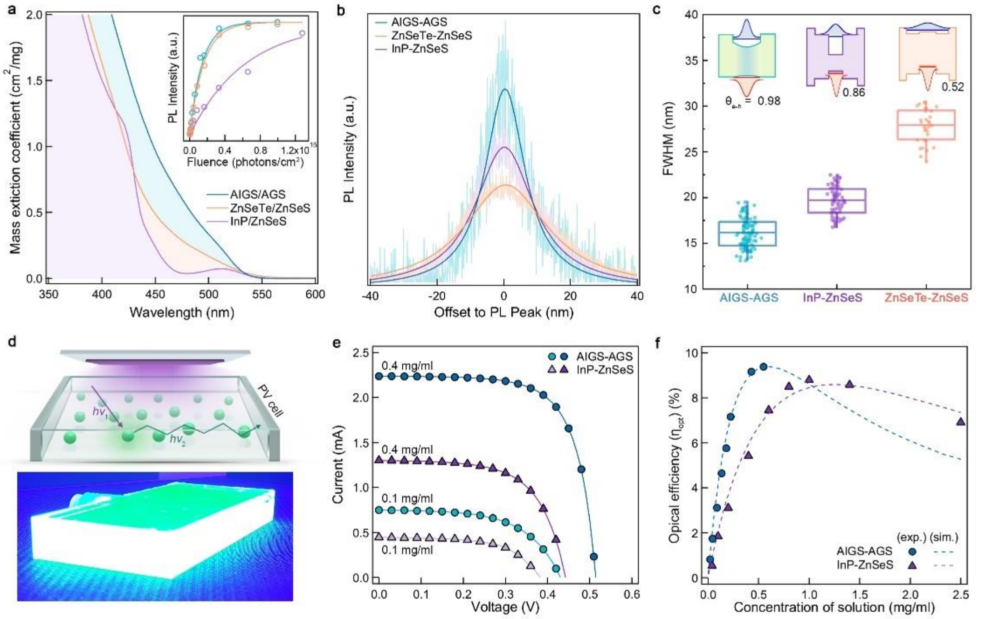

Figure 5. 4. Competitive advantages of AIGS−AGS NCs and their application to luminescent solar concentrator. (a) Mass extinction coefficients, and (b) representative PL spectra in individual NC level and (c) FWHM statistics of AIGS−AGS, ZnSeTe−ZnSeS, and InP−ZnSeS NCs. The inset in (a) shows pump−fluence−dependence of the single exciton PL intensities to gain optical absorption cross−sections (σ) of NCs @ 450 nm (σ = 8.15, 6.54, and 1.58 (E−15 cm^2) for AIGS−AGS, ZnSeTe−ZnSeS, and InP−ZnSeS NCs, respectively). Single exciton PL amplitudes from pump−fluence dependence measurements are fitted based on Poisson statistics of photon absorption to gain optical cross−sections. The PL spectra in (b) are fitted with single Lorentzian function and normalized by their integrated areas. The insets in (c) display the band alignment of each heterostructured NC and the electron−hole overlap integral ($\boldsymbol{\theta_{e-h}}$). (d) Schematic and photographic image

of a LSC, whose size is 100 x 50 x 10 mm^3. The incident photons from top of LSC (50 X 100 mm^2) are absorbed, re-emitted, and waveguided to the edge mounted solar cell (50 X 10 mm^2). Here, the geometric factor of LSC is 10 and light source is 420 nm LEDs. (e) Current-voltage characteristics of edge-mounted c-Si cells with 0.1 and 0.4 mg/ml of AIGS-AGS (circle) or InP-ZnSeS (triangle) NC solutions. (f) η_{opt}s of LSCs with varying concentrations of AIGS-AGS and InP-ZnSeS NC solution (exp.) with a theoretical simulation (sim.)[128]. Improved light absorption of AIGS-AGS NCs allows us to obtain higher efficiency of LSC with reduced NC concentrations or film thicknesses.

As demonstrated, AIGS−AGS NCs present a narrow emission linewidth and near-unity PL QY, promising their practical use in a range of photonic applications. To clarify the competitive advantages of AIGS−AGS NCs, we compare their optical properties with state-of-the-art heavy metal-free core-shell NCs (InP−ZnSeS NCs[114−117] and ZnSeTe−ZnSeS NCs[118−120]), both of which have similar PL energy ($peak\ PL \approx 520\ nm$) and total dimension ($diameter\ (d) = 7.0\ nm$) (Fig. 5.4). All NCs exhibit PL QYs over 90 % and narrow size distribution ($\sigma < 15\ \%$), implying that the structural or compositional inhomogeneities are well controlled. However, AIGS−AGS NCs have a greater mass extinction coefficient than InP−ZnSeS NCs by a factor of 1.5−4 at the blue to UV-A region (Fig. 5.4a), leading to an important implication for down-conversion application under the excitation photon sources in blue to UV-A region. In addition, AIGS−AGS NCs show very narrow spectral linewidths in both ensemble and individual NC levels (Fig. 5.4b, c). Specifically, AIGS−AGS NCs have a narrower spectral linewidth ($16.1 \pm 1.6\ nm$) compared to InP−ZnSeS NCs ($19.6 \pm\ 1.6\ nm$) or ZnSeTe−ZnSeS NCs ($27.8 \pm 1.9\ nm$). We speculate that the narrow spectral linewidth of AIGS−AGS NCs is attributed to the effective confinement of charge carriers in Type I heterojunction potential profile. The narrow spectral linewidth of individual AIGS−AGS NCs is reflected to their collective PL spectra (FWHM of ensemble PL = 30 nm), which is much narrower than the record narrow spectral linewidths of ensemble InP−ZnSeS NCs (FWHM = 36 nm)[114,115,117] or

ZnSeTe–ZnSeS NCs (FWHM = 41 nm)[118]. The narrower spectral linewidth and higher extinction coefficient of AIGS–AGS NCs promise a competitive edge over other heavy metal–free NCs in a range of photonic applications implementing down–converting NC layers. For example, the use of AIGS–AGS NCs in state–of–the–art NC displays in replace of InP–ZnSeS NCs awards not only an expanded color space of images but also thinness and lightweightness that are prerequisite for augmented reality or virtual reality displays.

The advantages in the form factors are of particular interest to luminescent solar concentrators (LSCs) that demand large–area down–converting NC films for an efficient harvest of sunlight. **Fig. 5.4d–f** exemplify the competitiveness of AIGS–AGS NCs in LSCs. In LSCs, NC layer absorbs incident light and emits down–converted photons, which are waveguided to the edge, where the solar cell is mounted (**Fig. 5.4d**). The optical efficiency (η_{opt}) of LSC, defined by the ratio between incident photons through the top window and collected photons to the edge–mounted solar cells, is normally a function of incident photon absorption, re–emission efficiency of luminophore, re–absorption, and waveguiding efficiency of structure.[128–130] Thus, the desirable characteristics of luminophores are a high absorption coefficient at the wavelength of the incident light, high PL QY, and a large stoke shift. Our AIGS–AGS NCs fulfill the requirements of luminophores for LSCs at the point of absorption and re–

emission efficiency (~ 95 %). Especially, the high absorption coefficient of AIGS−AGS NCs allows us to save the materials for LSCs by sufficiently absorbing incident light through dilute concentrated NCs. In addition, the small overlap between absorption and emission spectra of AIGS−AGS NCs (shown in **Fig. 5.2d**) suppresses the re−absorption loss in the LSC, thereby leading to the improved efficiency.

Regarding these factors, we compared the performance of LSC with AIGS−AGS NC solution to one employing InP−ZnSeS NC solution of various concentrations. Here, η_{opt} of LSC is derived from the short circuit current of edge−mounted crystalline silicon solar cell (10 × 50 mm^2) and incident light intensity (shown in **Fig. 5.4e**). As more luminophores are included in LSC, its η_{opt} increases typically at a lower concentration of luminophore due to enhanced light absorption. Thus, η_{opt}s of dilute concentrated LSCs with InP−ZnSeS and AIGS−AGS NCs are correlated with their concentration. Despite similar trends in the concentration and η_{opt}, the LSC employing AIGS−AGS NCs exhibits higher η_{opt} than LSC with InP−ZnSeS NCs at a low concentration (**Fig. 5.4f**). High absorption coefficient of AIGS−AGS NCs provides better absorption of incident photons, resulting in the increased η_{opt}. Consequently, the luminophore concentration for maximized η_{opt} is much lower in the case of AIGS−AGS NCs compared to the case of InP−ZnSeS NCs. According to the theoretical simulation and experiments, the optimized concentration of LSC with AIGS−AGS NCs is around 0.5 mg/ml[128], whereas 1 mg/ml of InP–ZnSeS NCs is required to reach the peak η_{opt}. Consistently with the expectation in LSC performance from the optical properties of AIGS–AGS NCs, the LSC experiment implies that AIGS–AGS NCs are strong candidates to demonstrate thin LSCs.

Thin LSCs would be beneficial to reduce fabrication costs and minimize material waste for solar energy harvesting and optoelectronic devices. Besides, the expected advantage from LSCs implementing AIGS–AGS NCs is enhanced mechanical strength, which plays a critical role in flexible and wearable devices. Given that the tensile and strain applied to the thin film is much smaller than those to the thick film,[131] flexible LSC with a thin absorption layer will be more robust to the deformation of its shape, which is suitable to cover curved surfaces. Moreover, it would be helpful for the rigid LSC, expected to cover building envelope. Field–installed LSC will be frequently exposed to harsh outdoor conditions, where the strain and tensile will be applied continuously due to temperature changes throughout the year. If the LSC consists of a thin absorption layer, delamination and crack from thermal mechanical stress will be reduced. In these respects, AIGS–AGS NCs not only ensure higher performance of LSCs but also contribute to realizing economic, environmental, and reliable LSCs.

5.4. Summary

In summary, we have presented new class of environmentally benign nano–emitters made of $Ag(In,Ga)S_2$–

$AgGaS_2$ I−III−VI_2−I−III−VI_2 core−shell heterostructures. We have designed a chemical scheme that deploys Ag−S−$Ga(COOR)_2$ complex for both AIGS core synthesis and AGS shell growth. The heteroepitaxy of AIGS and AGS constructs Type I potential profile that effectively confines charge carriers within the emissive core without the creation of optically active defects, allowing for near−unity PL QY and photochemical stability. Resulting AIGS−AGS NCs show remarkably high extinction coefficient and narrower spectral linewidth compared to state−of−the−art heavy metal−free NCs, promising their immediate use in a range of practicable photonic applications.

Conclusion

The global stringent regulation on the heavy metal elements in the industry has driven the research toward a new class of environmentally benign NCs. InP-based NCs has emerged as a well-developed alternative, which exhibits near-unity PL QYs across green to red. Nevertheless, InP-based NCs suffer from significant drawbacks that hinder their use in the industrial fields. such as low absorption coefficient at blue spectral regime, broad emission linewidth and the challenge of realizing blue-emitting InP-based NCs.

In this dissertation, we present synthesis and characterization of spherical quantum well $ZnSe/ZnSe_{1-X}Te_X/ZnSe$ NCs and core/shell $AgIn_XGa_{1-X}S_2/AgGaS_2$ NCs, which represent new class of environmentally benign NCs bearing near-unity PL QYs across full visible range (450 nm to 620 nm).

Chapter 2 focuses synthesis of $ZnSe_{1-X}Te_X$ SQW NCs across visible regime and their applications in the dichromic white NC-LEDs. Chapter 3 and 4 delve into the unique optical and photophysical properties of $ZnSe_{1-X}Te_X$ SQW NCs. Structural analysis of NC ensemble and photophysical analysis of individual NC analysis, combined with computational calculation, reveal the origin of asymmetric PL spectra observed in the blue $ZnSe_{1-X}Te_X$ SQW NCs, which is attributed to morphological inhomogeneity of Te excitonic states in the $ZnSe_{1-X}Te_X$ emissive layer. Additionally, newly designed opto-electrical charging methods enable a comprehensive analysis of the multicarrier dynamics of $ZnSe_{1-X}Te_X$-based NCs.

In Chapter 5, we present the first Ⅰ-Ⅲ-$Ⅵ_2$/Ⅰ-Ⅲ-$Ⅵ_2$ core/shell heterostructures, AIGS/AGS NCs, which exhibit an absorption coefficient fourth times higher than that of InP-based NCs, near-unity PL QYs and ultra-narrow emission linewidth (FWHM ~30 nm). The introduction of Ag-S-Ga(OA)2 intermediates plays key role in the AIGS nucleation and AGS shell growth. High absorption near blue regime with near-unity PL QY of AIGS/AGS NCs realizes enhanced optical efficiency with a reduced amount of NCs compared to InP/ZnSeS NCs.

Overall, this study contributes to the development of environmentally benign NCs with superior optical properties, expanding their potential in a wide range of photonic applications.

Bibliography

(1) Brus, L. Electronic wave functions in semiconductor clusters: experiment and theory. *J. Phys. Chem.* **1986**, *90* (12), 2555−2560.

(2) Ekimov, A. I.; Efros, A. L.; Onushchenko, A. A. Quantum size effect in semiconductor microcrystals. *Solid State Commun.* **1985**, *56* (11), 921−924.

(3) Murray, C.; Norris, D. J.; Bawendi, M. G. Synthesis and characterization of nearly monodisperse CdE (E= sulfur, selenium, tellurium) semiconductor nanocrystallites. *J. Am. Chem. Soc.* **1993**, *115* (19), 8706−8715.

(4) Hines, M. A.; Guyot−Sionnest, P. Synthesis and Characterization of Strongly Luminescing ZnS−Capped CdSe Nanocrystals. *J. Phys. Chem.* **1996**, *100* (2), 468−471.

(5) Park, Y.−S.; Lim, J.; Klimov, V. I. Asymmetrically strained quantum dots with non−fluctuating single−dot emission spectra and subthermal room−temperature linewidths. *Nat. Mater.* **2019**, *18* (3), 249−255.

(6) Jeong, B. G.; Chang, J. H.; Hahm, D.; Rhee, S.; Park, M.; Lee, S.; Kim, Y.; Shin, D.; Park, J. W.; Lee, C.; Lee, D. C.; Park, K.; Hwang, E.; Bae, W. K. Interface polarization in heterovalent core–shell nanocrystals. *Nat. Mater.* **2022**, *21* (2), 246−252.

(7) Jang, E.; Jun, S.; Jang, H.; Lim, J.; Kim, B.; Kim, Y. White-light-emitting diodes with quantum dot color converters for display backlights. *Adv. Mater.* **2010**, *22* (28), 3076−3080.

(8) Demir, H. V.; Nizamoglu, S.; Erdem, T.; Mutlugun, E.; Gaponik, N.; Eychmüller, A. Quantum dot integrated LEDs using photonic and excitonic color conversion. *Nano Today* **2011**, *6* (6), 632−647.

(9) Colvin, V. L.; Schlamp, M. C.; Alivisatos, A. P. Light−emitting diodes made from cadmium selenide nanocrystals and a semiconducting polymer. *Nature* **1994**, *370* (6488), 354−357.

(10) Coe, S.; Woo, W.−K.; Bawendi, M.; Bulović, V. Electroluminescence from single monolayers of nanocrystals in molecular organic devices. *Nature* **2002**,

420 (6917), 800−803.

(11) Cho, K.−S.; Lee, E. K.; Joo, W.−J.; Jang, E.; Kim, T.−H.; Lee, S. J.; Kwon, S.−J.; Han, J. Y.; Kim, B.−K.; Choi, B. L. High−performance crosslinked colloidal quantum−dot light−emitting diodes. *Nat. Photonics* **2009**, *3* (6), 341−345.

(12) Hahm, D.; Lim, J.; Kim, H.; Shin, J.−W.; Hwang, S.; Rhee, S.; Chang, J. H.; Yang, J.; Lim, C. H.; Jo, H. Direct patterning of colloidal quantum dots with adaptable dual−ligand surface. *Nat. nanotechnol.* **2022**, *17* (9), 952−958.

(13) Klimov, V.; Mikhailovsky, A.; Xu, S.; Malko, A.; Hollingsworth, J.; Leatherdale, a. C.; Eisler, H.−J.; Bawendi, M. Optical gain and stimulated emission in nanocrystal quantum dots. *Science* **2000**, *290* (5490), 314−317.

(14) Lim, J.; Park, Y.−S.; Wu, K.; Yun, H. J.; Klimov, V. I. Droop−Free Colloidal Quantum Dot Light−Emitting Diodes. *Nano Lett.* **2018**, *18* (10), 6645−6653.

(15) Lee, T.; Kim, B. J.; Lee, H.; Hahm, D.; Bae, W. K.; Lim, J.; Kwak, J. Bright and Stable Quantum Dot Light-Emitting Diodes. *Adv. Mater.* **2022**, *34* (4), 2106276.

(16) Park, Y.−S.; Roh, J.; Diroll, B. T.; Schaller, R. D.; Klimov, V. I. Colloidal quantum dot lasers. *Nature Reviews Materials* **2021**, *6* (5), 382−401.

(17) García de Arquer, F. P.; Talapin, D. V.; Klimov, V. I.; Arakawa, Y.; Bayer, M.; Sargent, E. H. Semiconductor quantum dots: Technological progress and future challenges. *Science* **2021**, *373* (6555), eaaz8541.

(18) Pietryga, J. M.; Park, Y.−S.; Lim, J.; Fidler, A. F.; Bae, W. K.; Brovelli, S.; Klimov, V. I. Spectroscopic and device aspects of nanocrystal quantum dots. *Chemical reviews* **2016**, *116* (18), 10513−10622.

(19) Bae, W. K.; Char, K.; Hur, H.; Lee, S. Single−step synthesis of quantum dots with chemical composition gradients. *Chem. Mater.* **2008**, *20* (2), 531−539.

(20) Bae, W. K.; Nam, M. K.; Char, K.; Lee, S. Gram−scale one−pot synthesis of highly luminescent blue emitting Cd1− x Zn x S/ZnS nanocrystals. *Chem. Mater.* **2008**, *20* (16), 5307−5313.

(21) Asano, H.; Arai, K.; Kita, M.; Omata, T. Synthesis of

colloidal Zn (Te, Se) alloy quantum dots. *Materials Research Express* **2017**, *4* (10), 106501.

(22) Iveland, J.; Martinelli, L.; Peretti, J.; Speck, J. S.; Weisbuch, C. Direct measurement of Auger electrons emitted from a semiconductor light−emitting diode under electrical injection: identification of the dominant mechanism for efficiency droop. *Phys. Rev. Lett.* **2013**, *110* (17), 177406.

(23) Vaxenburg, R.; Lifshitz, E.; Efros, A. L. Suppression of Auger−stimulated efficiency droop in nitride−based light emitting diodes. *Appl. Phys. Lett.* **2013**, *102* (3), 031120.

(24) Bae, W. K.; Park, Y.−S.; Lim, J.; Lee, D.; Padilha, L. A.; McDaniel, H.; Robel, I.; Lee, C.; Pietryga, J. M.; Klimov, V. I. Controlling the influence of Auger recombination on the performance of quantum−dot light−emitting diodes. *Nat. Commun.* **2013**, *4* (1), 2661.

(25) Brovelli, S.; Bae, W. K.; Galland, C.; Giovanella, U.; Meinardi, F.; Klimov, V. I. Dual−Color Electroluminescence from Dot−in−Bulk Nanocrystals. *Nano Lett.* **2014**, *14* (2), 486−494.

(26) Klimov, V. I.; Mikhailovsky, A. A.; McBranch, D.; Leatherdale, C. A.; Bawendi, M. G. Quantization of multiparticle Auger rates in semiconductor quantum dots. *Science* **2000**, *287* (5455), 1011−1013.

(27) Klimov, V. I. Multicarrier interactions in semiconductor nanocrystals in relation to the phenomena of Auger recombination and carrier multiplication. *Annu. Rev. Condens. Matter Phys.* **2014**, *5* (1), 285−316.

(28) Park, Y.−S.; Lim, J.; Makarov, N. S.; Klimov, V. I. Effect of interfacial alloying versus “volume scaling” on Auger recombination in compositionally graded semiconductor quantum dots. *Nano Lett.* **2017**, *17* (9), 5607−5613.

(29) Hahm, D.; Ko, D.; Jeong, B. G.; Jeong, S.; Lim, J.; Bae, W. K.; Lee, C.; Char, K. Environmentally benign nanocrystals: challenges and future directions. *Journal of Information Display* **2019**.

(30) Klimov, V. I. *Nanocrystal quantum dots;* CRC Press, 2010.

(31) Lim, J.; Jeong, B. G.; Park, M.; Kim, J. K.; Pietryga, J. M.; Park, Y. S.; Klimov, V. I.; Lee, C.; Lee, D. C.; Bae, W. K. Influence of Shell Thickness on the Performance of Light-

Emitting Devices Based on CdSe/Zn1-XCdXS Core/Shell Heterostructured Quantum Dots. *Advanced Materials* **2014**, *26* (47), 8034−8040.

(32) Kwak, J.; Bae, W. K.; Lee, D.; Park, I.; Lim, J.; Park, M.; Cho, H.; Woo, H.; Yoon, D. Y.; Char, K. Bright and efficient full−color colloidal quantum dot light−emitting diodes using an inverted device structure. *Nano letters* **2012**, *12* (5), 2362−2366.

(33) Pal, B. N.; Ghosh, Y.; Brovelli, S.; Laocharoensuk, R.; Klimov, V. I.; Hollingsworth, J. A.; Htoon, H. 'Giant' CdSe/CdS core/shell nanocrystal quantum dots as efficient electroluminescent materials: strong influence of shell thickness on light−emitting diode performance. *Nano letters* **2012**, *12* (1), 331−336.

(34) Meinardi, F.; Colombo, A.; Velizhanin, K. A.; Simonutti, R.; Lorenzon, M.; Beverina, L.; Viswanatha, R.; Klimov, V. I.; Brovelli, S. Large−area luminescent solar concentrators based on 'Stokes−shift−engineered' nanocrystals in a mass−polymerized PMMA matrix. *Nat. Photonics* **2014**, *8* (5), 392−399.

(35) Meinardi, F.; McDaniel, H.; Carulli, F.; Colombo, A.; Velizhanin, K. A.; Makarov, N. S.; Simonutti, R.; Klimov, V. I.; Brovelli, S. Highly efficient large−area colourless luminescent solar concentrators using heavy−metal−free colloidal quantum dots. *Nat. nanotechnol.* **2015**, *10* (10), 878−885.

(36) Medintz, I. L.; Uyeda, H. T.; Goldman, E. R.; Mattoussi, H. Quantum dot bioconjugates for imaging, labelling and sensing. *Nat. Mater.* **2005**, *4* (6), 435−446.

(37) Xie, R.; Kolb, U.; Li, J.; Basché, T.; Mews, A. Synthesis and characterization of highly luminescent CdSe− core CdS/Zn0. 5Cd0. 5S/ZnS multishell nanocrystals. *Journal of the American Chemical Society* **2005**, *127* (20), 7480−7488.

(38) Greytak, A. B.; Allen, P. M.; Liu, W.; Zhao, J.; Young, E. R.; Popović, Z.; Walker, B. J.; Nocera, D. G.; Bawendi, M. G. Alternating layer addition approach to CdSe/CdS core/shell quantum dots with near−unity quantum yield and high on−time fractions. *Chemical science* **2012**, *3* (6), 2028−2034.

(39) García-Santamaría, F.; Chen, Y.; Vela, J.; Schaller, R. D.; Hollingsworth, J. A.; Klimov, V. I. Suppressed auger recombination in "giant" nanocrystals boosts optical gain performance. *Nano Lett.* **2009**, *9* (10), 3482-3488.

(40) Javaux, C.; Mahler, B.; Dubertret, B.; Shabaev, A.; Rodina, A.; Efros, A. L.; Yakovlev, D.; Liu, F.; Bayer, M.; Camps, G. Thermal activation of non-radiative Auger recombination in charged colloidal nanocrystals. *Nature nanotechnology* **2013**, *8* (3), 206-212.

(41) Chen, Y.; Vela, J.; Htoon, H.; Casson, J. L.; Werder, D. J.; Bussian, D. A.; Klimov, V. I.; Hollingsworth, J. A. "Giant" multishell CdSe nanocrystal quantum dots with suppressed blinking. *Journal of the American Chemical Society* **2008**, *130* (15), 5026-5027.

(42) Mahler, B.; Spinicelli, P.; Buil, S.; Quelin, X.; Hermier, J.-P.; Dubertret, B. Towards non-blinking colloidal quantum dots. *Nature materials* **2008**, *7* (8), 659-664.

(43) Cirloganu, C. M.; Padilha, L. A.; Lin, Q.; Makarov, N. S.; Velizhanin, K. A.; Luo, H.; Robel, I.; Pietryga, J. M.; Klimov, V. I. Enhanced Carrier Multiplication in Engineered Quasi-Type-II Quantum Dots. *Nat. Commun.* **2014**, *5* (1), 1-8.

(44) Wu, K.; Liang+, G.; Kong, D.; Chen, J.; Chen, Z.; Shan, X.; McBride, J. R.; Lian, T. Quasi-type II CuInS 2/CdS core/shell quantum dots. *Chemical science* **2016**, *7* (2), 1238-1244.

(45) Wang, C.; Tong, X.; Wang, W.; Xu, J.-Y.; Besteiro, L. V.; Channa, A. I.; Lin, F.; Wu, J.; Wang, Q.; Govorov, A. O. Manipulating the Optoelectronic Properties of Quasi-type II CuInS2/CdS Core/Shell Quantum Dots for Photoelectrochemical Cell Applications. *ACS Applied Materials & Interfaces* **2020**.

(46) Jang, E.-P.; Han, C.-Y.; Lim, S.-W.; Jo, J.-H.; Jo, D.-Y.; Lee, S.-H.; Yoon, S.-Y.; Yang, H. Synthesis of Alloyed ZnSeTe Quantum Dots as Bright, Color-Pure Blue Emitters. *ACS Appl. Mater. Interfaces* **2019**, *11* (49), 46062-46069.

(47) Asano, H.; Tsukuda, S.; Kita, M.; Fujimoto, S.; Omata, T. Colloidal Zn (Te, Se)/ZnS Core/Shell Quantum Dots Exhibiting Narrow-Band and Green Photoluminescence.

ACS omega 2018, *3* (6), 6703−6709.

(48) Lee, S.−H.; Han, C.−Y.; Song, S.−W.; Jo, D.−Y.; Jo, J.−H.; Yoon, S.−Y.; Kim, H.−M.; Hong, S.; Hwang, J. Y.; Yang, H. ZnSeTe Quantum Dots as an Alternative to InP and Their High−Efficiency Electroluminescence. *Chemistry of Materials* 2020.

(49) Hahm, D.; Ko, D.; Jeong, B. G.; Jeong, S.; Lim, J.; Bae, W. K.; Lee, C.; Char, K. Environmentally benign nanocrystals: challenges and future directions. *Journal of Information Display* 2019, *20* (2), 61−72.

(50) Jeong, B. G.; Park, Y.−S.; Chang, J. H.; Cho, I.; Kim, J. K.; Kim, H.; Char, K.; Cho, J.; Klimov, V. I.; Park, P. Colloidal spherical quantum wells with near−unity photoluminescence quantum yield and suppressed blinking. *ACS nano* 2016, *10* (10), 9297−9305.

(51) Nagamine, G.; Jeong, B. G.; Ferreira, T. A.; Chang, J. H.; Park, K.; Lee, D. C.; Bae, W. K.; Padilha, L. A. Efficient Optical Gain in Spherical Quantum Wells Enabled by Engineering Biexciton Interactions. *ACS Photonics* 2020, *7* (8), 2252−2264.

(52) El−Nahass, M.; Khalifa, B.; El−Rahman, A. A.; El−Ariny, R. Structural and optical properties of ZnSe x Te 1−−x solid solutions in thin−film form. *Applied Physics A* 1996, *63* (1), 81−86.

(53) Wei, S. H.; Zunger, A. Band offsets and optical bowings of chalcopyrites and Zn-based II-VI alloys. *Journal of Applied Physics* 1995, *78* (6), 3846−3856.

(54) Hernandez−Calderon, I. Optical properties and electronic structure of wide band gap II−VI semiconductors. *II−VI Semiconductor Materials and Their Applications* 2002, *12*, 113−170.

(55) Padilha, L. A.; Bae, W. K.; Klimov, V. I.; Pietryga, J. M.; Schaller, R. D. Response of semiconductor nanocrystals to extremely energetic excitation. *Nano letters* 2013, *13* (3), 925−932.

(56) Rhee, S.; Chang, J. H.; Hahm, D.; Kim, K.; Jeong, B. G.; Lee, H. J.; Lim, J.; Char, K.; Lee, C.; Bae, W. K. "Positive incentive" approach to enhance the operational stability of quantum dot−based light−emitting diodes. *ACS applied materials & interfaces* 2019, *11* (43), 40252−

40259.

(57) Lim, J.; Park, M.; Bae, W. K.; Lee, D.; Lee, S.; Lee, C.; Char, K. Highly efficient cadmium−free quantum dot light−emitting diodes enabled by the direct formation of excitons within InP@ ZnSeS quantum dots. *ACS nano* **2013**, *7* (10), 9019−9026.

(58) Spindler, J. P.; Hamer, J. W.; Kondakova, M. E. *White OLED Lighting Panel Manufacturing Process*. 2014.

(59) Park, Y. S.; Kang, J. W.; Kang, D. M.; Park, J. W.; Kim, Y. H.; Kwon, S. K.; Kim, J. J. Efficient, Color Stable White Organic Light-Emitting Diode Based on High Energy Level Yellowish-Green Dopants. *Advanced Materials* **2008**, *20* (10), 1957−1961.

(60) Brus, L. E. Electron–electron and electron-hole interactions in small semiconductor crystallites: The size dependence of the lowest excited electronic state. *J. Chem. Phys.* **1984**, *80* (9), 4403−4409.

(61) Klimov, V. I. *Nanocrystal quantum dots;* CRC press, 2017.

(62) Ning, C.−Z.; Dou, L.; Yang, P. Bandgap engineering in semiconductor alloy nanomaterials with widely tunable compositions. *Nature Reviews Materials* **2017**, *2* (12), 1−14.

(63) Protesescu, L.; Yakunin, S.; Bodnarchuk, M. I.; Krieg, F.; Caputo, R.; Hendon, C. H.; Yang, R. X.; Walsh, A.; Kovalenko, M. V. Nanocrystals of cesium lead halide perovskites (CsPbX3, X= Cl, Br, and I): novel optoelectronic materials showing bright emission with wide color gamut. *Nano Lett.* **2015**, *15* (6), 3692−3696.

(64) Lim, J.; Park, Y.−S.; Klimov, V. I. Optical Gain in Colloidal Quantum Dots Achieved with Direct−Current Electrical Pumping. *Nat. Mater.* **2018**, *17* (1), 42−49.

(65) Roh, J.; Park, Y.−S.; Lim, J.; Klimov, V. I. Optically Pumped Colloidal−Quantum−Dot Lasing in LED−like Devices with an Integrated Optical Cavity. *Nat. Commun.* **2020**, *11* (1), 1−10.

(66) Fan, F.; Voznyy, O.; Sabatini, R. P.; Bicanic, K. T.; Adachi, M. M.; McBride, J. R.; Reid, K. R.; Park, Y.−S.; Li, X.; Jain, A. Continuous−wave lasing in colloidal quantum dot solids enabled by facet−selective epitaxy. *Nature* **2017**, *544* (7648), 75−79.

(67) Wu, K.; Li, H.; Klimov, V. I. Tandem Luminescent Solar Concentrators Based on Engineered Quantum Dots. *Nat. Photon.* **2018**, *12* (2), 105−110.

(68) Chang, J. H.; Lee, H. J.; Rhee, S.; Hahm, D.; Jeong, B. G.; Nagamine, G.; Padilha, L. A.; Char, K.; Hwang, E.; Bae, W. K. Pushing the Band Gap Envelope of Quasi−Type II Heterostructured Nanocrystals to Blue: ZnSe/ZnSe1−XTeX/ZnSe Spherical Quantum Wells. *Energy mater. adv.* **2021**, *2021*.

(69) Kim, T.; Kim, K.−H.; Kim, S.; Choi, S.−M.; Jang, H.; Seo, H.−K.; Lee, H.; Chung, D.−Y.; Jang, E. Efficient and stable blue quantum dot light−emitting diode. *Nature* **2020**, *586* (7829), 385−389.

(70) Bao, Z.; Jiang, Z.−F.; Su, Q.; Chiu, H.−D.; Yang, H.; Chen, S.; Chung, R.−J.; Liu, R.−S. ZnSe: Te/ZnSeS/ZnS Nanocrystals: An Access to Cadmium−Free Pure−Blue Quantum−Dot Light−Emitting Diodes. *Nanoscale* **2020**, *12* (21), 11556−11561.

(71) Han, C.−Y.; Lee, S.−H.; Song, S.−W.; Yoon, S.−Y.; Jo, J.−H.; Jo, D.−Y.; Kim, H.−M.; Lee, B.−J.; Kim, H.−S.; Yang, H. More than 9% Efficient ZnSeTe Quantum Dot−based Blue Electroluminescent Devices. *ACS Energy Lett.* **2020**, *5* (5), 1568−1576.

(72) Lee, S.−H.; Song, S.−W.; Yoon, S.−Y.; Jo, D.−Y.; Kim, S.−K.; Kim, H.−M.; Kim, Y.; Park, S. M.; Yang, H. Heterostructural Tailoring of Blue ZnSeTe Quantum Dots Toward High−Color Purity and High−Efficiency Electroluminescence. *Chem. Eng. J.* **2022**, *429*, 132464.

(73) Tosini, G.; Ferguson, I.; Tsubota, K. Effects of blue light on the circadian system and eye physiology. *Mol. Vis.* **2016**, *22*, 61.

(74) Sugawara, M.; Choi, S.−Y.; Wood, D. Ultra−high−definition television (Rec. ITU−R BT. 2020): A generational leap in the evolution of television [standards in a nutshell]. *IEEE Signal Process. Mag.* **2014**, *31* (3), 170−174.

(75) Series, B. Parameter values for ultra−high definition television systems for production and international programme exchange. **2012**.

(76) Hahm, D.; Chang, J. H.; Jeong, B. G.; Park, P.; Kim, J.;

Lee, S.; Choi, J.; Kim, W. D.; Rhee, S.; Lim, J. Design Principle for Bright, Robust, and Color−Pure InP/ZnSe x S1-x/ZnS Heterostructures. *Chem. Mater.* **2019**, *31* (9), 3476−3484.

(77) Jeong, B. G.; Chang, J. H.; Hahm, D.; Rhee, S.; Park, M.; Lee, S.; Kim, Y.; Shin, D.; Park, J. W.; Lee, C. Interface polarization in heterovalent core-shell nanocrystals. *Nat. Mater.* **2021**, 1−7.

(78) Bae, W. K.; Padilha, L. A.; Park, Y.−S.; McDaniel, H.; Robel, I.; Pietryga, J. M.; Klimov, V. I. Controlled Alloying of the Core-Shell Interface in CdSe/CdS Quantum Dots for Suppression of Auger Recombination. *ACS Nano* **2013**, *7* (4), 3411−3419.

(79) Park, Y.−S.; Bae, W. K.; Baker, T.; Lim, J.; Klimov, V. I. Effect of Auger Recombination on Lasing in Heterostructured Quantum Dots with Engineered Core/Shell Interfaces. *Nano Lett.* **2015**, *15* (11), 7319−7328.

(80) Kim, S.; Fisher, B.; Eisler, H.−J.; Bawendi, M. Type−II Quantum Dots: CdTe/CdSe (Core/Shell) and CdSe/ZnTe (Core/Shell) Heterostructures. *J. Am. Chem. Soc.* **2003**, *125* (38), 11466−11467.

(81) Piryatinski, A.; Ivanov, S. A.; Tretiak, S.; Klimov, V. I. Effect of Quantum and Dielectric Confinement on The Exciton− Exciton Interaction Energy in Type II Core/Shell Semiconductor Nanocrystals. *Nano Lett.* **2007**, *7* (1), 108−115.

(82) Ivanov, S. A.; Piryatinski, A.; Nanda, J.; Tretiak, S.; Zavadil, K. R.; Wallace, W. O.; Werder, D.; Klimov, V. I. Type−II Core/Shell CdS/ZnSe Nanocrystals: Synthesis, Electronic Structures, and Spectroscopic Properties. *J. Am. Chem. Soc.* **2007**, *129* (38), 11708−11719.

(83) Knowles, K. E.; Nelson, H. D.; Kilburn, T. B.; Gamelin, D. R. Singlet-Triplet Splittings in the Luminescent Excited States of Colloidal Cu+: CdSe, Cu+: InP, and CuInS2 Nanocrystals: Charge−Transfer Configurations and Self−Trapped Excitons. *J. Am. Chem. Soc.* **2015**, *137* (40), 13138−13147.

(84) Pradhan, N.; Peng, X. Efficient and Color−Tunable Mn−doped ZnSe Nanocrystal Emitters: Control of Optical

Performance via Greener Synthetic Chemistry. *J. Am. Chem. Soc.* **2007**, *129* (11), 3339−3347.

(85) Zang, H.; Li, H.; Makarov, N. S.; Velizhanin, K. A.; Wu, K.; Park, Y.−S.; Klimov, V. I. Thick−shell CuInS2/ZnS quantum dots with suppressed "blinking" and narrow single−particle emission line widths. *Nano Lett.* **2017**, *17* (3), 1787−1795.

(86) Avidan, A.; Oron, D. Large Blue Shift of The Biexciton State in Tellurium Doped CdSe Colloidal Quantum Dots. *Nano Lett.* **2008**, *8* (8), 2384−2387.

(87) Avidan, A.; Pinkas, I.; Oron, D. How Quickly Does a Hole Relax into an Engineered Defect State in CdSe Quantum Dots. *ACS Nano* **2012**, *6* (4), 3063−3069.

(88) Tenne, R.; Pedetti, S.; Kazes, M.; Ithurria, S.; Houben, L.; Nadal, B.; Oron, D.; Dubertret, B. From Dilute Isovalent Substitution to Alloying in CdSeTe Nanoplatelets. *Phys. Chem. Chem. Phys.* **2016**, *18* (22), 15295−15303.

(89) Franzl, T.; Müller, J.; Klar, T. A.; Rogach, A. L.; Feldmann, J.; Talapin, D. V.; Weller, H. CdSe: Te nanocrystals: Band−edge versus Te−related emission. *J. Phys. Chem. C* **2007**, *111* (7), 2974−2979.

(90) Wu, J.; Walukiewicz, W.; Yu, K.; Ager III, J. W.; Haller, E. E.; Miotkowski, I.; Ramdas, A. K.; Su, C.−H.; Sou, I.; Perera, R. C. Origin of The Large Band−Gap Bowing in Highly Mismatched Semiconductor Alloys. *Phys. Rev. B.* **2003**, *67* (3), 035207.

(91) Gu, Y.; Kuskovsky, I. L.; Van der Voort, M.; Neumark, G.; Zhou, X.; Tamargo, M. Zn− Se− Te Multilayers with Submonolayer Quantities of Te: Type−II Quantum Structures and Isoelectronic Centers. *Phys. Rev. B.* **2005**, *71* (4), 045340.

(92) Muller, A.; Bianucci, P.; Piermarocchi, C.; Fornari, M.; Robin, I.; André, R.; Shih, C. Time−Resolved Photoluminescence Spectroscopy of Individual Te Impurity Centers in ZnSe. *Phys. Rev. B.* **2006**, *73* (8), 081306.

(93) Kuskovsky, I. L.; Tian, C.; Neumark, G.; Spanier, J.; Herman, I. P.; Lin, W.−C.; Guo, S.; Tamargo, M. Optical Properties of δ−doped ZnSe: Te Grown by Molecular Beam Epitaxy: The Role of Tellurium. *Phys. Rev. B.* **2001**,

63 (15), 155205.

(94) Perdew, J. P.; Burke, K.; Ernzerhof, M. Generalized Gradient Approximation Made Simple. *Phys. Rev. Lett.* **1996**, *77* (18), 3865.

(95) Giannozzi, P.; Baroni, S.; Bonini, N.; Calandra, M.; Car, R.; Cavazzoni, C.; Ceresoli, D.; Chiarotti, G. L.; Cococcioni, M.; Dabo, I. QUANTUM ESPRESSO: A Modular and Open-Source Software Project for Quantum Simulations of Materials. *J. Phys.: Condens. Matter* **2009**, *21* (39), 395502.

(96) Whitham, P. J.; Marchioro, A.; Knowles, K. E.; Kilburn, T. B.; Reid, P. J.; Gamelin, D. R. Single-particle photoluminescence spectra, blinking, and delayed luminescence of colloidal CuInS2 nanocrystals. *J. Phys. Chem. C.* **2016**, *120* (30), 17136-17142.

(97) Cui, J.; Beyler, A. P.; Coropceanu, I.; Cleary, L.; Avila, T. R.; Chen, Y.; Cordero, J. M.; Heathcote, S. L.; Harris, D. K.; Chen, O. Evolution of the single-nanocrystal photoluminescence linewidth with size and shell: implications for exciton-phonon coupling and the optimization of spectral linewidths. *Nano Lett.* **2016**, *16* (1), 289-296.

(98) Groeneveld, E.; de Mello Doneg□, C. Enhanced Exciton-Phonon Coupling in Colloidal Type-II CdTe-CdSe Heteronanocrystals. *J. Phys. Chem. C* **2012**, *116* (30), 16240-16250.

(99) Micic, O. I.; Sprague, J. R.; Curtis, C. J.; Jones, K. M.; Machol, J. L.; Nozik, A. J.; Giessen, H.; Fluegel, B.; Mohs, G.; Peyghambarian, N. Synthesis and Characterization of Inp, Gap, and Gainp2 Quantum Dots. *J. Phys. Chem.* **1995**, *99* (19), 7754-7759.

(100) Yu, W. W.; Peng, X. Formation of high-quality CdS and other II-VI semiconductor nanocrystals in noncoordinating solvents: tunable reactivity of monomers. *Angew. Chem., Int. Ed.* **2002**, *41* (13), 2368-71.

(101) Hines, M. A.; Guyot-Sionnest, P. Synthesis and characterization of strongly luminescing ZnS-Capped CdSe nanocrystals. *J. Phys. Chem.* **1996**, *100* (2), 468-471.

(102) Lim, J.; Jeong, B. G.; Park, M.; Kim, J. K.; Pietryga, J. M.;

Park, Y.-S.; Klimov, V. I.; Lee, C.; Lee, D. C.; Bae, W. K. Influence of Shell Thickness on the Performance of Light-Emitting Devices Based on CdSe/Zn1-XCdXS Core/Shell Heterostructured Quantum Dots. *Adv. Mater.* **2014**, *26* (47), 8034-8040.

(103) Park, Y. S.; Lim, J.; Klimov, V. I. Asymmetrically strained quantum dots with non-fluctuating single-dot emission spectra and subthermal room-temperature linewidths. *Nat. Mater.* **2019**, *18* (3), 249-255.

(104) Jeong, B. G.; Chang, J. H.; Hahm, D.; Rhee, S.; Park, M.; Lee, S.; Kim, Y.; Shin, D.; Park, J. W.; Lee, C.; Lee, D. C.; Park, K.; Hwang, E.; Bae, W. K. Interface polarization in heterovalent core-shell nanocrystals. *Nat. Mater.* **2022**, *21* (2), 246-252.

(105) Cho, K.-S.; Lee, E. K.; Joo, W.-J.; Jang, E.; Kim, T.-H.; Lee, S. J.; Kwon, S.-J.; Han, J. Y.; Kim, B.-K.; Choi, B. L.; Kim, J. M. High-performance crosslinked colloidal quantum-dot light-emitting diodes. *Nat. Photonics* **2009**, *3* (6), 341-345.

(106) Jang, E.; Jun, S.; Jang, H.; Lim, J.; Kim, B.; Kim, Y. White-light-emitting diodes with quantum dot color converters for display backlights. *Adv. Mater.* **2010**, *22* (28), 3076-80.

(107) Hahm, D.; Lim, J.; Kim, H.; Shin, J. W.; Hwang, S.; Rhee, S.; Chang, J. H.; Yang, J.; Lim, C. H.; Jo, H.; Choi, B.; Cho, N. S.; Park, Y. S.; Lee, D. C.; Hwang, E.; Chung, S.; Kang, C. M.; Kang, M. S.; Bae, W. K. Direct patterning of colloidal quantum dots with adaptable dual-ligand surface. *Nat. Nanotechnol.* **2022**, *17* (9), 952-958.

(108) Eisler, H. J.; Sundar, V. C.; Bawendi, M. G.; Walsh, M.; Smith, H. I.; Klimov, V. Color-selective semiconductor nanocrystal laser. *Appl. Phys. Lett.* **2002**, *80* (24), 4614-4616.

(109) Choi, H. S.; Liu, W.; Misra, P.; Tanaka, E.; Zimmer, J. P.; Itty Ipe, B.; Bawendi, M. G.; Frangioni, J. V. Renal clearance of quantum dots. *Nat. Biotechnol.* **2007**, *25* (10), 1165-70.

(110) Li, H. B.; Wu, K. F.; Lim, J.; Song, H. J.; Klimov, V. I. Doctor-blade deposition of quantum dots onto standard window glass for low-loss large-area luminescent solar

concentrators. *Nat. Energy* **2016**, *1* (12), 16157.

(111) Jeong, B. G.; Hahm, D.; Park, J. W.; Kim, J. Y.; Song, H. E.; Kang, M. G.; Jeong, S.; Kang, G.; Bae, W. K.; Song, H. J. Colorful opaque photovoltaic modules with down-converting InP/ZnSexS1-x quantum dot layers. *Nano Energy* **2020**, *77*, 105169.

(112) Kruszynska, M.; Borchert, H.; Parisi, J.; Kolny-Olesiak, J. Synthesis and shape control of CuInS(2) nanoparticles. *J. Am. Chem. Soc.* **2010**, *132* (45), 15976-86.

(113) Uematsu, T.; Wajima, K.; Sharma, D. K.; Hirata, S.; Yamamoto, T.; Kameyama, T.; Vacha, M.; Torimoto, T.; Kuwabata, S. Narrow band-edge photoluminescence from AgInS2 semiconductor nanoparticles by the formation of amorphous III–VI semiconductor shells. *NPG Asia Mater.* **2018**, *10* (8), 713-726.

(114) Kim, Y.; Ham, S.; Jang, H.; Min, J. H.; Chung, H.; Lee, J.; Kim, D.; Jang, E. Bright and Uniform Green Light Emitting InP/ZnSe/ZnS Quantum Dots for Wide Color Gamut Displays. *ACS Appl. Nano Mater* **2019**, *2* (3), 1496-1504.

(115) Hahm, D.; Chang, J. H.; Jeong, B. G.; Park, P.; Kim, J.; Lee, S.; Choi, J.; Kim, W. D.; Rhee, S.; Lim, J.; Lee, D. C.; Lee, C.; Char, K.; Bae, W. K. Design Principle for Bright, Robust, and Color-Pure InP/ZnSexS1–x/ZnS Heterostructures. *Chem. Mater.* **2019**, *31* (9), 3476-3484.

(116) Altıntas, Y.; Talpur, M. Y.; Ünlü, M.; Mutlugün, E. Highly Efficient Cd-Free Alloyed Core/Shell Quantum Dots with Optimized Precursor Concentrations. *J. Phys. Chem. C.* **2016**, *120* (14), 7885-7892.

(117) Yu, P.; Cao, S.; Shan, Y.; Bi, Y.; Hu, Y.; Zeng, R.; Zou, B.; Wang, Y.; Zhao, J. Highly efficient green InP-based quantum dot light-emitting diodes regulated by inner alloyed shell component. *Light: Sci. Appl.* **2022**, *11* (1), 162.

(118) Chang, J. H.; Lee, H. J.; Rhee, S.; Hahm, D.; Jeong, B. G.; Nagamine, G.; Padilha, L. A.; Char, K.; Hwang, E.; Bae, W. K. Pushing the Band Gap Envelope of Quasi-Type II Heterostructured Nanocrystals to Blue: ZnSe/ZnSe1-XTeX/ZnSe Spherical Quantum Wells. *Energy Mater. Adv.* **2021**, *2021*, 3245731.

(119) Lee, S. H.; Han, C. Y.; Song, S. W.; Jo, D. Y.; Jo, J. H.; Yoon, S. Y.; Kim, H. M.; Hong, S.; Hwang, J. Y.; Yang, H. ZnSeTe Quantum Dots as an Alternative to InP and Their High−Efficiency Electroluminescence. *Chem. Mater.* **2020**, *32* (13), 5768−5775.

(120) Huang, Z.; Sun, Q.; Zhao, S.; Wu, B.; Zhang, M.; Zang, Z.; Wang, Y. Deciphering Ultrafast Carrier Dynamics of Eco−Friendly ZnSeTe−Based Quantum Dots: Toward High−Quality Blue-Green Emitters. *J. Phys. Chem. Lett.* **2021**, *12* (49), 11931−11938.

(121) Uematsu, T.; Doi, T.; Torimoto, T.; Kuwabata, S. Preparation of luminescent AgInS2− AgGaS2 solid solution nanoparticles and their optical properties. *J. Phys. Chem. Lett.* **2010**, *1* (22), 3283−3287.

(122) Kameyama, T.; Kishi, M.; Miyamae, C.; Sharma, D. K.; Hirata, S.; Yamamoto, T.; Uematsu, T.; Vacha, M.; Kuwabata, S.; Torimoto, T. Wavelength−tunable band−edge photoluminescence of nonstoichiometric Ag-In-S nanoparticles via Ga3+ doping. *ACS Appl. Mater. Interfaces* **2018**, *10* (49), 42844−42855.

(123) Kim, J.−H.; Kim, B.−Y.; Jang, E.−P.; Yoon, S.−Y.; Kim, K.−H.; Do, Y. R.; Yang, H. Synthesis of widely emission−tunable Ag-Ga-S and its quaternary derivative quantum dots. *Chem. Eng. J.* **2018**, *347*, 791−797.

(124) Hu, Z.; Lu, H.; Zhou, W.; Wei, J.; Dai, H.; Liu, H.; Xiong, Z.; Xie, F.; Zhang, W.; Guo, R. Aqueous synthesis of 79% efficient AgInGaS/ZnS quantum dots for extremely high color rendering white light−emitting diodes. *J. Mater. Sci. Technol.* **2023**, *134*, 189−196.

(125) Hoisang, W.; Uematsu, T.; Torimoto, T.; Kuwabata, S. Luminescent Quaternary Ag (In x Ga1-x) S2/GaS y Core/Shell Quantum Dots Prepared Using Dithiocarbamate Compounds and Photoluminescence Recovery via Post Treatment. *Inorgan. Chem.* **2021**, *60* (17), 13101−13109.

(126) Hoisang, W.; Uematsu, T.; Torimoto, T.; Kuwabata, S. Photoluminescence Stability Enhancement of Ag-In-Ga-S/GaSx Core/Shell Quantum Dots with Thicker Shells by the Addition of Gallium Diethyldithiocarbamate. *Chem. Lett.* **2021**, *50* (11), 1863−1866.

(127) Hoisang, W.; Uematsu, T.; Torimoto, T.; Kuwabata, S. Surface ligand chemistry on quaternary Ag (In x Ga 1−x) S 2 semiconductor quantum dots for improving photoluminescence properties. *Nanoscale Adv.* **2022**, *4* (3), 849−857.

(128) Gungor, K.; Du, J.; Klimov, V. I. General Trends in the Performance of Quantum Dot Luminescent Solar Concentrators (LSCs) Revealed Using the "Effective LSC Quality Factor". *ACS Energy Lett.* **2022**, *7* (5), 1741−1749.

(129) Klimov, V. I.; Baker, T. A.; Lim, J.; Velizhanin, K. A.; McDaniel, H. Quality Factor of Luminescent Solar Concentrators and Practical Concentration Limits Attainable with Semiconductor Quantum Dots. *ACS Photonics* **2016**, *3* (6), 1138−1148.

(130) Song, H. J.; Jeong, B. G.; Lim, J.; Lee, D. C.; Bae, W. K.; Klimov, V. I. Performance Limits of Luminescent Solar Concentrators Tested with Seed/Quantum−Well Quantum Dots in a Selective−Reflector−Based Optical Cavity. *Nano Lett.* **2018**, *18* (1), 395−404.

(131) Lee, G.; Kim, M. C.; Choi, Y. W.; Ahn, N.; Jang, J.; Yoon, J.; Kim, S. M.; Lee, J. G.; Kang, D.; Jung, H. S.; Choi, M. Ultra−flexible perovskite solar cells with crumpling durability: toward a wearable power source. *Energy Environ. Sci.* **2019**, *12* (10), 3182−3191.

국문초록

콜로이드 양자점은 좁은 발광선폭, 높은 발광효율, 크기에 따라 조절되는 밴드갭과 같은 독특하고 우수한 광특성으로 광변환층, 전계발광소자, 레이저 등의 다양한 응용분야에서 각광받고 있다. 하지만 이러한 우수한 성과들은 대부분 CdSe 기반 양자점 기반 소재로 달성되었는데, 카드뮴계 양자점의 독성으로 인하여 산업계에 적용되기 불가능하다.

이에 대한 해답으로 InP 기반 양자점 소재가 개발되었지만 청색영역에서의 낮은 흡광특성, 넓은 발광반치폭, 청색 영역 발광 양자점의 합성 불가능 등의 이유로 새로운 친환경 양자점 소재의 필요성이 대두되었다.

본 학위논문에서는 전체 가시광 영역에서 높은 양자 발광효율을 보이는 양자우물구조 ZnSe/ZnSe$_{1-X}$Te$_X$/ZnSe 양자점과 코어쉘 AgIn$_X$Ga$_{1-X}$S$_2$/AgGaS$_2$ 양자점의 합성법과 특성분석에 대해 논의한다. 심층적인 구조, 광, 광물리적 특성의 분석과 양자계산을 통해 합성메커니즘과 발광 특성을 밝혀내었고 이의 다양한 응용을 소개한다.

제1 장에서는 기본적인 양자점의 특성과 친환경 양자점의 역사에 대해 간략히 소개하였다. 기존 양자점의 이종접합구조와 밴드갭 조절을 위한 합금 코어, 오제 재결합 특성을 요약하고 친환경 양자점을 소개하며 현 시점에서 친환경 양자점의 단점에 대해 논의하였다.

제2 장에서는 양자우물구조로 인한 격자비일치 차이를 완화하여 100 %의 발광효율을 가지는 ZnSe/ZnSe$_{1-X}$Te$_X$/ZnSe 양자점을 합성하는 방법을 소개한다. 뿐만 아니라 *quasi*-type Ⅱ의 밴드구조를 가지는 ZnSe/ZnSe$_{1-X}$Te$_X$/ZnSe 양자점은 쉘 두께 조절을 통하여서도 밴드갭을 조절할 수 있어 더욱 섬세한 조절이 가능하다. 이러한 특성으로 인해 청색부터 적색까지 넓은 발광파장대에서 높은 ㅂ라광효

율을 구현할 수 있는 양자우물구조 양자점의 특성을 이용하여 2색성(청색+주황색)의 백색 발광 전계발광 소자를 제작하여 해당 소재의 우수성을 증명하였다.

제3, 4 장에서는 2 장에서 제시한 $ZnSe/ZnSe_{1-x}Te_x/ZnSe$ 청색 양자점에서 관측되는 비대칭적인 양자점의 발광스펙트럼과 녹색 양자점의 다중전하엑시톤(multicarrier)의 발광특성에 대해 분석하였다. 군집, 개별 양자점의 광 및 광물리학적 특성분석과 양자계산을 통하여 청색 발광 $ZnSe/ZnSe_{1-x}Te_x/ZnSe$ 양자점의 비대칭 발광 스펙트럼이 양자점 발광층 내 개별 Te과 Te_2 간의 에너지 준위 차이로 인해 발생하는 것을 밝혀내었다. 또한 새로운 광-전계측정법을 개발하여 기존 방법으로는 확인할 수 없었던 녹색 발광 $ZnSe/ZnSe_{1-x}Te_x/ZnSe$ 양자점의 포지티브, 네거티브 트라이온 발광 거동을 측정하였다.

제5 장에서는 신규 친환경 양자점 조성으로 $\mathrm{I-III-VI_2/I-III-VI_2}$ 코어/쉘 양자점인 $AgIn_xGa_{1-x}S_2/AgGaS_2$을 최초로 합성하였다. 본 연구진은 $Ag-S-Ga(OA)_2$ 중간체의 도입을 통하여 Ag와 Ga간 반응성 차이를 완화하여 균일한 AIGS 코어와 AGS 쉘 성장을 달성하였다. 이렇게 합성된 AIGS/AGS 양자점은 가시광 영역에서 높은 흡광계수, 발광효율, 좁은 발광선폭을 가져 InP 기반 양자점을 대체할 수 있을 것으로 기대된다. 실제 태양전지 광변환층으로 이용하였을 때 InP/ZnSeS 양자점에 비해 절반의 농도로 더 높은 광변환효율을 달성하였다.

본 학위논문으로 개발된 신규 친환경 양자점은 우수한 발광특성을 지녀 디스플레이용 양자점 소재로 적합하다. 추후 이러한 소재는 광변환층, 전계발광소자, 레이저 등 다양한 분야로 적용되어 양자점 산업 및 연구에 크게 기여할 것으로 예상된다.

주요어 : 콜로이드 양자점 · 친환경 양자점 · 양자우물구조 · 오제 재결합 · 합성 메커니즘

학번 : 2018-22155